

**MICROBIALY MEDIATED SEDIMENTARY STRUCTURES AND STROMATOLITES IN
THE MISSISSIPPIAN STRATA OF THE HORTON BLUFF FORMATION, NOVA SCOTIA**

Alison Fiona Gallacher

**Submitted in Partial Fulfilment of the Requirements
for the Degree of Bachelor of Science, Honours
Department of Earth Sciences
Dalhousie University Halifax, Nova Scotia
March 2010**

ABSTRACT

Over the past decade, microbial mats have been identified as major players in sedimentology. The mats are thin crusts, largely of bacterial origin and form rubbery mats on sediment surfaces, which they protect from erosion. Domal stromatolites are also microbial in origin. Microbial mats and stromatolites have been recognized as far back as 3.5 billion years but until recently, mats on flat-lying surfaces have been difficult to identify and have been overlooked.

Stromatolites and remnants of microbial mats have been discovered at Blue Beach in the Mississippian Horton Bluff Formation of Nova Scotia. The domes range in height from 13 to 30 cm and have horizontal bases ranging in width from 15 to 60 cm. The domes are spaced individually and in clusters along a gently dipping bedding surface on the tidal platform. The stromatolite bed can be correlated with strata in the adjacent cliff approximately 47 m distant, and the spacing of each group on the bedding surface ranged from 3.4 m to 10.6 m. The domes have oversteepened laminae at the margins of approximately 35°, steeper than the angle of repose for any wet sediment, suggesting sediment fixation with possible microbial origin.

The remnants of microbial mats have been found on an equivalent bedding surface of very fine-grained sandstone in the cliff face. The mats, which are also termed wrinkle structures, have no distinct orientation and do not cover the entire surface, forming patches with an average diameter of 8-10 cm. The largest wrinkles are up to 4 mm in relief. Domal stromatolites are also seen in the cliff face, and in one instance a dome surrounds remnants of a tree stump with wrinkle structures on the bedding surface around the feature.

Petrological analysis identified four micofacies (A to D) with a similar upward succession within several stromatolite domes. The domes grew from a greenish layer with discontinuous dolosiltite laminae (A), overlain in turn by finely laminated quartz- and dolomite-rich silt (B), massive dololutite (C) and banded dolosiltite and dololutite with quartz grains (D). The domes are penetrated by roots. XRD results show that dolomite is the most abundant mineral, along with quartz and muscovite in the finely laminated layers. Based on a sedimentological analysis of the associated strata, the microbial structures grew in shallow water and on periodically exposed flats, probably in bays that experienced fluctuating salinities and probably hypersaline conditions.

Key Words: Microbial mats, stromatolites, dololutite, dolosiltite, siliciclastic



**DALHOUSIE
UNIVERSITY**

Inspiring Minds

Department of Earth Sciences

Halifax, Nova Scotia

Canada B3H 4J1

(902) 494-2358

FAX (902) 494-6889

DATE: April 28th, 2010

AUTHOR: Alison Fiona Gallacher

TITLE: Microbially mediated sedimentary structures
and stromatolites in the Mississippian
strata of the Horton Bluff Formation, Nova
Scotia

Degree: Earth Science Convocation: May 2010 Year: 2010

Permission is herewith granted to Dalhousie University to circulate and to have copied for non-commercial purposes, at its discretion, the above title upon the request of individuals or institutions.

Signature of Author

THE AUTHOR RESERVES OTHER PUBLICATION RIGHTS, AND NEITHER THE THESIS NOR EXTENSIVE EXTRACTS FROM IT MAY BE PRINTED OR OTHERWISE REPRODUCED WITHOUT THE AUTHOR'S WRITTEN PERMISSION.

THE AUTHOR ATTESTS THAT PERMISSION HAS BEEN OBTAINED FOR THE USE OF ANY COPYRIGHTED MATERIAL APPEARING IN THIS THESIS (OTHER THAN BRIEF EXCERPTS REQUIRING ONLY PROPER ACKNOWLEDGEMENT IN SCHOLARLY WRITING) AND THAT ALL SUCH USE IS CLEARLY ACKNOWLEDGED.

Table of Contents

Abstract	i
Table of Contents	ii
List of Figures	v
List of Tables	viii
Acknowledgements	ix
Chapter 1.0- Introduction	1
1.1.0 Introduction	1
1.2.0 Geological Setting	1
1.3.0 Previous Work	5
1.3.1 Blue Beach Member- Stratigraphic Background	5
1.3.2 Blue Beach Member- Depositional Environment	5
1.3.3 Blue Beach Member- Microbial Mats and Stromatolites	6
1.4.0 Objectives	7
Chapter 2.0- Microbial Mat and Stromatolite Background	8
2.1.0 Introduction- Microbes	8
2.2.0 Geological Evolution	11
2.3.0 Modern vs. Ancient	12
2.4.0 Stromatolites and Thrombolites- Microbial Structures	13
2.5.0 Diagnostic Criteria	15
2.5.1 Field Criteria	15
2.5.2 Petrology Criteria	18

Chapter 3.0- Methodology	21
3.1.0 Introduction- Research Methods	21
3.2.0 Field Data Collection	21
3.3.0 Facies Observations	22
3.3.1 Megascopic Observations	22
3.3.2 Microscopic Observations	22
3.4.0 X-Ray Diffraction	23
Chapter 4.0- Field Work and Observations	27
4.1.0 Introduction- Study Area	27
4.2.0 Stratigraphy	27
4.2.1 Stratigraphic Descriptions	27
4.2.2 Stratigraphic Interpretations	34
4.3.0 Paleontology	36
4.4.0 Cliff Section Observations	38
4.5.0 Rock Platform Observations	44
4.6.0 Megascopic Interpretations	48
Chapter 5.0- Petrology	51
5.1.0 Introduction- Microscope	51
5.2.0 Slab Observations	52
5.3.0 Facies descriptions	57
5.4.0 Mineralogy Results	68
5.5.0 Microfacies Interpretations	72

Chapter 6.0- Discussion	76
6.1.0 Paleoenvironment of microbial features and modern analogue	76
6.2.0 Siliciclastic stromatolites in the Blue Beach Member	81
6.3.0 Carbonate Diagenesis	83
6.4.0 Microbial influences in the Blue Beach strata	85
Chapter 7.0- Conclusions	86
7.1.0 Results	86
7.1.1 Sedimentology	86
7.1.2 Microbial Mats and Stromatolites	87
7.1.3 Microscopic conclusions	88
7.2.0 Recommendations for Further Analysis	89
Chapter 8.0- References	91
Appendix A- Field data	
Appendix B- Slab Photos	
Appendix C- XRD Data	

LIST OF FIGURES

Figure 1.1	Horton Group within the Windsor Sub-basin	2
Figure 1.2	Regional Geology	3
Figure 1.3	Stratigraphy of Windsor Sub-basin	4
Figure 2.1	Filamentous and coccoid cyanobacteria	8
Figure 2.2	Epibenthic cyanobacteria	9
Figure 2.3	Envisioned formation of domal stromatolites	10
Figure 2.4	Schematic diagram of thrombolites and stromatolites	15
Figure 2.5	Wrinkled bed surface	16
Figure 2.6	Cohesive behaviour	16
Figure 2.7	Small domes with over-steepened laminae	18
Figure 2.8	Dolomitic and clay/silt laminae	19
Figure 4.1	Study area	27
Figure 4.2	Stratigraphic column	31
Figure 4.3	Stratigraphic column with descriptions	32
Figure 4.4	Stratigraphic column with descriptions	33
Figure 4.5	Blue Beach Member	38
Figure 4.6	Exposed bedding surface of study area	39
Figure 4.7	Wrinkled structures	40
Figure 4.8	Gully structures	40
Figure 4.9	Domal structures	41
Figure 4.10	Load structures and Rooted mudstone	42
Figure 4.11	Tree stump fossil	43

Figure 4.12	Desiccated horizon	43
Figure 4.13	GPS map	44
Figure 4.14	Stromatolite mounds on bedding platform	45
Figure 4.15	Domal structures	46
Figure 4.16	Stromatolite mound	47
Figure 4.17	Location of stromatolite mounds	50
Figure 5.1	Schematic diagram of microfacies	53
Figure 5.2	Stromatolite sample FG-4	53
Figure 5.3	Stromatolite sample FG-1	54
Figure 5.4	Graded Beds- thin section	58
Figure 5.5	Cross-laminated and crinkled dark laminae- thin section	59
Figure 5.6	Graded Beds- thin section	60
Figure 5.7	Microfaults- thin section	61
Figure 5.8	Cohesive textures- thin section	61
Figure 5.9	Massive dololomite- thin section	62
Figure 5.10	Wispy mesh-like laminae- thin section	64
Figure 5.11	Clay material- thin section	64
Figure 5.12	Iron rich material penetrated into root system- thin section	65
Figure 5.13	Microfaulting- thin section	66
Figure 5.14	Sample FG-10	67
Figure 5.15	Histogram- Microfacies B	69
Figure 5.16	Histogram- Microfacies C	70
Figure 5.17	Histogram- Vein	71

Figure 5.18	Microfacies- Platform compared to Cliff	73
Figure 6.1	Three phases of deposition	78
Figure 6.2	Variant to Tibert's Model	80
Figure 6.3	The optimal depositional facies	82

LIST OF TABLES

Table 2.1	Comparison of ancient and modern microbial mats	13
Table 2.2	Diagnostic Criteria	17
Table 2.3	Textures of microbial structures	20
Table 4.1	Blue Beach lithofacies and depositional interpretations	30
Table 4.2	Cycles observed in the field	48
Table 5.1	Microfacies Chart	55,56

ACKNOWLEDGMENTS

This thesis would not have been completed without the guidance and endless enthusiasm from Dr. Martin Gibling. If he had not walked along Blue Beach and came across these domal mounds, the project would not have been started. I now have a deep love for stromatolites after long days looking at the specimens in hand sample and thin section. Many thanks go to Gordon Brown, who tirelessly worked on cutting my samples and making the many thin sections. A huge thanks goes to Tom Duffett, who provided me with endless support in the rock crushing room and all the odds and ends of this project. XRD analysis was made easy with Keith Taylor's expertise and energy into the thesis. Finally, I would like to thank my family and friends who have heard me on countless days talking about rocks that they only pretend to understand.

Chapter 1.0- Introduction

1.1.0 Introduction-

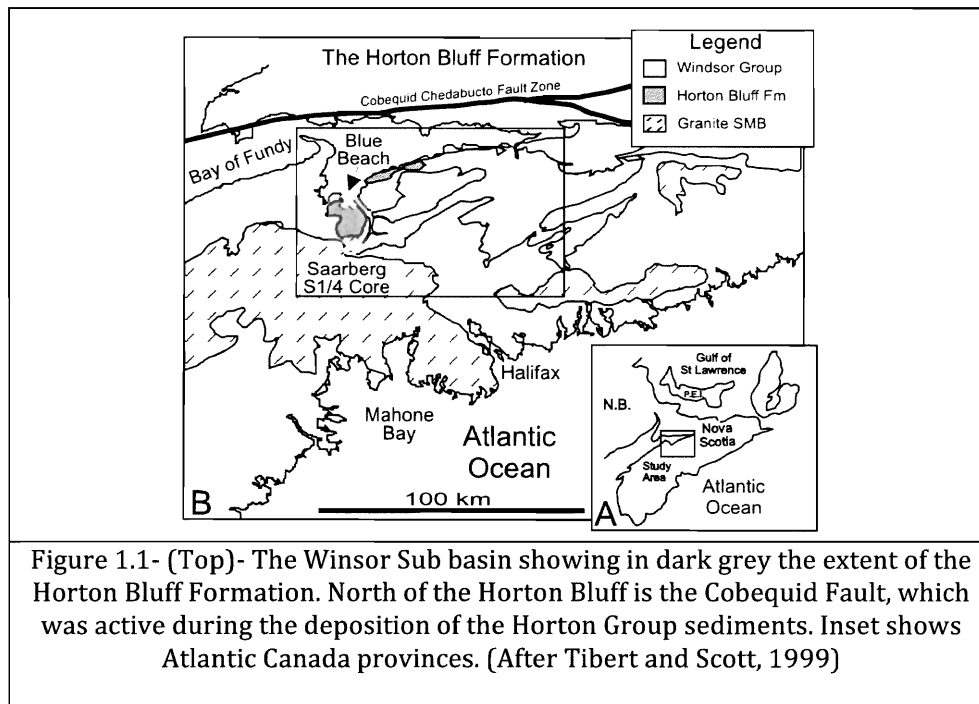
Over the past decade, microbial mats have been identified as major players in sedimentology. The mats are thin crusts, largely generated by cyanobacteria. They form rubbery mats on sediment surfaces by baffling, binding and gluing, which ultimately provide a protective film across the surface and prevents extensive weathering (Pflugger, 1999). Microbes grow in extreme environments and can form domal structures, which include thrombolite and stromatolite fabrics that are distinguished by their internal geometries (Kennard & James, 1986). Domal stromatolites have been identified on the modern rock platform at Blue Beach, Nova Scotia and microbial mats, unique with their wrinkle structures, have been identified on the same bedding surface within the main cliff face. The focus of this research is to determine the composition and fabric of these domes and to evaluate the reasons for the growth of microbial mats in a largely siliciclastic environment.

1.2.0 Geological Setting

The late Devonian-Carboniferous Horton Group is the basal stratigraphic unit of the Maritimes Basin and is a siliciclastic unit containing conglomerates, sandstones and shales. The Horton Group is located near Wolfville, Nova Scotia. The Cheverie Formation overlies the Horton Bluff Formation and together they comprise the Horton Group within the Windsor sub-basin area of Nova Scotia (Tibert & Scott, 1999)(Fig. 1.1). The group rests with pronounced unconformity on the Lower Paleozoic rocks of the Meguma Terrane and post-dates terrane accretion associated with the Acadian Orogeny (Martel and Gibling, 1996). Following the Acadian

Orogeny, an extensional phase, approximately 355 Ma, opened up the Maritimes Basin of Atlantic Canada, forming half grabens in which the Devonian-Carboniferous Horton Group was deposited. The regional geology is shown in figure 1.2.

Palynological data reflect a moderately humid climate (Tibert and Scott 1999).



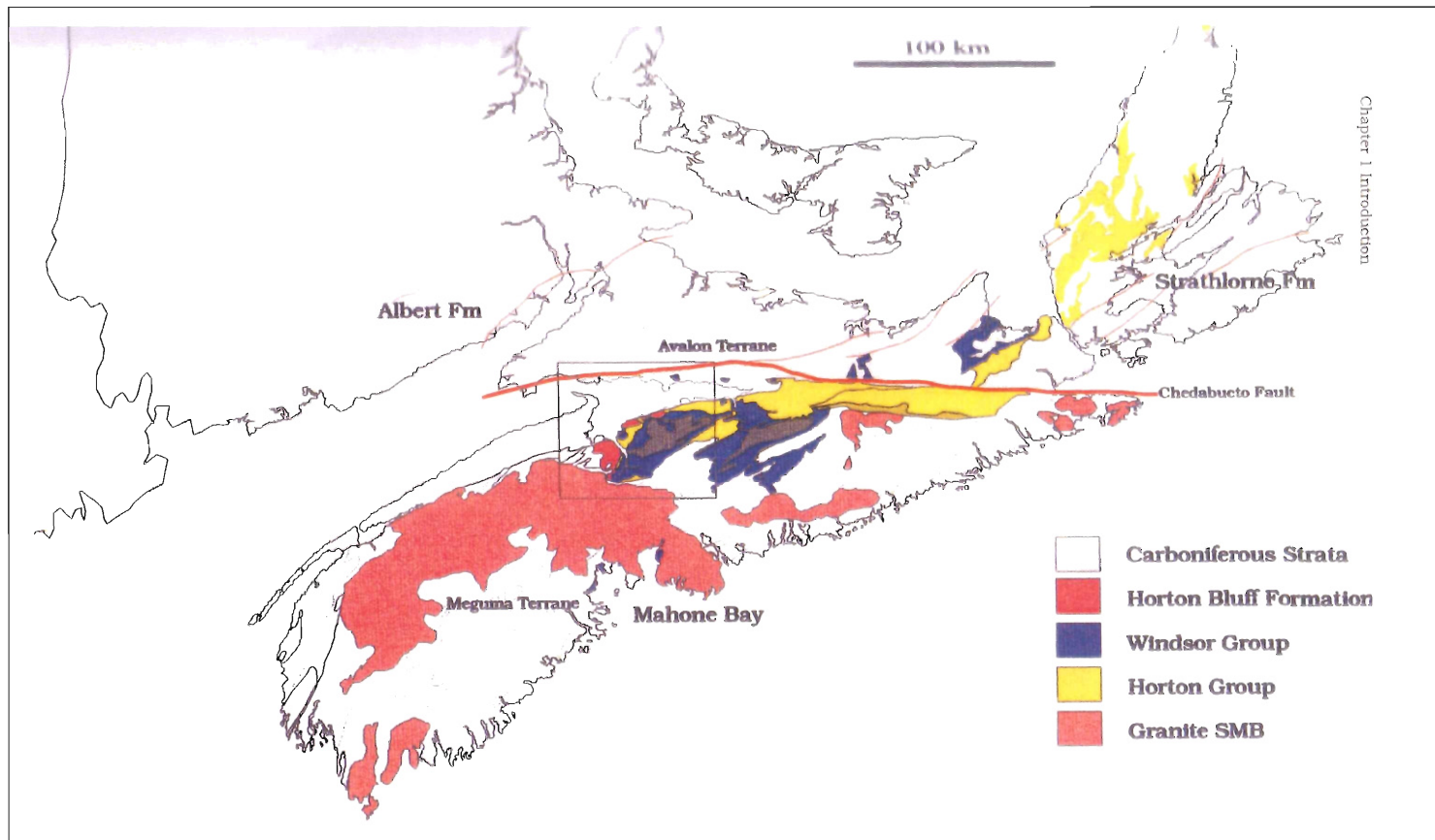


Figure 1.2- The regional geology of Nova Scotia showing the different groups and formation, along with the South Mountain Batholith granitic intrusion. Study area in within black square. (After Tibert, 1996)

Martel and Gibling (1996) further divided the Horton Bluff Formation into four members: the basal Harding Brook Member, the Curry Brook Member, the Blue Beach Member and the Hurd Creek Member (Fig. 1.3). The Harding Brook Member was deposited in a braided-fluvial environment and the Curry Brook was deposited in deltaic channels and interdistributary lakes. The Blue Beach Member was deposited in large, wave-dominated lakes and/or restricted marine bay. The Hurd Creek Member was deposited with some deltaic influence in a brackish bay. Tibert and Scott (1999) later interpreted the Blue Beach Member to represent an ancient marginal-marine brackish bay.

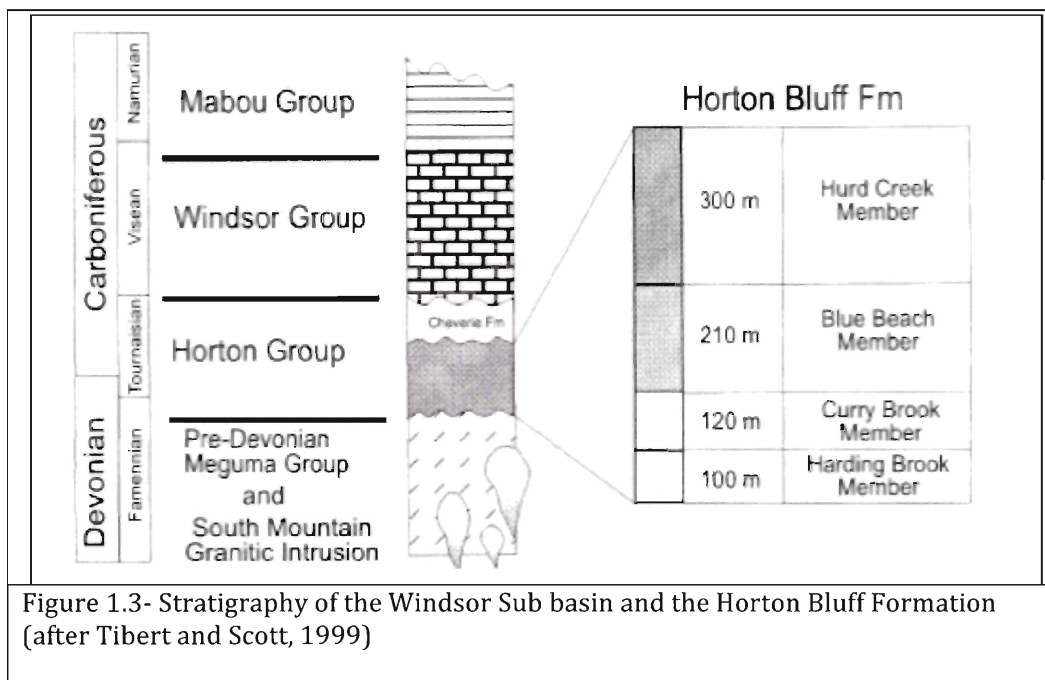


Figure 1.3- Stratigraphy of the Windsor Sub basin and the Horton Bluff Formation (after Tibert and Scott, 1999)

1.3.0 Previous Work

1.3.1 Blue Beach Member- Stratigraphic Background

The study area is located within the Blue Beach Member (BBM) of the Horton Bluff Formation. The cycles in the BBM contain green mudstone, carbonate-rich duricrust, interbedded claystone-siltstone and sandstone layers, and thick sequences of grey and black shale (Martel and Gibling, 1991). They show a marked absence of siderite nodules common in the other three members. This member is notable for the presence of ostracodes and disarticulated fish material. The different beds of this member include asymmetric-coarsening upward cycles, planar lamination, wave ripples, and abundant plant fragments and large tree stumps (Martel and Gibling, 1996). Tibert and Scott (1999) noted some key differences between the BBM and the other three members in which marine ostracodes occur almost exclusively in the lower BBM. Also reported by Mamet (1995), marine echinoderm fragments were found within an oolitic bed in the Horton Bluff Formation just above the designated study area.

1.3.2 Blue Beach Member- Depositional Environment

The depositional environment interpreted by Martel and Gibling (1991) was a large, wave-dominated lake representing an upward transition from offshore clay shales to nearshore/shoreline sandstones and siltstones. The presence of wave ripples, hummocky cross-stratification and groove casts indicate that wave action occurred in the shallow-water parts of the cycles.

The BBM, was interpreted by Tibert and Scott (1999), to be a restricted marine embayment with episodic brackish environments. Tibert (1996) looked at

the ostracode and foraminiferal taxa within the BBM. Studies show that the dominant parameter that limits ostracode species is salinity and they can indicate different hydrologic energy zones within ancient nearshore-marine stratigraphic sequences (Tibert 1996). The ostracodes in this member were opportunistic, euryhaline-marine biotypes common to Carboniferous seas (Tibert, 1996).

This suggests that the BBM had a marine influence with the rise and fall of the Carboniferous sea that separated Atlantic Canada from Western Europe. These transitional environments were often too harsh for most stenohaline organisms to survive and resulted in a suite of tolerant and adaptable eurytopic brackish-water organisms that flourished in response to wide-ranging salinity and temperature changes and hydrologic conditions (Tibert and Scott, 1999). The presence of microbial structures is in accordance with settings of brackish environments due to their tolerance for those types of conditions.

1.3.3 Blue Beach Member- Microbial mats and Stromatolites

No previous work has studied microbial mats or stromatolites in the Blue Beach area. The domal mounds have probably been overlooked as concretions. Microbial mats are often difficult to identify on bedding surfaces due to similarities in appearance to ripple marks. Recently, these mats have been uncovered from the cliff due to erosion and are located on a fine-grained sandstone-bedding surface.

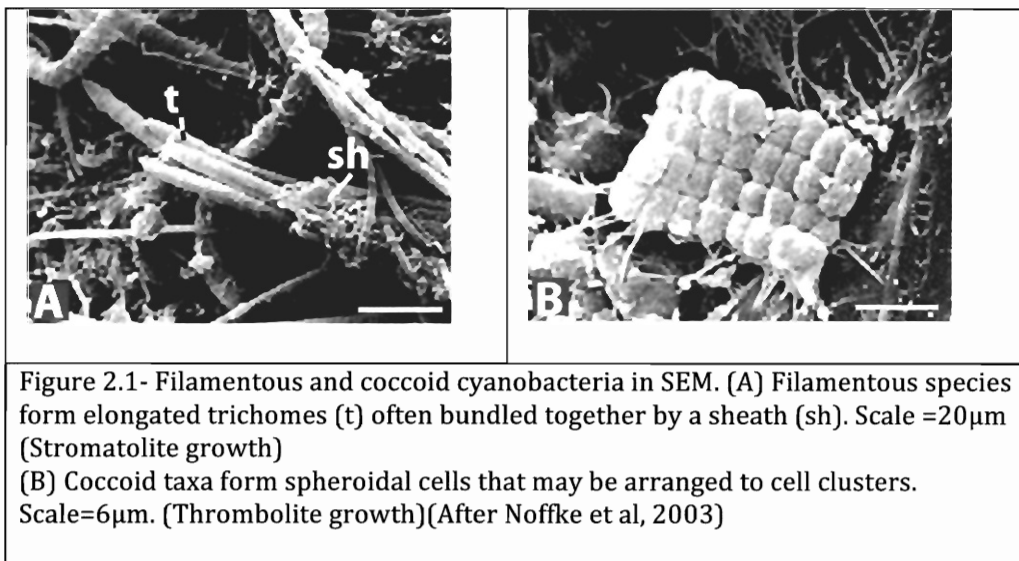
1.4.0 Objectives

This thesis examines the megascopic structures of microbial mats and stromatolites in the field and microscopic details in thin section in order to identify the different morphologies of the stromatolites and to better understand the depositional setting for these microbial structures. Thin sections provide petrographic properties of these samples (e.g., matrices, cements, grain types and size, mineralization), yielding information pertaining to their local paleo-conditions. XRD analysis is used to confirm minerals identified in thin section, and to test for the presence of calcite, dolomite, quartz and minerals that are difficult to identify in thin sections. Although the project only deals with a small stratigraphic interval, understanding the physical sedimentary parameters that control the formation and preservation of microbial structures in siliciclastic environments can facilitate exploration for biological signatures elsewhere in the formation. The structures may have contributed to stabilizing the Horton Bluff sediment surface during deposition, with implications for interpreting the succession.

Chapter 2.0- Microbial Mat and Stromatolite Background

2.1.0 Introduction- Microbes

Laminated sedimentary rocks representing microbial mat and/or stromatolite development are remarkable fossils and represent microbial biomineralization processes (Spadafora et al, 2010). Benthic cyanobacteria are photoautotrophic microorganisms that are known from early Archean to the Recent. Microbial activity is recognized for playing an important role in defining and modifying bedding surfaces by responding to sediment dynamics (Noffke et al., 2003). There are two distinct morphological types of microbial growth seen using a scanning electron microscope (SEM)(Fig. 2.1): A) filamentous species that form elongated cell chains called trichomes which is the typical growth of stromatolites and B) coccoid species that form spheroidal cells often arranged into cell clusters called mesoclots, which are typical for thrombolite species.



The microorganisms biostabilize, baffle, trap and bind loose grains into a mesh-like framework and can stabilize fine-grained sediment (Noffke et al, 2006; Noffke et al, 2008). Biofilms or bio-laminates form through the process of enveloping the mineral grains with organic coatings composed of cells plus their extracellular polymeric secretions (Noffke, 2009). Biofilms grow to form thick organic layers and can cover a large surface area, forming microbial mats (Fig. 2.2). The microorganisms also grow upward in a dome-like manner when there is competition for light, and these structures are termed stromatolites. Microbial mats are known as filamentous microorganisms because they entangle and attach sand grains to form a flexible, leathery, or felt-like mesh of sediment and carbonaceous material.

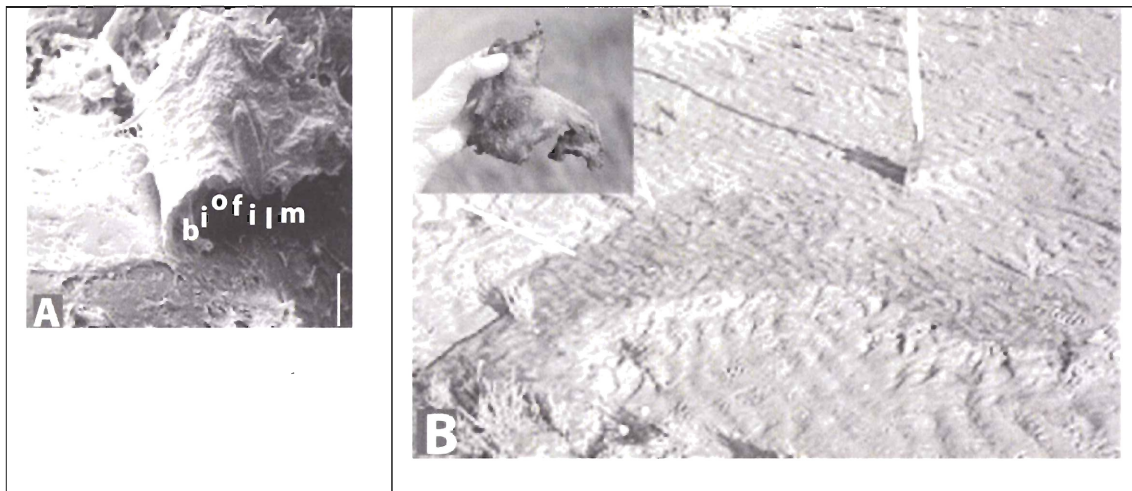
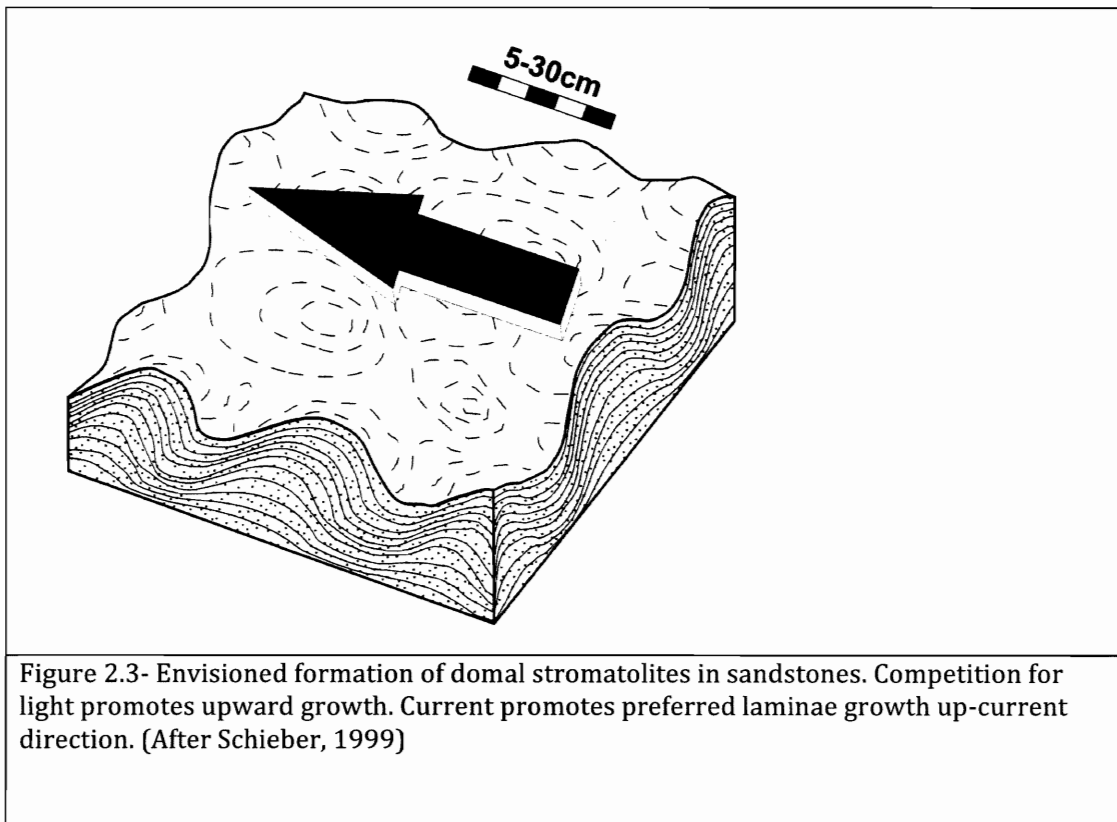


Figure 2.2- Epibenthic cyanobacteria form biofilms and microbial mats. (A) Biofilms are organic coatings that consist of the cells and their slimy, adhesive 'extracellular polymeric substances'. This biofilm envelops a quartz grain. SEM scale=20 μ m. (B) A microbial mat patch overgrows ripple marks of a sandy tidal flat. Scale=blade of spade (20-cm wide). The small picture shows a piece of the coherent, carpet-like microbial mat. (After Noffke et al, 2003).

The domes of stromatolites seem to be influenced by the rates of sediment supply because few organisms can survive rapid deposition. The geometry of the laminae within the domal structures often display periods of sediment movement and stasis where the microbial community has to re-establish itself again and again on new sedimentary surfaces (Druschke et al., 2009). Depending on how strong the water current is, sediment is moved over the mat surface and trapped by the sticky mucilaginous mat surface, which causes a preferred growth of the stromatolite in an up-current direction (Fig. 2.3).



2.2.0 Geologic Evolution

Microbial communities are thought to have flourished in the marine biosphere, particularly in the Archean and Proterozoic. In marine settings, stromatolites provide ample evidence about microbial activity in carbonate settings, but little information exists about microbial activity in coeval marine siliciclastic-dominated facies (Hagadorn & Bottjer, 1997). Stromatolites and most microbial communities were common throughout the Precambrian in many aqueous environments, however, with the onset of the 'Cambrian flora', grazing and burrowing metazoans fed on the cyanobacteria (Pflugger, 1999).

In the Phanerozoic rock record, sandy matgrounds and associated sedimentary structures appear only sporadically, usually nearshore during intervals when bioturbation was suppressed by bottom-water anoxia and deeper settings (Pflugger, 1999). Inhospitable environments such as anoxic, intertidal, supratidal, hypersaline or thermal settings have hosted microbial mat-building communities after the Cambrian and into the present day. Microbial communities have been a significant focus in sedimentologic studies of Archean and Proterozoic rock fabrics, however, it was not until modern counterparts were found in hypersaline and restricted environments that earth scientists began to understand the critical role of microbial communities (Hagadorn & Bottjer, 1999).

2.3.0 Modern vs. Ancient

Microorganisms are well adapted to extreme environments with varying salinity and can form in almost every habitat: siliciclastic, evaporitic-salty and evaporitic-carbonatic. Microbial mats form in carbonate environments largely from mineral precipitation (Druschke et al, 2009).

In modern shallow marine environments, microbial mats are common on both siliciclastic and carbonate substrates, but stromatolites are less abundant in siliciclastic than in carbonate settings. Siliciclastic environments generally have high sediment mobility, frequent disturbances by waves or tides producing a more turbid water column, and reduced light penetration, which is inhospitable for stromatolite formation (Druschke, 2009). However, modern analogues indicate that microbial communities can become established even in strongly siliciclastic environments, if periods of high sedimentation rates are interrupted by periods of low or no deposition, allowing the resettlement of microbial communities (Draganitis & Noffke, 2004).

Modern and ancient mat communities (Table 2.1) exhibit similar wrinkled surface morphologies, patchiness, and sheared, torn or other mat-related characteristics (Hagadorn and Bottjer, 1999). The height, length, inter-crest distance, and angle of repose of ancient and modern microbial mats are similar.

Ancient Microbial Mat Structures	Modern Microbial Mat Structures
Sub-millimetre to millimetre laminae beneath wrinkle horizons Very fine to fine-grained quartzite Mica-rich bedding plane surfaces Suspended quartz grains near surface and on wrinkle troughs and crests Pyrite and heavy minerals (ilmenite) Wrinkled surface textures, asymmetric crests and troughs, oversteepened wrinkle-crests Surface structures appear contorted, torn or folded Patchy occurrence on bedding planes, but common on many bedding planes at all localities Shallow subtidal environments	Sub-millimetre to millimetre laminae beneath mats Very fine to fine-grained sand Mica-rich mat surfaces Mucilaginous binding, silt and clay preferentially incorporated into mat surface Subsurface pyrite precipitation Wrinkled surface textures, asymmetric crests and troughs, oversteepened wrinkle-crests Surface structures are contorted, torn or folded Patchy occurrences where strong currents, pooling, or bioturbation Stressed marine environments (hypersaline, supratidal, dysaerobic)
Table 2.1- A comparison of ancient and modern microbial mat structures After Hagadorn and Bottjer, 1999	

2.4.0 Stromatolites and Thrombolites- Microbial Structures

In the course of fieldwork, domal structures built by microorganisms have to be objectively described, differentiated and classified (Fig. 2.4). Stromatolites and thrombolites are interpreted as two distinct types of microbial structure, and understanding the differences between them is key to classifying the structures that were observed in the Blue Beach field. Kennard and James (1986) described and defined the types of constructional, mesoscopic constituents that are diagnostic of

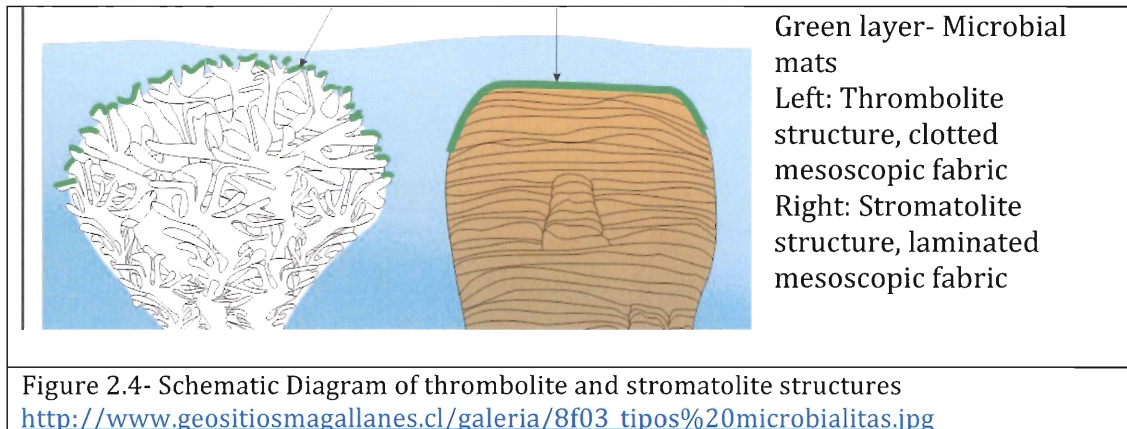
thrombolites and stromatolites. Some of their key findings are highlighted in this section.

Thrombolites first appeared in the earliest Cambrian time, during a period marked by a worldwide marine transgression and in conjunction with the first appearance of the first calcified cyanobacteria. However, the demise of the Lower Paleozoic thrombolites correlates with the onset of a marine regression in early to mid Ordovician time (Kennard and James, 1986). Newly evolved reef-building, skeletal metazoans, algae and mollusks aided in the subsequent decline.

Thrombolites are characterized by a clotted mesoscopic fabric, known as mesoclots, and are constructed by *in situ* calcification of discrete microbial colonies or growth forms of coccoid-dominated organisms (Fig. 2.1B), which are internally poorly differentiated. Detrital particles such as terrigenous silt and sand, peloids, and ooids are sparse or absent within mesoclots, however between these structures, the unbound-sediment pockets are composed of detrital particles. Mesoclots are generally extensively burrowed or bored or both.

Stromatolites, known as the oldest microbial structures on earth were most abundant during the Archean and Proterozoic eons but are still around today in isolated patches around the world that are normally inhospitable to grazing organisms. They are different than thrombolites because they are characterized by a laminated mesoscopic fabric constructed by the episodic growth and sediment-trapping, sediment-binding, and/or carbonate-precipitating activities of mat-like communities that are dominated by filamentous microbes (Fig. 2.1A). Many stromatoids, a diagnostic term to refer to the individual layers or laminae within

stromatolites, are constructed by relatively laterally continuous, well-layered, microbial communities (Kennard and James, 1986). Laminoid fenestrae are long, thin cavities, parallel to the sediment laminae, formed particularly in algal, laminated muds and produced by the decay of organic material (Allaby, 1999). Fenestrae are prevalent within many stromatolites but seldom occur within thrombolites. In addition, thrombolite-forming microbial communities are commonly intimately associated with abundant and diverse metazoans whereas stromatolite-forming microbial communities are usually devoid of metazoans.



2.5.0 Diagnostic Criteria

2.5.1 Field Criteria

Identifying microbial mats in the field is a formidable task. Microbiota may be destroyed after the first few hundred years of burial and modern microbial mats become folded, ripped and disturbed by other organisms, current activity, and slumping (Schieber, 1999). Indicative features (Table 2.2) of microbial activity include wavy-crinkled laminae (Fig. 2.5); cohesive behavior during erosion, transport and deposition (Fig. 2.6); ripple patches; domal structures (Fig 2.7);

impressions of mat fragments; mica enrichment and random mica orientation; and carbon-rich laminae (Fig. 2.8) (Schieber, 1999).

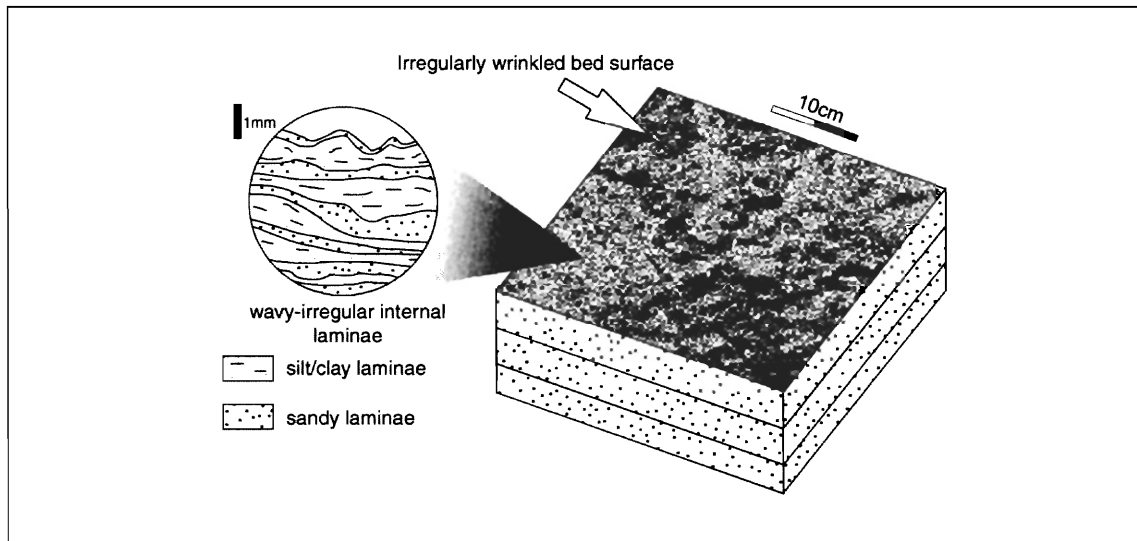


Figure 2.5-Irregularly wrinkled bed surface as observed in sandstones. Detailed view may be microbial mat in origin. (After Schieber, 1999)

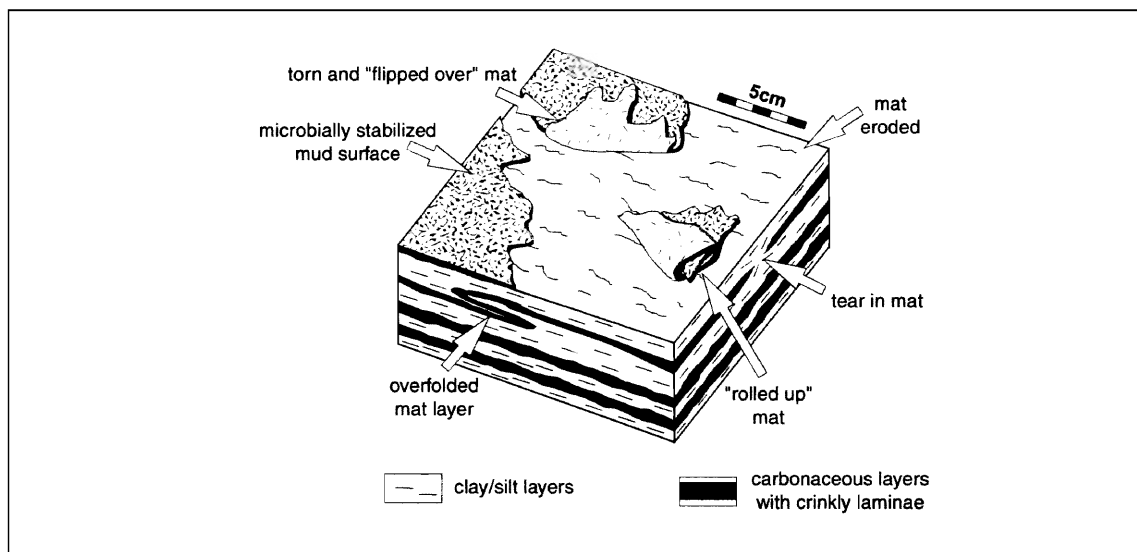


Figure 2.6-Sedimentary features that reflect cohesive behaviour of carbonaceous layers that are suspected of microbial origin. (After Schieber, 1999)

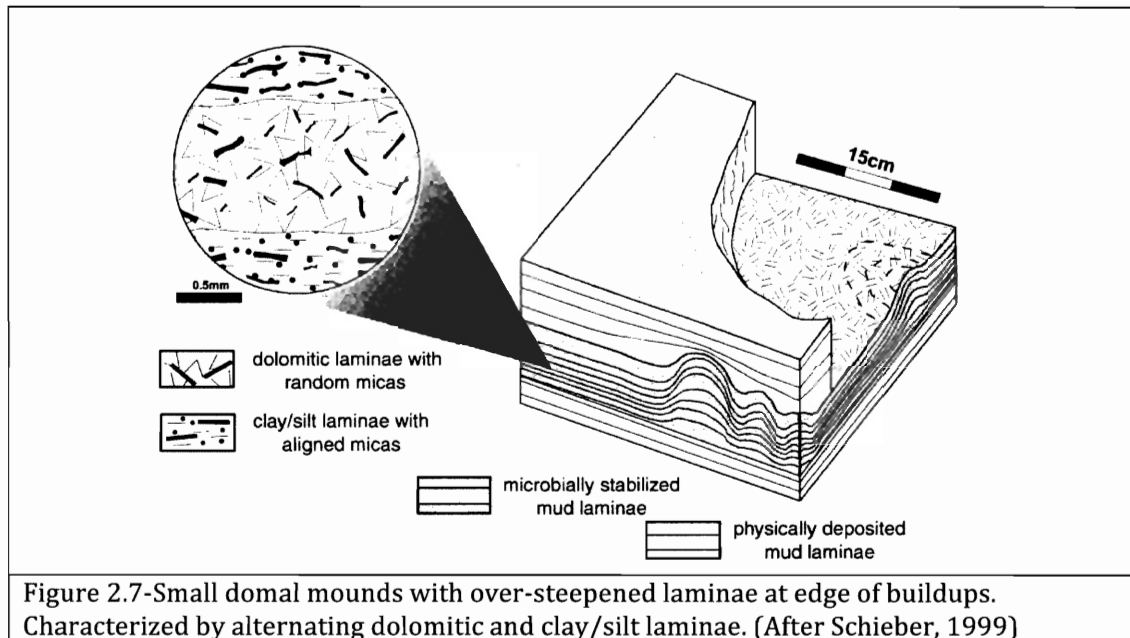
Criteria for recognizing microbial structures in the field were collected by Jurgen Schieber and highlighted in his 1999 paper. His criteria will be used as a

template in producing a diagnostic table for identifying microbial structures in the field during this thesis.

Microbial Mats-Indicative Features	Stromatolites-Indicative Features
<p>Appearance: Oddly contorted, wrinkled, irregular, patchy and over-steepened surface morphologies</p> <p>Cohesive Behaviour: thin sediment layers that were rolled up and about during transport, by stretching and overfolding of thin microbially bound layers</p> <p>Bedding Surfaces: Wavy-crinkly laminae and irregularly wrinkled bedding surface</p> <p>Dolomite cement- mat-decay mineralization</p> <p>Ripple patches- Microbial layer was ripped off during erosion, providing a window to older layers preserved below</p> <p>Occurrences: Both sandstone and mudstone</p>	<p>Appearance: External-Asymmetric domes, grey in color when dominant organic rich carbonate influence</p> <p>Internal- Planar-continuous laminae, wrinkled laminae and dark carbonaceous layers (organic rich)</p> <p>Laminoid fenestrae</p> <p>Laminae at the margin of the dome are steeper than the angle of repose</p> <p>Bedding surface: Laterally linked hemispheroids, horizontal bases and convex upward form</p> <p>Dolomite cement- mat-decay mineralization and random micaceous</p>
<p>Rule out: Wavy laminae being an artifact of differential compaction around micro-concretions, fecal pellets or silt lenses.</p>	<p>Rule out: Thrombolites and stromatoporoids, load structures, large-scale hummocky cross-stratification</p>
<p>Table 2.2- Diagnostic criteria for mat and stromatolite recognition in the field Source of criteria: Schieber, 1999</p>	

Microbial mats that grow as domal stromatolites are easier to identify in the field due to their mounded structure on bedding planes (Fig. 2.7). Microbial mats, whether they are mat-like or dome-like, grow on both fine-grained sandstone and mudstone, which are associated with carbonaceous layers (Schieber, 1999). The bedding surfaces become crinkled due to loading pressure of overlying sediments and dewatering processes of fluid-rich microbial layers. Microbial mats greatly reduce the erodibility of sand and sand movement (Schieber, 1999). Partial erosion

can show windows that reveal the lower rippled layer, resulting in a patchy surface. Stromatolites can be widespread along traceable horizons, whereas microbial mats can be easily overlooked along traceable horizons.

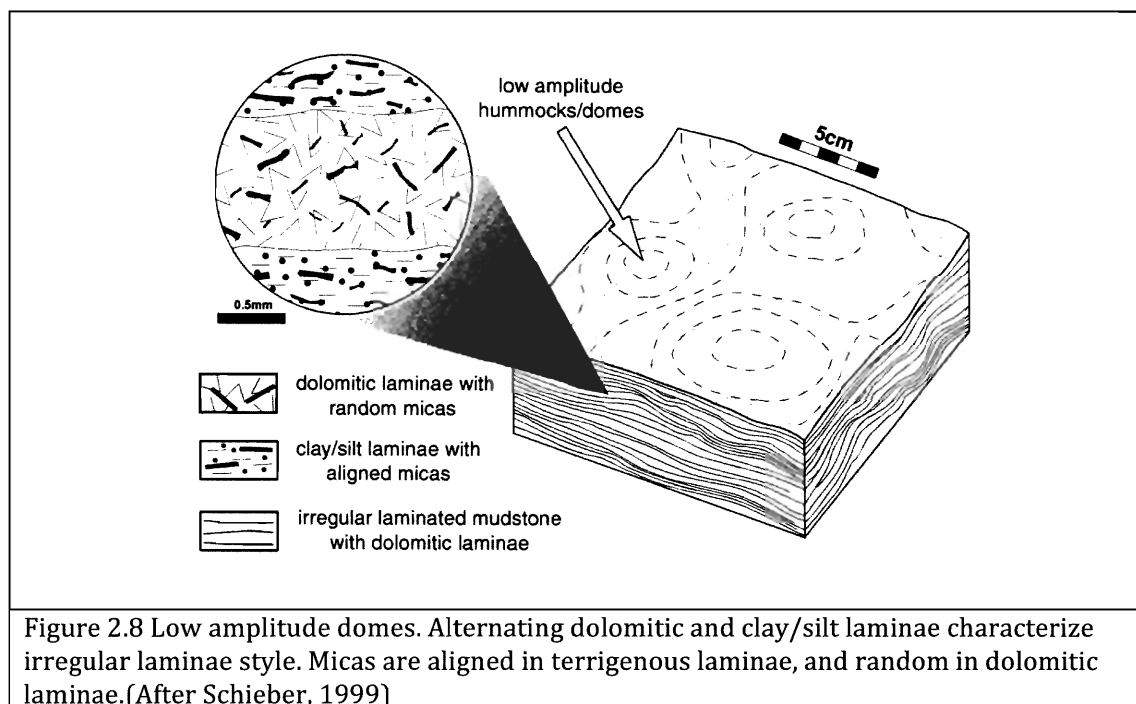


2.5.2 Petrology Criteria

In thin section, microbially induced sedimentary structures should reveal a wavy-crinkly pattern of dark, opaque laminae. Strong evidence for ancient microbial textures includes solitary quartz grains that float without grain-to-grain contact in a dark, laminated matrix. The quartz grains have identical grain sizes to the particles of the substrate beneath the microbial mat. Such solitary quartz grains embedded in the organic mat fabrics are a common textural feature in both ancient and modern microbial mats (Noffke et al., 2006).

Bacterial decay of cyanobacterial filaments beneath a microbial mat strongly enhances carbonate precipitation. Mat laminae in stromatolites are preferentially

dolomitic, due to Mg uptake in the mucilaginous sheaths of filamentous cyanobacteria (Schieber, 1999). Mat-decay mineralization can be a relict feature of the original microbial mat. Sandstones have higher permeability than shales, and this results in the ready metabolism of organic matter by microbes during early burial, when formation water is likely to remove most of the organic material. Due to anaerobic decay of mat material, chemical conditions beneath modern mats in sandy sediments tend to be strongly reducing, leading to the formation of 'anoxic' minerals beneath the mat, ferroan dolomite, being the most dominant. This may be termed 'mat-decay mineralization' (Schieber, 1999). When looking at the samples in thin section, the organic material of the mats is likely to be absent, but dolomitic laminae could be a relict of the original mats (Fig. 2.8).



A diagnostic table (Table 2.3) was organized to identify microbial mat structures in thin section. From previous research of microbial organisms, this table contains the key identifying features that were observed in thin section.

<p>Table 2.3 Textures of microbial structures in thin section Source of criteria: Noffke et al, 2006 and Schieber, 1999</p>
<p>Dark clay-rich laminae, which increase in number towards crinkled bedding surfaces Within thicker parts of the laminae, single (quartz) grains 'float' independently in the opaque matrix without grain-to-grain contact Laminae form a mesh-like microfabric around entangled mineral grains Dolomitic laminae show mica enrichment Alternating dolomitic and clastic/dolomitic laminae and random mica in the dolomitic laminae Oriented grains are particles that originally derive from the sandy substrate underneath the microbial mat</p>

Chapter 3.0- Methodology

3.1.0 Introduction- Research Methods

In recent literature, stromatolites are no longer considered just a phenomenon of the Archean and Cambrian periods, but are part of the greater geological global picture. Largely ignored after the introduction of metazoans, microbial mats were thought not to have survived in the geological record. Contrary to this theory, stromatolites and various other microbial mat-induced structures have been found after the Cambrian and still exist today in places like Shark Bay, Australia. These discoveries allow a greater understanding of fluctuations in different paleoenvironments.

Wrinkle structures and dome-shaped mounds were found located on a single bedding surface at Blue Beach, Nova Scotia. They were found in the Blue Beach Member of the Horton Bluff Formation, which is largely composed of siliciclastic deposits. The evidence of carbonate mounds with horizontal bases and planar to mounded lamination implies a working hypothesis that these mounds are stromatolites and the wrinkle structures are microbial mats. The methodology of this thesis is to incorporate field evidence, petrological work and XRD analysis in order to confirm that these are microbial structures and to gain new insight into the paleoenvironment at the time.

3.2.0 Field Data Collection

Fieldwork was done in late August to early October 2009. A global positioning system receiver (GPS), was used to collect coordinates of the domes to map them on the rock platform. The GPS receiver had a (+ or -) error of 4 m, so to

correct for this measurement error, a distance-measuring wheel was used between the mounds, which had (+ or -) 1 mm error. Work in the field was designed to provide a context for the stromatolites and to document correlative strata within the main cliff face. A large number of samples were collected for further analysis and petrological work.

3.3.0 Facies Observations

3.3.1 Megascope Observations-

A detailed stratigraphic log was compiled over a twelve-metre interval and put into a program called SedLog 2.1.4. The main lithofacies within the column were identified and interpreted. This stratigraphic column was compared to the stratigraphic column produced by Tibert (1996) in order to compare the ostracode occurrences with the microbial occurrences and enable a more accurate paleoenvironment interpretation. Slabs were cut and polished to provide a better view of the internal structure of the mounds. The way-up directions were recorded and photos were taken. Slabs were further cut into thin sections for microscopic observations.

3.3.2 Microscopic Observations-

Twelve thin sections were cut from the rock samples by Gordon Brown at the Dalhousie University thin section preparation facility. The thin sections were selected to highlight different facies within the mounds. Matrix, cement, grain size, sedimentary structures, fossils and mineralization were evaluated using two different microscopes. The Bausch and Lomb binocular microscope was used for low magnification (2X= 6.5mm and 4X=3.5mm in the field of view), in order to get a

closer look at the overall geometry of the laminae. The Leitz Laborlux 12pol petrographic microscope was used for higher magnification (6.3X-2.9 mm, 16X=1.0 mm, 25X=0.8mm and 40X= 0.5 mm field of views). The petrographic microscope was used to determine all the optical properties and grain sizes that were too fine to measure with the binocular microscope.

Carbonate rocks are classified under three main systems: the grain size classification system of Grabau, Folk classification, and Dunham classification. In this thesis, the stromatolitic mounds were divided into four facies following the grain size classification scheme set by Grabau: dololutite (grain size is 2 micrometres or smaller; mud sized); dolosiltite (grain size is larger than 2 and less than 63 micrometres: silt sized); doloarenite (grain size is between 62 micrometres and 2 millimetres: sand sized); and dolorudite (grain size is greater than 2 millimetres: gravel sized). The thin sections aid in refining the facies descriptions and highlighting subtle but important differences between the facies. These facies were important in determining the depositional relationships.

3.4.0 X-Ray Diffraction

X-Ray diffraction (XRD) analysis is done to aid in determining specific mineral assemblages. According to Nesse (2000), the wavelengths used in X-ray diffractometers are similar to the atom spacing in most mineral structures. The similarity in dimensions enables the diffraction of X-rays by regularly spaced atoms, which comprise a crystal lattice. Diffraction maxima produced by layers of atoms transmit the incident X-rays effectively given an appropriate angle of incidence. If the X-ray wavelength and the interplanar spacing between crystals in a crystal

structure are known, reflection angles can be predicted using the Bragg equation: $n\lambda = d\sin\theta$, where n represents the order of reflections, λ represents the wavelength of the X-rays, and d represents the interplanar spacing of atoms within a crystal lattice (Nesse, 2000).

Several steps were required in order to get the samples reduced down to a few tenths of a gram and into a fine powder form. The three specific facies chosen for analysis were fine-grained pale carbonate, dark planar-laminated carbonate, and veins within the mounds. These were individually cut apart using the tile saw and separately kept in different sample bags. These sections of the samples were crushed using the Sturtevant Jaw Crusher, which crushes the sample down to a fine aggregate of material. The sample was further crushed into a coarse-grained powder using the Bico Pulverizer. Finally, the coarse-grained material was ground into a fine powder using a mortar and pestle and this was mounted on an XRD slide. Acetone was used to aid in destroying any contaminants and also to reduce the heat from the mortar friction against the aggregates.

XRD analysis was conducted by putting the sample on a holder that pivots relative to the X-ray tube, allowing the angle of incidence of the X-ray beam to vary from zero to 90° . To record the reflections, the electronic X-ray detector was placed at the angle 2θ . In order to achieve this angle, the electronic X-ray detector was mounted on a concentric goniometer, which moves at twice the angular speed between sample and X-ray tube. As the sample and detector were rotated through the desired range of θ and 2θ angles, the intensity of the reflected X-rays were electronically recorded in the form of an X (2θ)-Y (Intensity-counts/second) graph.

Intensity peaks indicated that the sample contains a mineral with atomic planes, the d-spacing of which is appropriate to reflect X-rays for the particular angle θ . Each mineral possesses a different diffraction pattern that can be identified using the graphic records.

X-ray Diffraction techniques were used to confirm minerals identified in thin section, to test for the presence of quartz, micas, calcite, dolomite and for mineral types that are difficult to identify in thin sections. Any analytical method is ultimately limited by its sensitivity; that is, its detection limit and resolution. The Ocean Drilling project set up an experiment on key minerals to get positive identification of each mineral and a plot of intensity factors versus detection limit (weight percent) was produced (Cook et al, 1975).

After the diffraction analysis was complete, minerals and mineral groups that are commonly found in sediments were actively sought by the computer-analysis program and presented in a graph with the diagnostic peaks of the minerals present in the sample. This XRD analysis does not give mineral percentages within the sample, and a second method was used to get a semi-quantitative measure of the mineral percentages.

The Ocean Drilling Project (Cook et al., 1975) produced a table of minerals actively sought in diffraction data analysis, and this table was used for estimating semi-quantitative mineral percentages. With the computer analysis, a list of minerals was produced and the major minerals were picked to fit the peaks on the graph. After the peaks were picked on the graph, a visual analysis was done to

confirm that all the peaks matched with an identified mineral, after which semi-quantitative measures were completed to estimate mineral percents.

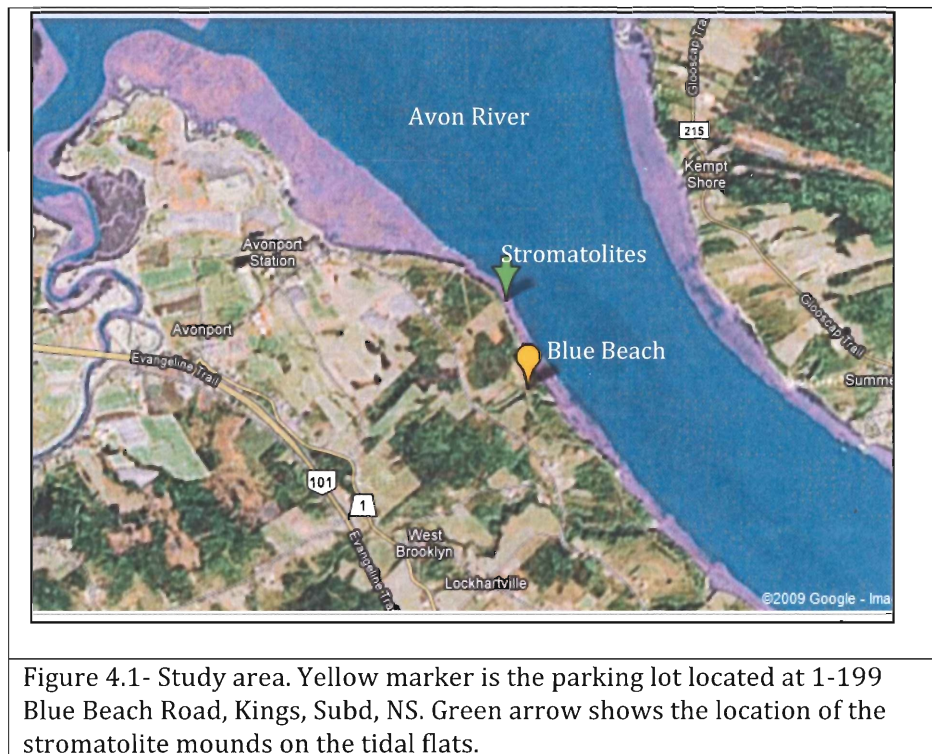
The heights of diagnostic peaks of the major minerals, selected by Cook et al. (1975) as the basis for estimation, were measured with a ruler on the XRD trace, and this measurement was multiplied the by the intensity factor of the mineral to obtain a product. The products for each mineral were added together to get a total product for the sample. The mineral percentages for each sample were calculated by dividing the individual mineral products by the total products.

A combined total for each of the three areas of interest was calculated after each individual sample was completely analyzed. Although the results are semi-quantitative, the combined total allowed the three sample groups to be compared in a reliable manner.

Chapter 4.0- Field Work and Observations

4.1.0 Introduction- Study Area

The study area (Fig. 4.1) is located at Blue Beach, along the Avon River, in central Nova Scotia. The stromatolites are observed to rise from a single bedding surface on the tidal flats, and the same bedding surface, when traced to the cliff face, has eroded down and uncovered microbial mat structures.



4.2.0 Stratigraphy

4.2.1 Stratigraphic Descriptions

Twelve metres of the cliff face were logged into a stratigraphic column (Fig. 4.2). This was done in order to gain a more detailed understanding of the upper part of the Blue Beach Member and to look for microbial mat structures on other bedding planes in association with the stromatolite occurrence on the rock platform.

A traverse along the cliff was set up and the different lithologies were interpreted and categorized into beds.

The facies of BBM, were initially interpreted by Thomas Martel (1990) in his Ph. D thesis. These facies were used as a template when observing the different lithologies in the field. Their cycles were interpreted as progradational in style and represent an upward transition from offshore clay shales (facies 1) to nearshore/shoreline sandstones and siltstones (facies 2), disrupted green mudstone (facies 3), carbonate duricrust (facies 4) and coarse deltaic sandstones (facies 5). Table 4.1 uses the five facies highlighted in a later paper by Martel and Gibling (1991), along with descriptions made in the field during this current study of the Blue Beach Member. Figure 4.2 shows the entire stratigraphic section with the legend attached and Figure 4.3 shows the log broken down with its field descriptions and cycles observed. All five facies are identified within the 12 meters and the cycles are outlined but will be later discussed in 4.5.0 with reference to microbial structures.

The five facies described by Martel and Gibling (1991) paper are:

Facies 1: Grey clayshale:

Grey clayshale varies in colour from medium grey to black, and contains less than 1.5% organic matter. The unit is bioturbated and contains medium- to coarse-grained lags, fish debris and duricrust fragments. The shale is predominantly clay rich. Evenly splitting, fissile clayshale predominates at Blue Beach and includes ostracode, fish and plant material.

Facies 2: Alternating sandstone, siltstone and clayshale

Facies 2 overlies Facies 1 in most of the cycles and is predominantly composed of siltstone and sandstone beds 0.5-12 cm thick, which comprise bedsets up to 60 cm thick. The beds are separated by erosional surfaces and by thin clayshale layers. Siltstones and sandstones are moderately to well-sorted and quartzose. Roots are commonly preserved *in situ* in this facies.

Facies 3: Green mudstone

The facies is composed of olive-grey to greenish-grey and dusky yellow mudstone and silty mudstone. Many of the units contain calcareous siltstone and sandstone beds that display wave cross-lamination, horizontal lamination, and rarely graded beds. Molds of roots and plant fragments are located in this facies.

Facies 4: Dolomite (Carbonate Duricrust)

Three different kinds of dolomite exist in this facies. The first subfacies consists of continuous, planar 5-10 cm thick beds that are commonly structureless and usually overlie facies 1. The second subfacies consists of continuous, sharp-based dolomite layers 15-40 cm that are massive, well indurated and split randomly. The third subfacies consists of nodular dolomite, generally as isolated nodules but locally coalesced into irregular but continuous buff-weathering, massive layers.

Facies 5: Coarse Deltaic Sandstones: This facies consists of coarse-grained sandstones, with trough cross-bedding and ripple cross-lamination.

Lithologies	Descriptions	Depositional Setting
1- Clay Shale- Black or Grey	Convolute bedding Planar lamination Plant material Fissile <i>Fossils:</i> Fish, ostracodes, serpulid worms, foraminifera	Offshore- Deposited from suspension in a quiet environment, below wave base. Fissile nature suggests interstitial waters were anaerobic or dysaerobic. Plant material was washed out to sea and settled slowly. Within the profundal zone of a low oxygen quiescent lagoon.
2- Interbedded shales, siltstones and sandstones.	Convolute and planar laminae, Wave-ripple cross-lamination Mudcracks Load casts <i>Fossils:</i> Microbial textures, Ostracodes Plant Material	Nearshore/shoreline- Wave ripples indicate shallow littoral settings where energies fluctuate, above fair-weather wave base with the clay beds interbedded representing brief periods of deeper water, below wave base. Decelerating waves near the shoreline.
3- Disrupted Green Mudstone	Disturbed (contorted) bedding Conchoidal weathering <i>Fossils:</i> root traces, plant detritus, tree stumps, agglutinated foraminifera	Hydromorphic Paleosols- Lake-fringing or coastal marsh of the shallow marine embayment that was periodically covered by silt and sand layers. Greenish colour (in contrast with dark shales) implies some syndepositional alteration, probably in poorly drained but subaerially exposed settings. Pedogenic in origin.
4- Carbonate duricrust	Concretions: Nodular and tabular	Hydromorphic Paleosols- Carbonate precipitation within pores of water-rich mud formed diagenetically. Nodular formed in the vadose zone of a fluctuating shoreline and tabular formed in the subsurface below shallow water sediment interface
5- Coarse-grained Deltaic Sandstone	Trough Cross Beds Inclined Foresets	Deltaic Distributary Channel and Mouth bar deposits
Table 4.1- Blue Beach lithofacies and depositional interpretations. Criteria from Martel and Gibling, 1991 and Tibert 1996		

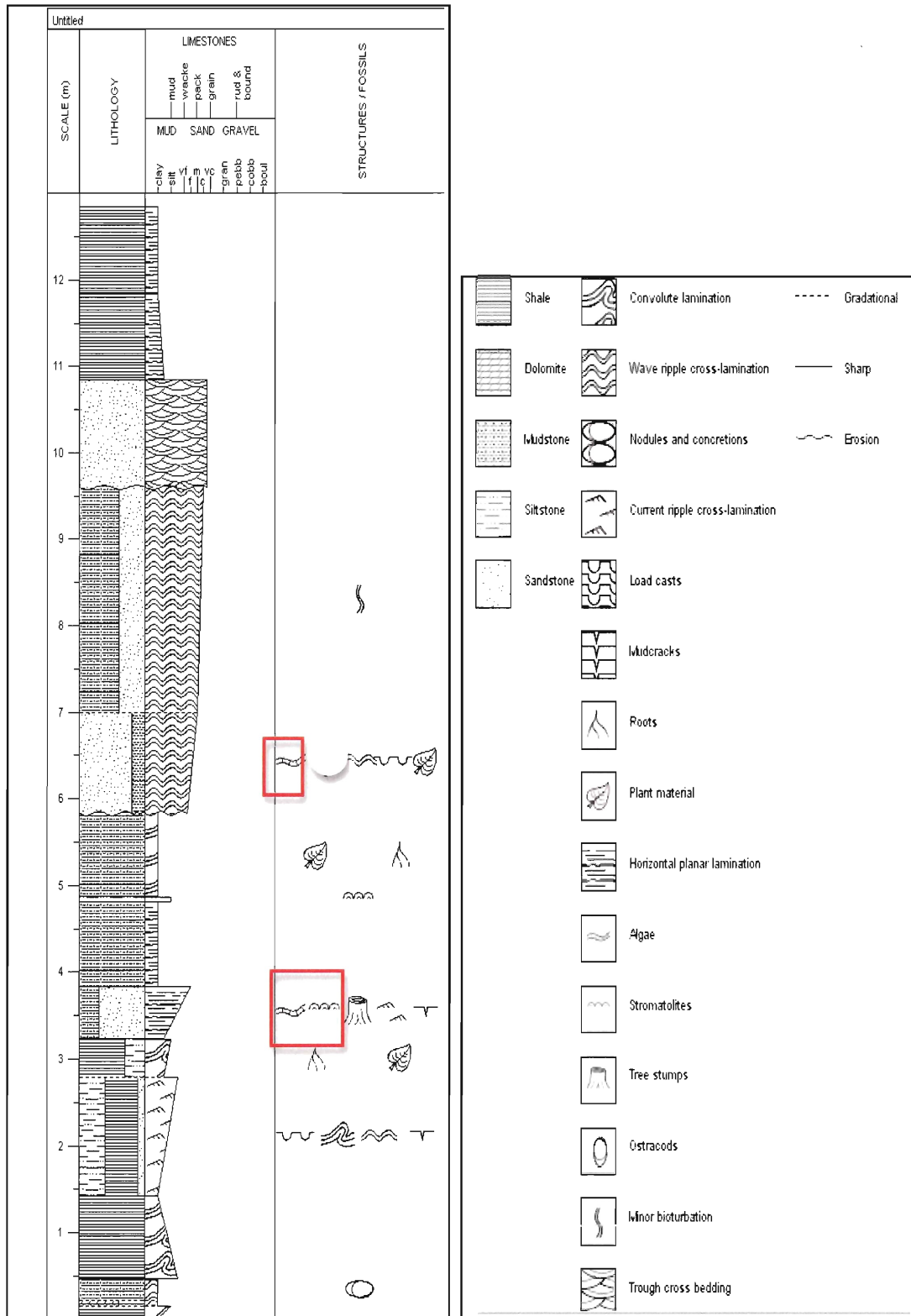


Figure 4.2 Stratigraphic column of study area. Twelve metres was logged and interpreted.

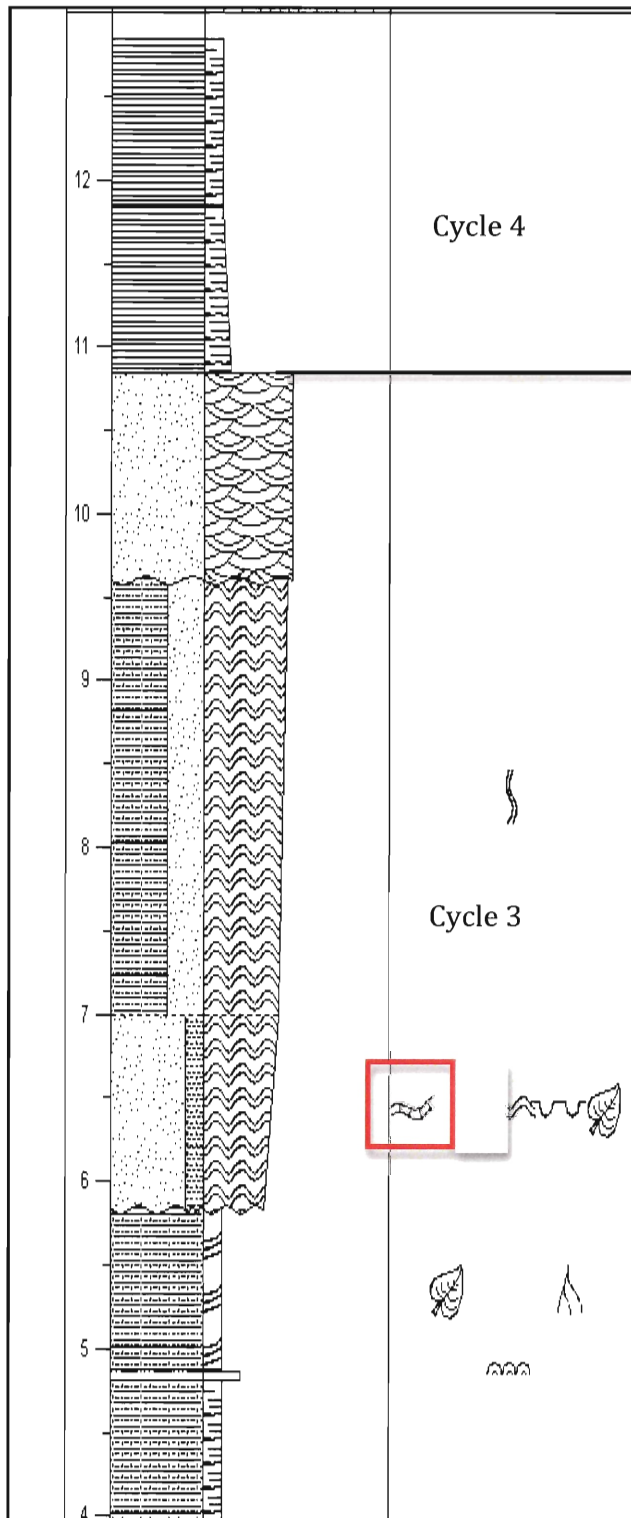


Figure 4.3 Field Descriptions. Horizontal dark lines separate the strata into four shallowing-upward cycles (see text):

11.85m-Top: Facies 1-Black Shale

-Horizontal planar laminae

-Abrupt boundary

10.85m-11.85m: Facies 3- Green mudstone

-Pseudoanticlines

-Planar laminae

-Abrupt boundary

9.6m-10.85m: Facies 5- Coarse-grained Deltaic Sandstone

-Trough cross-bedding

-Inclined foresets

-Coarse to very coarse quartzose sand

-Erosional Boundary

7.0m-9.6m: Facies 2- Interbedded Sandstone and Siltstone

-Coarsening upwards

-Predominantly coarse-grained sandstone

-Minor bioturbation

-Wave-ripple cross-lamination

-Gradational boundary

5.8m-7.0m: Facies 2- Interbedded Sandstone and Siltstone

-Coarsening upwards

-Microbial mats

-Load Casts

-Plant Material

-Erosional boundary

3.8m-5.8m: Facies 1- Black Shale

-Convolute bedding

-Plant material and roots

-Siltstone layer-low domes and finely laminated

-Planar lamination

-Abrupt boundary

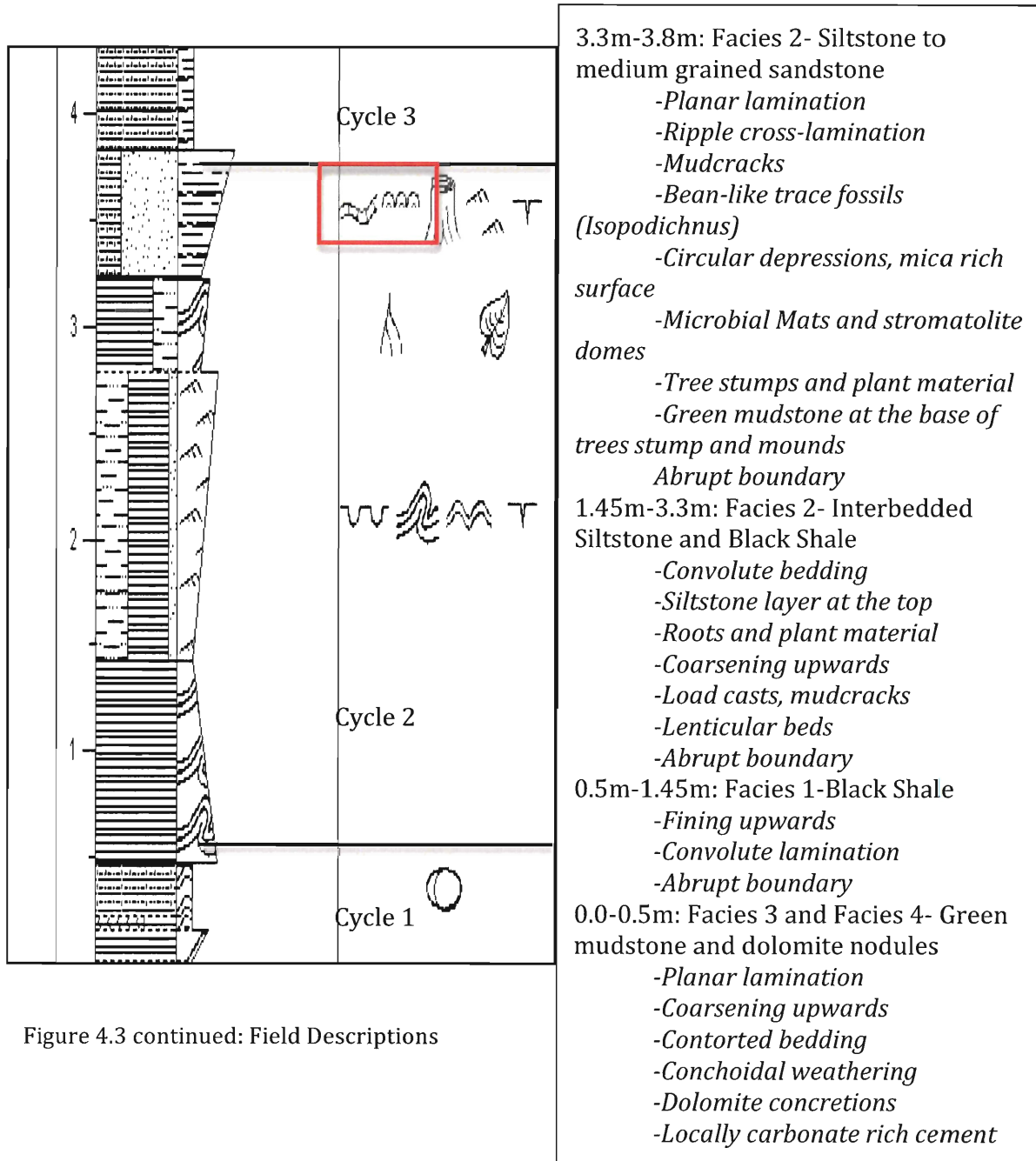


Figure 4.3 continued: Field Descriptions

4.2.2 Stratigraphic Interpretations

The stratigraphic section includes all five facies identified by Martel and Gibling (1991), and the strata comprise part or all of four shallowing-upward cycles (Fig. 4.3). A detailed interpretation of the depositional environment is provided.

The section commences with green mudstone (Facies 3), with planar and disturbed lamination with locally carbonate-rich cement. The greenish weathering contrasts with the dark colour of shale at other levels, and suggests poorly drained but periodically exposed surfaces. The green sediment and the dolomitic nodules (Facies 4) are typical of pedogenic horizons formed in a marsh deposit. Dolomitic nodules are present within this layer. These strata form the top of Cycle 1.

Cycle 2 commences with black shale (Facies 1), which overlies Facies 3 and 4 with an abrupt boundary. The shale has convolute lamination and fines upwards, deposited in a quiet environment, mainly below wave base where fine sediment could drop out of suspension. The apparent absence of benthic fauna suggests that the waters were predominantly anaerobic or dysaerobic. This sediment was deposited most likely offshore in deeper waters.

Facies 1 is overlain by a thick interval of Facies 2, with several coarsening upward cycles of interbedded siltstones and black shale passing upward to a coarser grained unit of siltstone to medium-grained sandstone. The interbedded siltstone and black shale included convolute beds, ripple cross-lamination, roots, plant material, mudcracks and load casts. This facies is interpreted to be closer to the shoreline and influenced by waves with periods of less agitation allowing for the accumulation of clays.

The bedding layer that is the focus of the thesis was part of Facies 2 between 3.3m and 3.8m from the base, within the siltstone to medium-grained sandstone layer. The microbial structures were present on the bedding surface of this layer and showed distinct wrinkle features along with domes that had over-steepened laminae. Within the same layer, tree roots and plant debris are preserved. The domes and tree stump both had their bases starting at a thin disrupted greenish mudstone layer. This layer shows characteristics of shallow water deposition and exposed conditions with mudcracks present. This interval is discussed below in cliff observations.

Cycle 3 commences with strata of Facies 2, which overlies Facies 1 with an abrupt boundary. This section has distinct fissile black shale with planar laminae. A siltstone layer interbedded with this black shale has low domes and is finely laminated. Near the top of this section, there is evidence of plant material or possibly burrows. The fissile, non-bioturbated bottom section suggests predominantly anaerobic or dysaerobic deeper waters. The top of the section that contains burrows and plant debris was a brief aerobic period in shallower waters.

Facies 1 is overlain by another episode of Facies 2 deposition with interbedded siltstone and sandstone. Microbial mat structures were found on these layers, along with plant material, ostracodes, and load casts and wave-ripple cross-lamination within the bed. This layer shows characteristics of a shallow-water deposition and exposed conditions supporting microbial life.

Facies 2 was eroded below a large channel sandstone body, Facies 5, which is interpreted as a large deltaic distributary channel and mouth bar deposit. It includes

trough cross bedding, inclined foresets and very coarse-grained quartzose sandstone. Finally, green mudstone (Facies 3) overlies the large channel sandstone with an abrupt boundary, and this represents the return to a marsh-like setting. Cycle 3 is overlain by black shale at the top of the logged stratigraphic column, marking the base of Cycle 4.

4.3.0 Paleontology

An earlier paleoecological evaluation of the Blue Beach Member demonstrated that there were five fossil assemblages (Tibert, 1996) seen in Appendix A. The stratigraphic interval that was logged in this thesis roughly correlates with cycles 14 and 15 of the stratigraphic log produced by Tibert (1996) also seen in Appendix A. According to Tibert, this stratigraphic section is the top of the Blue Beach Member and contained asymmetrical coarsening upward cycles. He also made note in this section that there were algal bodies apparent on two of the sandstone bedding planes but made no further analysis during his project. It can be assumed that these two bedding planes were the same bedding planes in which algal bodies were observed in the stratigraphic log of this thesis, highlighted with red boxes (Fig.4.3).

The bulk of his samples collected came from the basal 50 metres of the BBM, with sampling intervals at approximately 1 m and after that 50 m, random samples were taken from each cycle up to 215 m. All sedimentary facies were sampled but the majority came from the organic rich shales low in the cycles. The only fossil assemblage that was identified by Tibert (1996) in cycles 14 and 15, roughly the same stratigraphic section in this thesis, was assemblage A5, agglutinated

foraminifera and no ostracodes were found, however, this section was at the randomly sampled bit of the stratigraphic log and increases the possibility that ostracode occurrences could have been missed.

The agglutinated foraminifera are almost exclusively by themselves in the green carbonate rich mudstones, in which ostracodes are absent. Sedimentological features in this mudstone include coarse-grained silty interbeds, micaceous interbeds, carbonate nodules, and desiccation cracks. Euhedral pyrite is prominent in these assemblages. In situ lycopsid tree trunks are also observed in this layer (Tibert, 1996). The microbial features were observed on one of the fine-grained silt-sandstone beds, which was directly above a green mudstone layer that Tibert mentioned.

4.4.0 Cliff Section Observations

The diagnostic criteria for identifying microbial mats and stromatolites were used in the field. The cliff section was the upper portion of Blue Beach Member (Fig. 4.5). Irregular wrinkle structures and domal mounds were observed in the cliff section (Fig. 4.6) within the Blue Beach Member. The bedding unit between 3.3m and 3.8m in the measured section was the focus of this portion of fieldwork. The bedding unit was 0.5 m thick, and was exposed for a horizontal distance of six meters, projecting from the cliff for about half a meter. The bed was composed of fine-grained sandstone and the domes were within the bed while the wrinkle structures were observed on the surface of the bed.

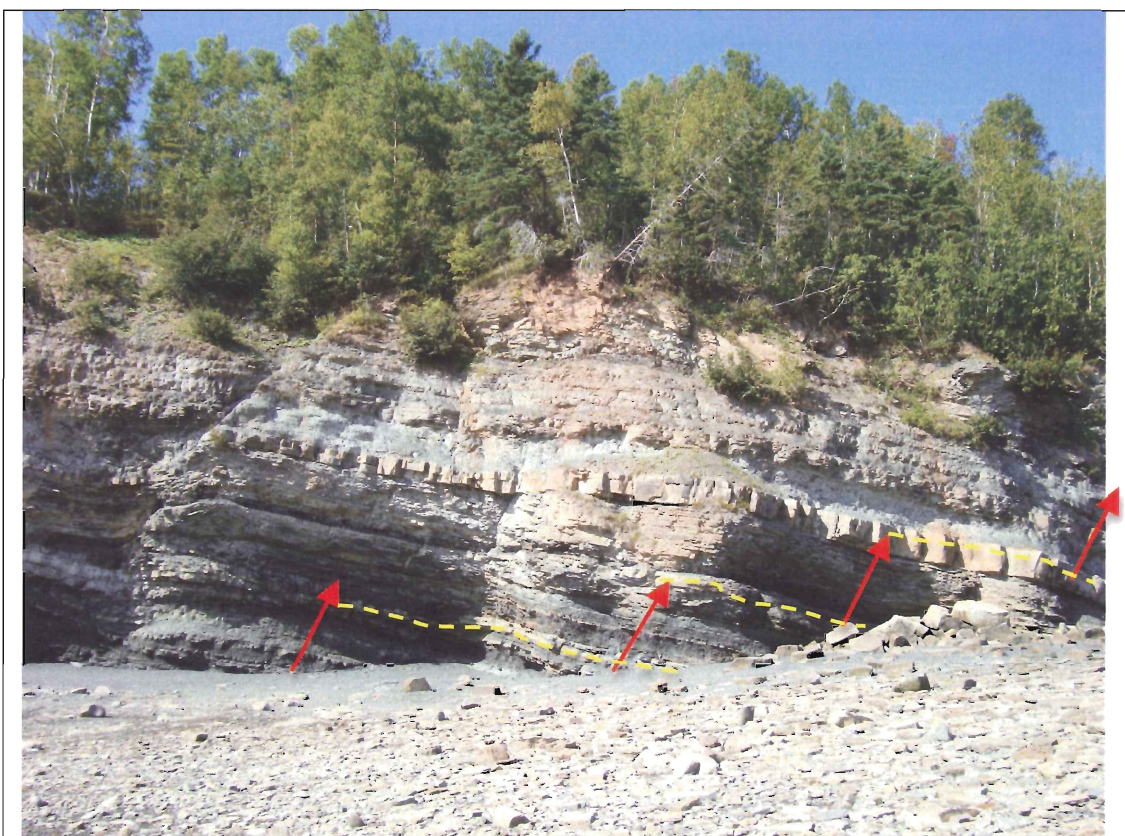


Figure 4.5- Study Area- Cliff section of Blue Beach Member, Horton Bluff Formation. Measured section is shown with red arrow.

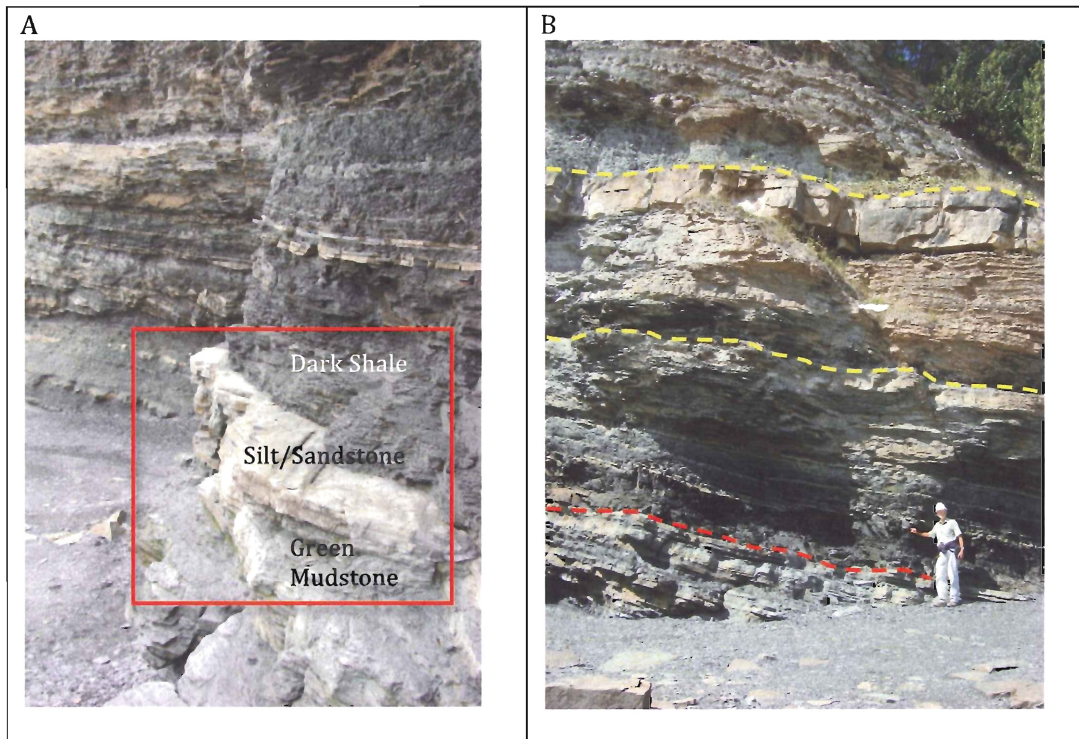


Figure 4.6 Study Section

Exposed bedding surface within cliff section is the top surface of a fine-grained sandstone bed (3.3 to 3.8 m level in Figure 4.2) that consists predominantly of quartz grains and mica. Wrinkle structures and domal mounds were identified on the top surface and within this bed. Tree stumps and gully forms were also identified. Black fissile shale overlies the sandstone layer. Other cycles are highlighted in yellow.

The first observation (Fig. 4.7) made on this bedding surface was its wavy-crinkled laminae and irregular patches. The patches are contorted, wrinkled and have over-steepened surfaces between each crest. The average size of the patches is 8 cm by 10 cm, and the large wrinkles have up to 4 mm of relief and small wrinkles about 0.5 mm of relief. The wrinkle structures have no preferred orientation on the bedding surface and are irregularly distributed, giving them a patchy appearance. The bedding surface is mica-rich seen with a hand lens. The bedding surface has two large gully-like structures, which are parallel to each other and approximately 1 metre long. The gullies were approximately 5 cm wide, 2 cm deep and 1 m long.

Facies 1, black shale infills the gullies. Wrinkle structures near the gullies are sub-parallel with the gully structures (Fig. 4.8).

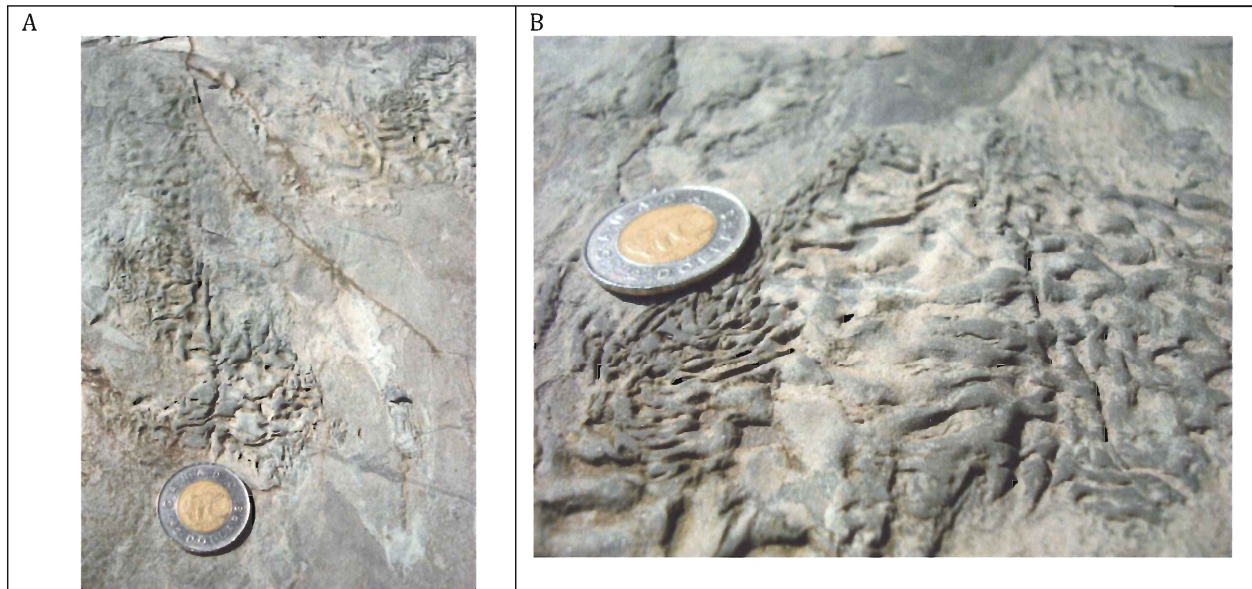


Figure 4.7- Wrinkle structures seen in photos A and B on the fine-grained sandstone bedding surface at the 3.8 m level in the measured section. Note the oddly contorted appearance and irregular crinkled surface. Coin diameter 2.7cm

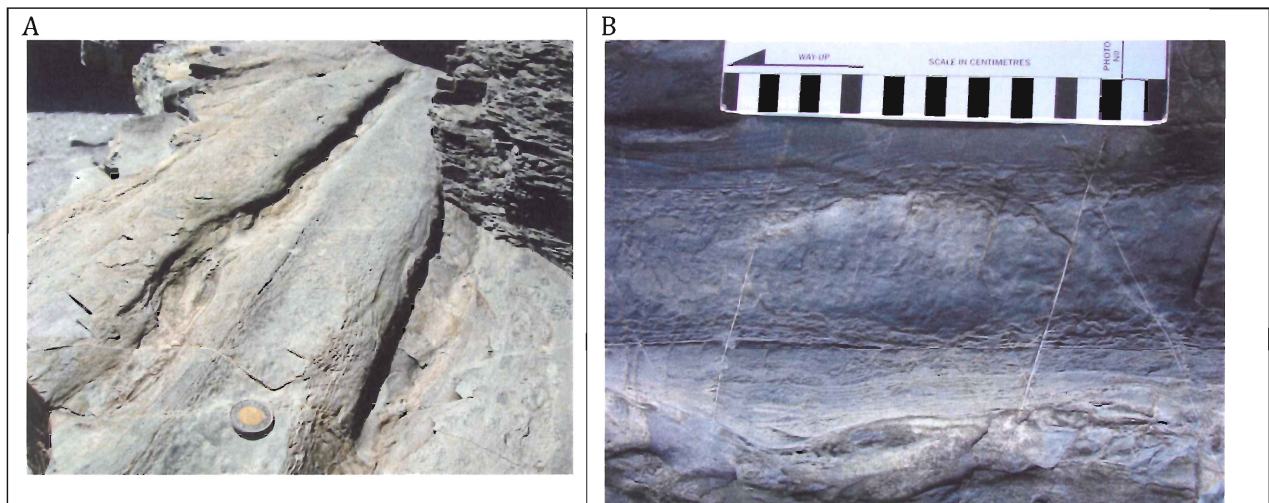


Figure 4.8- Gully structures seen in A, at the 3.8 m level in the measured section, aligned sub-parallel with wrinkle structures. B) Wrinkle structures are aligned sub-parallel. Coin diameter 2.7cm

The second major observation on this bedding surface is the domal structures (Fig. 4.9). These domes are grey, have horizontal bases and laminae that are convex upward on the bedding plane, ruling out load structures that were seen on another bedding plane within the stratigraphic column (Fig. 4.10A). Roots structures were within the green mudstone layer and faulting occurred in this section (Fig. 4.10B). The bases of the domes start on a greenish mudstone layer, and the domal structure is within the sandstone and siltstone layer. The internal laminae are planar through the middle section and over-steepened at the margin of the dome at roughly 35°, giving it an onion-like appearance. The possibility that it was a predominantly thrombolitic structure was ruled out due to its internal laminae. The domes contain no mesofabric but are characterized by a planar laminated fabric.

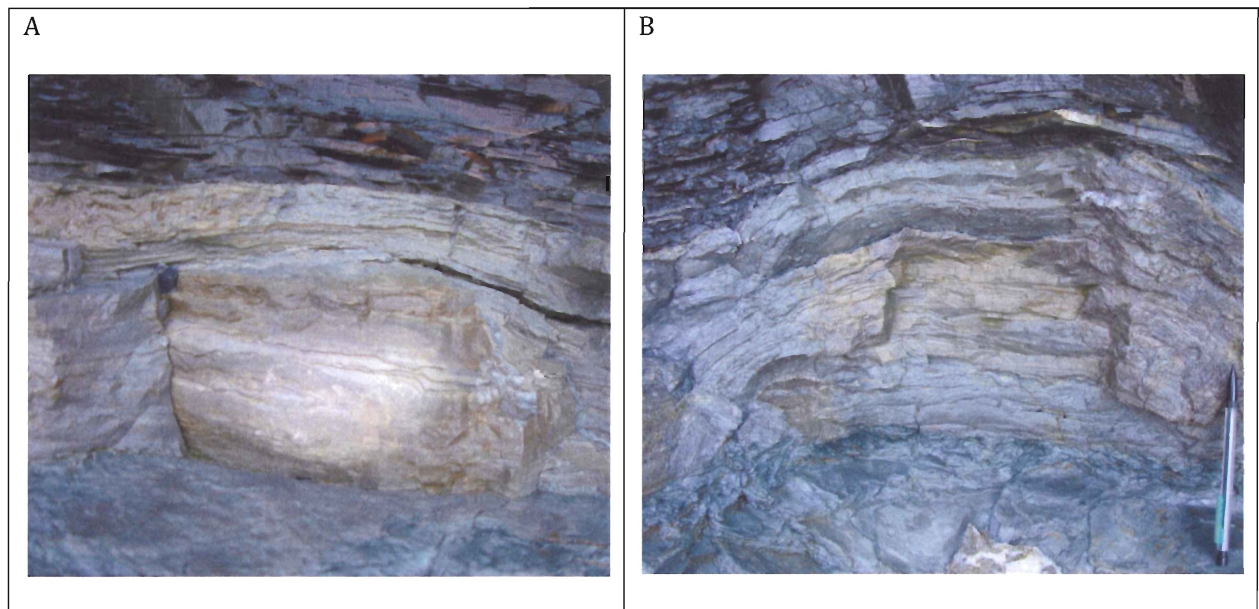


Figure 4.9

Two domal structures preserved at the 3.8 m level in the measured section. Weathered surface shows alternation of dark grey and light grey irregular layers. Horizontal base starts on the greenish mudstone and sand-siltstone laminae are convex upward. Veining at top of dome and black shale above shows an abrupt boundary. Length of pencil 14 cm. Horizontal base of the dome in A) is 20 cm and in B) is 44 cm. Base to top of dome in A) is 9 cm and in B) is 29 cm. Laminae are 0.5-1 cm thick. Angle of laminae at margins of dome in B) is ~35°.



Figure 4.10

- A) Load structure at 5.8 m level in the measured section. The structure is convex down into bedding surfaces below as a result of the overlying sediment being heavier than the underlying sediment, which ultimately loses its fluid content and compacts more easily. The domal structures in Figure 4.9 can easily be distinguished from load structures in the measured section.
- B) Rooted mudstone and fault seen penetrating the siltstone and sandstone layers, at 5.8 m level in the measured section. Length of pencil: 14cm.

About two metres from this domal structure, a tree stump and mudcracks are observed (Figs. 4.11, 4.12). The stump has a circular base that rests on a thin mudstone layer (facies 3). From this disrupted mudstone layer the tree stump goes up through sandstone and siltstone layers, which rest upon (drape) it at an angle. Wrinkle structures are present on the topmost sandstone bedding surface closely adjacent to the stump. The internal part of the stump is pale and massive.

Mudcracks (Fig. 4.12) are observed along the bedding plane further from the stump position, distinguished by their near-hexagonal geometry.

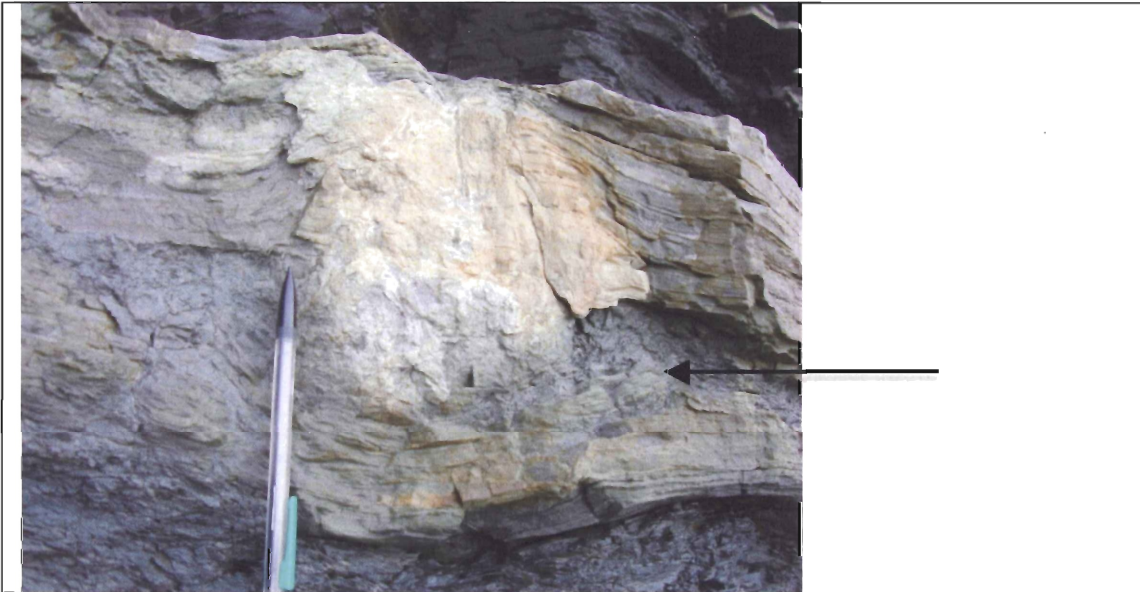


Figure 4.11

Tree stump fossil between 3.3 m-3.8 m levels in measured section. The stump cast is internally massive with laminae draped up around it. It lies on a thin Facies 3 mudstone layer, shown with black arrow. The sandstone and siltstone layer at the top of the photo drapes the sides of the stump. Length of pencil 14 cm.



Figure 4.12

Desiccated horizon with mudcracks observed on the 3.3 m bedding plane, representing subaerial exposure.

4.5.0 Rock Platform Observations

GPS positions were noted for all the individual domes and clusters of stromatolite domes along the bedding surface (Seen in Appendix A). GPS was used to estimate the dome spacing along the bedding plane. Various measurements were made for the domes at each coordinate site. A GPS map was produced to show the general spacing (Figure 4.13). The bedding plane containing the stromatolite domes is located approximately 47.5 m from the cliff face and was followed to approximately 100 m from the cliff (Fig. 4.14). The stromatolite mounds were located along the same bedding surface, a fine-grained sandstone bed, which cropped out on the rock platform at Blue Beach.

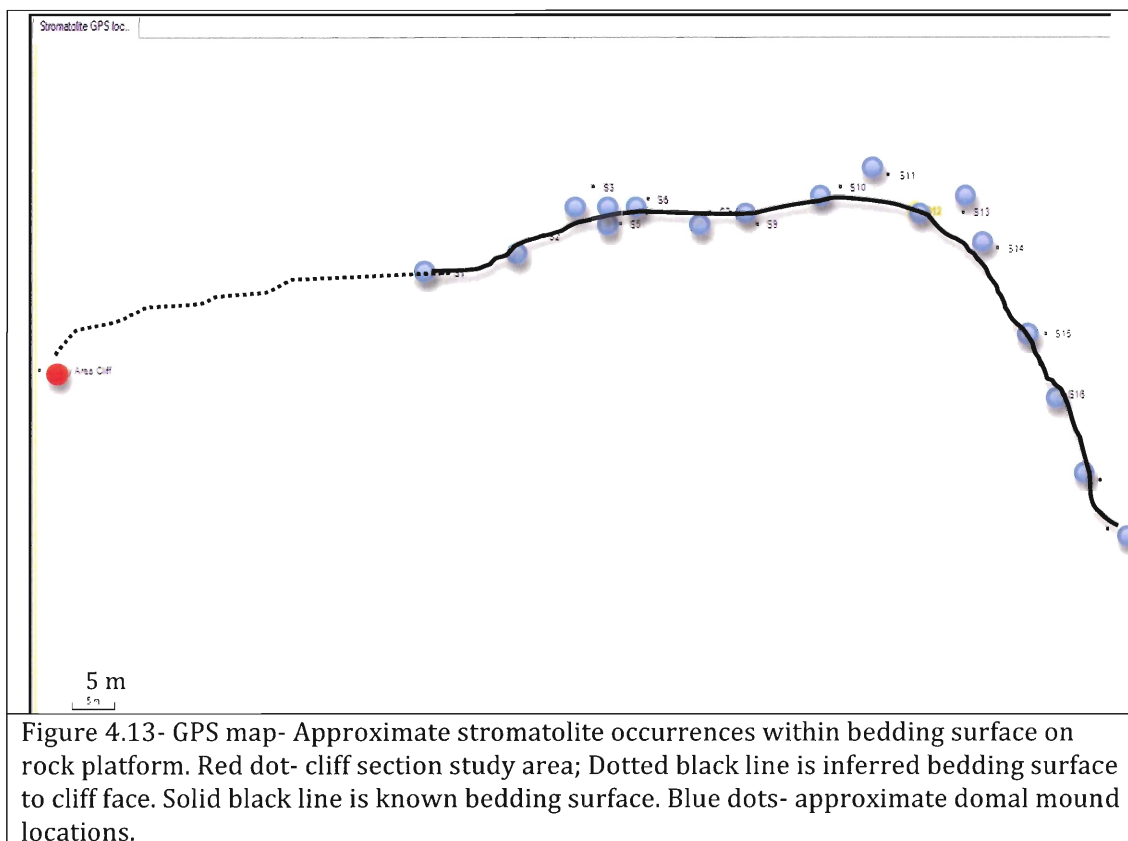
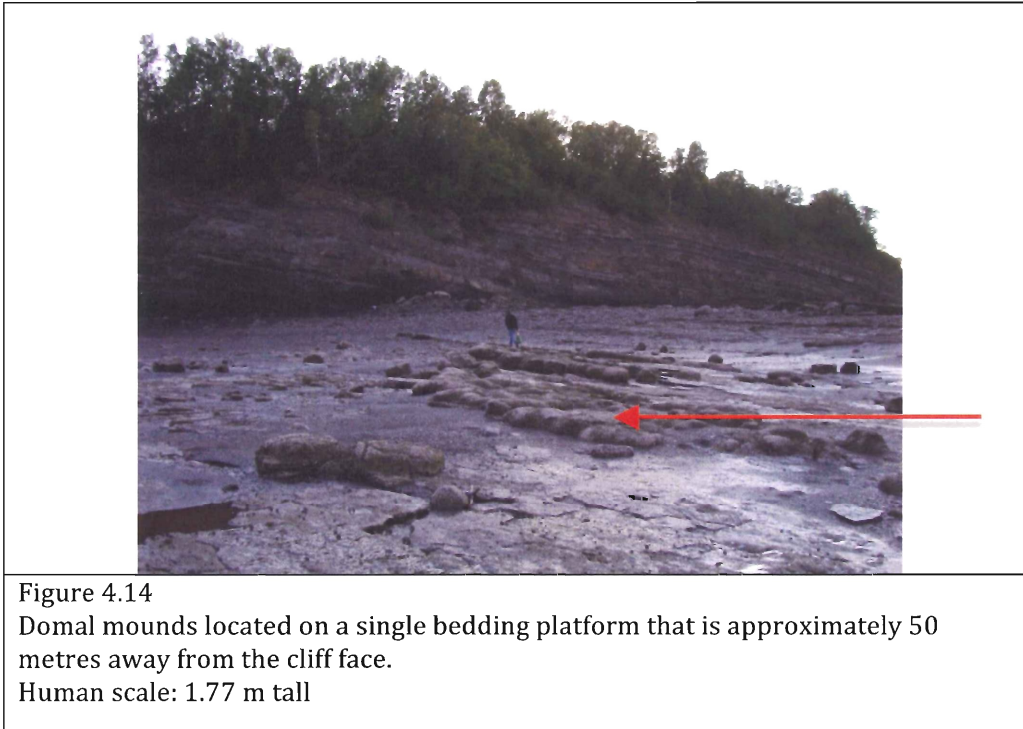


Figure 4.13- GPS map- Approximate stromatolite occurrences within bedding surface on rock platform. Red dot- cliff section study area; Dotted black line is inferred bedding surface to cliff face. Solid black line is known bedding surface. Blue dots- approximate domal mound locations.



The domes range in height from 13-30 cm and have diameters between 35-50 cm. They are weathered grey and are grey to dark grey on a fresh surface. The mounds have horizontal bases, convex upward form, and are laterally linked hemispheroids (Figure 4.15). Internally, the domes are carbonate rich, evident when acid was applied to the surface. The bases of the domes have planar laminae, and the domes have over-steepened laminae at their margins. The upper parts of the domes are massive and pale grey with intricate veining throughout.



Figure 4.15 A) Mounds in clusters forming laterally linked hemispheroids. B) Internal domal structure with dark laminae at base and massive pale layer at top with intricate veining. C) Individual domes associated with fine-grained sandstone, showing convex-upward form. D) Domes in foreground and cliff face in background. Visible portion of hammer in B is 32 cm long.

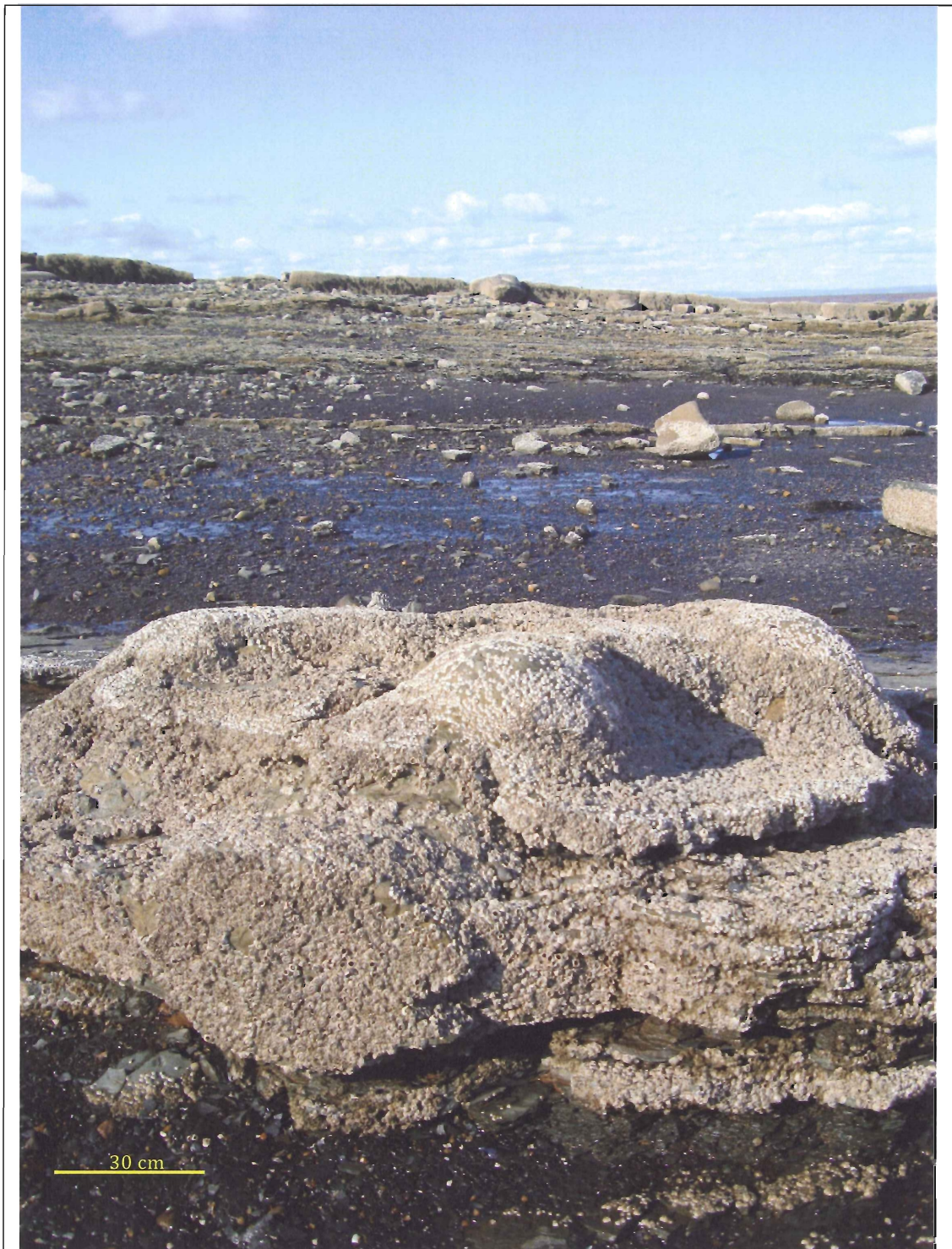


Figure 4.16- Stromatolite mound seen in the fine-grained sandstone layer. The dome itself has a horizontal base and it convex up. Black shale that was above this dome has eroded away.

4.6.0 Megascopic Field Interpretations

In summary, the principal reason for measuring the section and completing all the field descriptions was to link the microbial mats and stromatolites in the cliff section to the stromatolite occurrence in the rock platform and to further interpret the paleoenvironment (Table 4.2). Stratigraphically, the stromatolites and microbial mats occur within the same fine-grained sandstone layer of Cycle 2 observed in the field. The stromatolites grew upwards and the horizontal bases started at the disrupted mud layer. The facies occur in repeated asymmetrical, shallowing upward cycles commonly with abrupt tops. The stromatolite and microbial mats were identified within Cycles two and the three:

Facies 1	Cycle Four - Overall thickness- 1.0 m Offshore black shales (only basal part of cycle measured)
Facies 3 Facies 5 Facies 2 Facies 2 Facies 1	Cycle Three - Overall thickness- 8.05 m Upward transition from offshore shales to nearshore sands and silts with a large channel eroding some of the sand and silt layers. Overlain by a coastal marsh deposits of green mudstone. Microbial features observed on fine-grained sandstone at 5.8 m.
Facies 2 Facies 2 Facies 1	Cycle Two -Overall thickness- 2.35 m. Consists of black shale with sandstone and siltstone sequences. Deeper water offshore setting to nearshore setting with wave ripples. The second facies 2 occurrences contains microbial features, stromatolite mounds and tree stumps between 3.3 m and 3.8 m and correlates to the same bed with the stromatolite occurrence on the modern-day tidal flats. The tree stump and stromatolite mound bases start at a disrupted greenish mudstone.
Facies 4 Facies 3	Cycle One - Overall thickness- 0.5m (only top part of cycle measured). Hydromorphic paleosols, marsh-like setting, exposed subaerially
Table 4.2- Cycles observed in the measured section of Figures 4.2 and 4.3.	

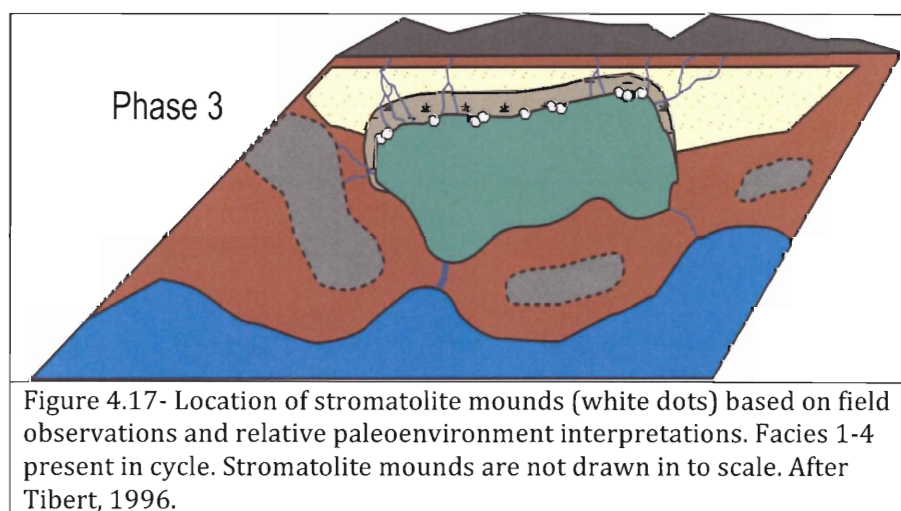
The stromatolites and microbial mats were identified in outcrop using the diagnostic Table 2.2. In the field, the microbial features were recognized mostly by

their appearance and the nature of occurrences on and within the sandstone layer. The microbial mats were apparent with their oddly contorted, irregular patches and wrinkled surface morphologies, and the stromatolites were distinguished for their convex-up geometry and the oversteepened laminae at the domal margins. These domes were distinguished as stromatolites with laminated fabrics rather than thrombolites with clotted fabrics.

According to Schieber (2004), microbial mats influence the depositional fabric of clastic deposits across a wide range of physical, chemical and biological processes. He stressed that these mat-related structures and features are in many ways analogous to trace fossils, and that the former presence of mats can be inferred from observations suggesting sediment properties that would be uncharacteristic for a purely physically deposited sand or mud. Useful features are those that indicate original sediment cohesiveness, tensile strength and erosion-resistance during deposition, and those that allow deduction of original permeability and geochemical behaviour during early diagenesis. The stromatolites have planar laminae within the central core but are oversteepened at the margins with angles around 35° , greater than the angle of repose for subaqueous sediment. This diagnostic feature strongly suggests sediment cohesiveness and erosional resistance during deposition most likely influenced by microbial binding (Webster, 1919). See Appendix A for angle of repose table used for this research.

According to Martel and Gibling (1991), the depositional environment for the sandstone layers was nearshore within shallow-water settings (Fig. 4.17), interpreted later by Tibert and Scott (1999) to be part of a brackish marine

embayment during phase 3, which will later be discussed. Tibert (1999) found marine ostracodes within the black shale above the siltstone/sandstone layer that contains the stromatolites, bringing evidence that this stratigraphic interval experienced intermittent marine influence and possible hyperhaline conditions. Thus, the microbial mats and stromatolites on and within the nearshore sandstone layer probably formed in a hyperhaline environment but may also have been influenced by freshwater, being situated at the top of a progradational cycle and associated with tree stumps, desiccation cracks, and gullies. Freshwater and seawater mixing may have resulted in inhospitable conditions for grazing organisms, promoting the preservation of the microbial structures. The stromatolite growths are inferred to reflect higher levels of wave or current energy (which favours more rapid syndepositionary trapping and buildup of particles) whereas the microbial mats on planar surfaces are inferred to reflect lower energy levels (Hoffman, 1976). The close proximity of domes and flat-lying microbial mats suggests that similar micro-organisms were responsible for both types of occurrence, although this cannot be proven.



Chapter 5.0- Petrology

5.1.0 Introduction- Microscope

Twelve samples, representing separate domes, were collected along a 50 m traverse across the bedding surface on the modern tidal platform for detailed analysis, and labeled FG-1 to FG-12. Thin sections were taken from different areas of interest to observe the sedimentary structures, the bulk mineralogy and different microfacies within the stromatolites. The overall geometry of the laminae and mineralogical properties were observed under the microscope.

A four-step observation process was organized to understand the overall morphology of the stromatolite mounds. First, the polished slabs were observed with a hand lens for colour changes and lithology differences (laminated or massive), and the total thickness of macroscopic units was recorded. Second, the relevant thin section was located with respect to the polished slab from which it was cut, for a reference point. The overall geometry of the laminae was observed under the binocular microscope.

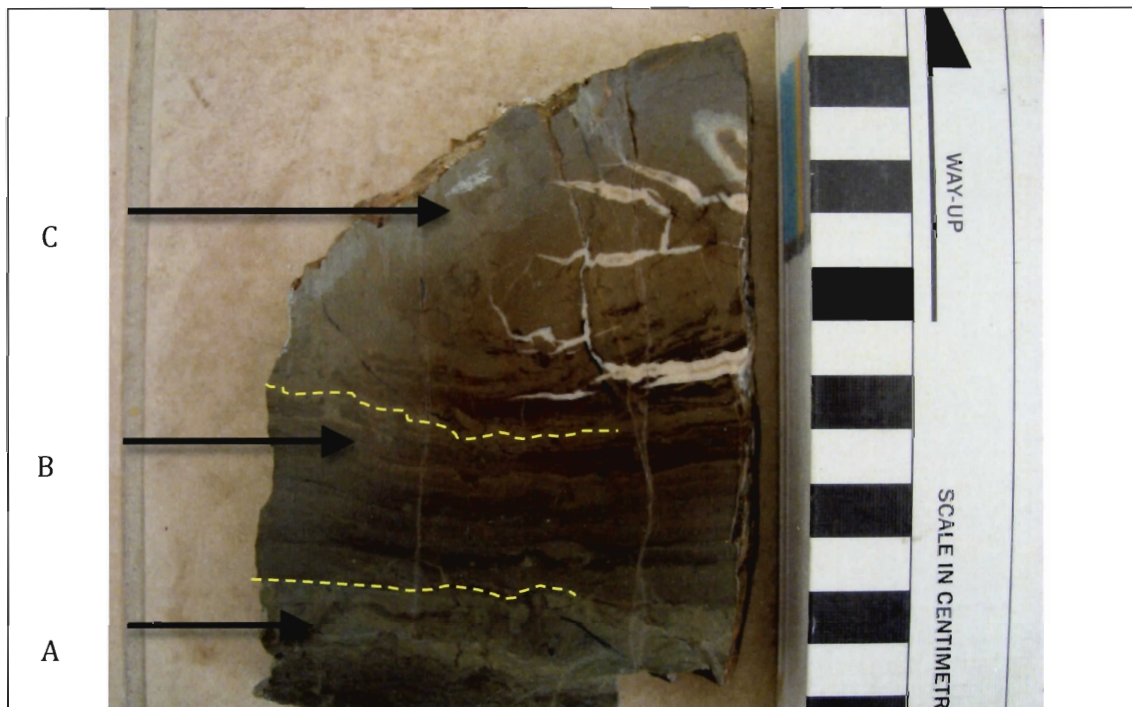
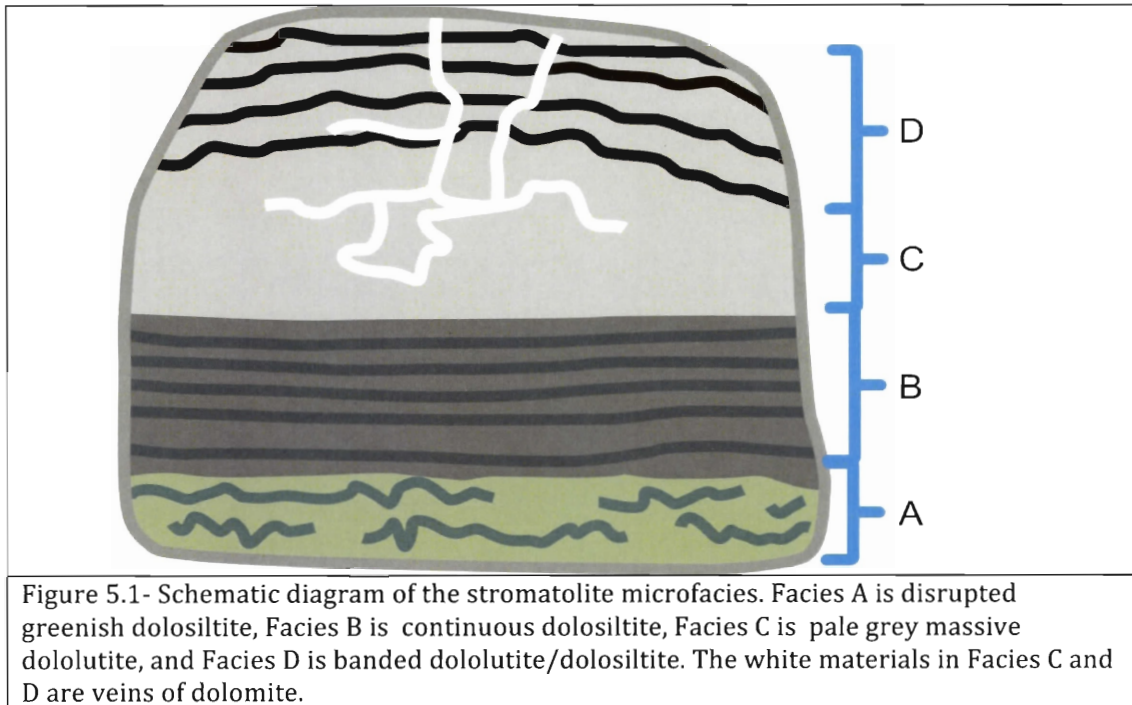
Third, the thin sections were observed under high magnification with an optical microscope. These observations covered mineralogy, thickness of laminae, optical properties and sorting, leading to a microfacies classification. Grains less than 10 μ m in size were considered part of the matrix. Fourth, XRD results were obtained for crushed materials from specific slabs selected on the basis of thin-section analysis, and were used to confirm minerals identified in thin section and to test for mineral types that are difficult to identify in thin sections. Finally, an interpretation of the paleoenvironment was made for each microfacies identified.

5.2.0 Slab Observations

Twelve polished slabs were analyzed and classified into four microfacies. The four microfacies were named for their grain size and the nature of the stratification. These microfacies were labeled with a letter scheme to differentiate from field-scale facies that were observed in the cliff section as a whole. As noted later, dolomite is the most abundant mineral within the stromatolites, and the terms dolosiltite and dololutite were used in a classification that emphasized their carbonate content.

The stromatolites in all slabs show a similar upward trend of microfacies (Fig, 5.1). Facies A is the light greenish-grey disrupted layer at the base and is classified as discontinuous dolosiltite. This layer is overlain with an abrupt boundary by a dark grey, well-laminated layer, Facies B, classified as continuous dolosiltite. Facies B is gradationally overlain by a massive pale grey layer, Facies C, which is classified as dololutite and contains an intricate veining system of dolomite that locally penetrates into the dark laminated layer of facies B. Facies C is gradationally overlain by thick interbedded pale grey massive laminae and dark grey-black laminae, classified as banded dololutite/dolosiltite (facies D). Facies C and D are the only layers that have thick vertical and curved veining throughout.

The four microfacies were measured and ranges of thicknesses were observed between the twelve different samples. The samples were collected from various locations on the exposed bedding plane, and the thickness of the microfacies varied depending on where they were situated. The range of thickness of facies A was 1 cm-3 cm; facies B was 2.5 cm-5.5 cm; facies C was 3 cm-5.5 cm and facies D was 4 cm- 8 cm. The facies observations can be seen in Table 5.1.



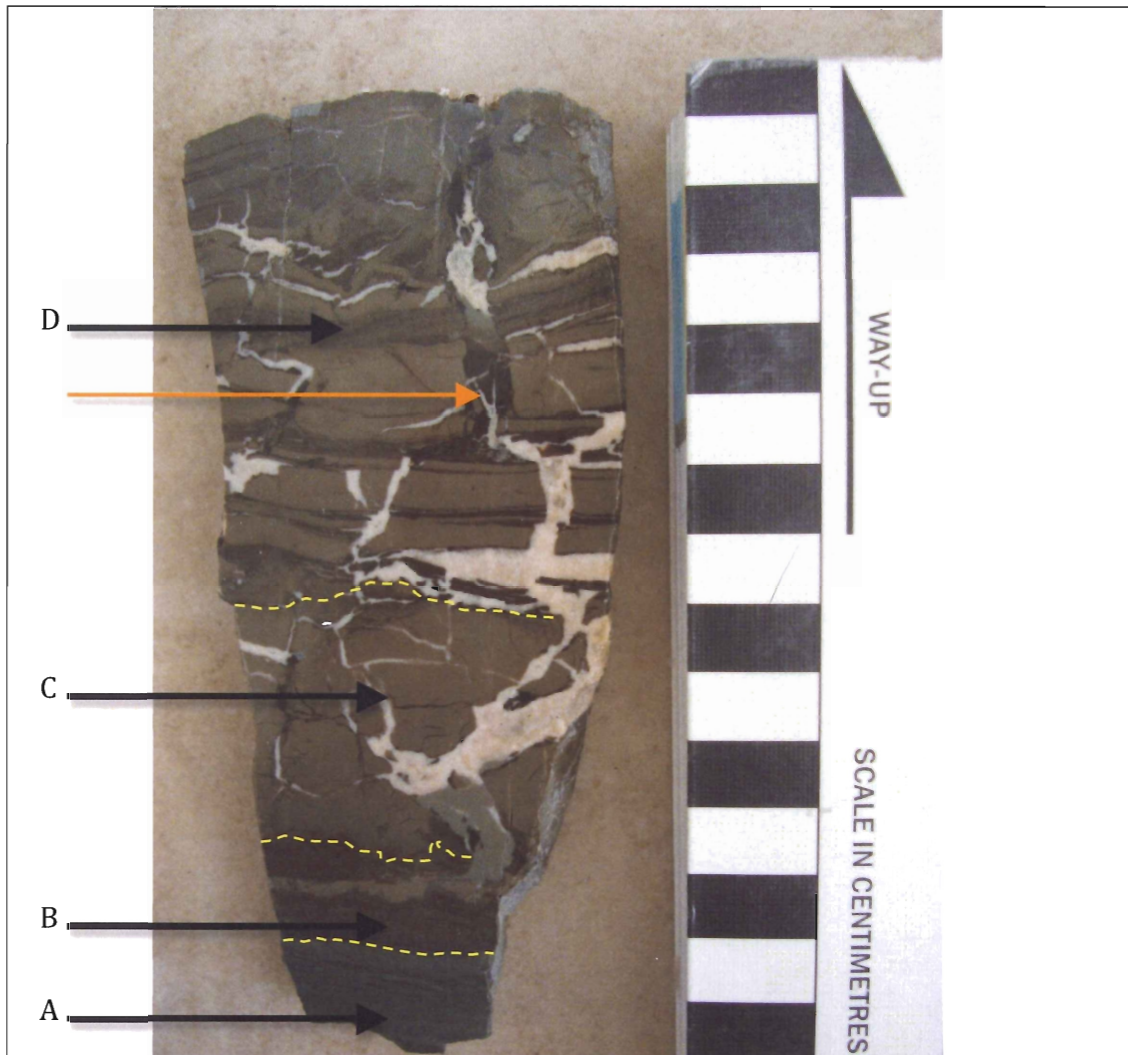


Figure 5.3- Stromatolite sample FG-1.

This slab contains all four facies.

Facies A, B and C are relatively thin in the sample, while facies D is dominant in the upper part. Facies D is distinguished by thick bands of fine-grained massive dolomite and thinner bands of dark grey-black laminae. Possible root system, shown with orange arrow, vertically cuts through existing layers. Veins are predominantly composed of dolomite crystals.

Figures 5.2 and figure 5.3 are samples FG-4 and FG-1 to highlight the major observations of the slab analysis. Four principle microfacies were distinguished along with the intricate root and vein system. The other sampled slab observations are provided in Appendix B.

Facies	A	B	C	D
Classification	Discontinuous Dolosiltite	Continuous Dolosiltite	Dololutite	Banded Dolosiltite/Dololutite
Carbonate/Clastic	Mixed	Mixed	Carbonate	Mixed
Range of Thickness (cm)	1.0 cm-3.0 cm	2.5 cm-5.5 cm	3 cm-5.5 cm	4 cm-8 cm
Colour (Laminae) Hand sample Thin section	Hand sample: Greenish-grey	Hand sample: Light grey Thin section: Dark and light grey	Hand sample: Pale grey Thin section: Dark-brown-grey	Hand sample: Pale grey and dark grey-black Thin section: Dark brown-grey and light grey with dark organics
Average Mineral Grain Size- Measure in thin section(μm)	Quartz-62 μm Micas-50 μm Opaque grains-52 μm Carbonate grains-52 μm Carbonate matrix-10 μm	Quartz->62.5 μm Isolated packages of very coarse grained quartz- 250 μm Micas-50 μm Opaque grains-50-125 μm Carbonate grains-54 μm	Carbonate Grains-~10 μm	Quartz grains->62.5 μm Black grains-50-200 μm Micas- 50 μm
Sedimentary Structures/ Textures	Graded beds Domal laminae Organic rich layers at top of beds	Graded beds Cross-lamination Domal laminites Grain imbrication and alignment	Massive Fine-grained matrix	Mesh-like fabric Distinct bands of alternating fine- grained massive material and dark medium- grained material with 'coated grain' fabric

Table 5.1 Microfacies Observations

Facies	A	B	C	D
Geometry of laminae Range of thickness of individual laminae (mm)	Wavy, Discontinuous, Irregular, Sub-parallel, Minor crenulations. Individual: ~1mm-3mm	Wavy, parallel, Draped, Downlapping, Tops of laminae crenulated. Individual: ~0.5mm	Homogenous Single Bed	Planar, continuous Pale lamination- massive Dark lamination-Wispy Individual- pale laminations-0.5-1.5mm Dark Laminations~3mm
Fossils	Plant Fragments	Plant Fragments	Plant Fragments Roots	Plant Fragments Roots
Other: Boundary between numbered facies, Veins, Faulting	1-> 2 Sharp	2->3 Gradational Microfaults	3->4 Gradational Veins dominate	Veins, Roots-dark lined bits
Interpretation	Greenish grey color evidence of an oxidized environment. Background sediment with minimal microbial activity.	Higher energy zone with planar, continuous laminae, graded bedding and cross-bedding show sorting and energy flow. Dark laminae probably represent microbial mats.	Massive carbonate bed, probably precipitated as result of microbial mat decomposition. Little to no sediment deposition or very low energy conditions, as indicated by minimal siliciclastic content.	Terrestrial influence with roots penetrating layers. Very dark organic rich laminae represent microbial mats.

Table 5.1 Microfacies Observations
continued

5.3.0 Facies Descriptions

Facies A: Discontinuous Dolosiltite

Facies A is the basal unit found in some stromatolite samples but not in all. It has a mixed lithology of clastic and carbonate grains, and the average thickness of the entire facies package is 3 cm. In hand sample, this facies has minor planar laminae and greenish-grey crinkled laminae. The minerals identified in thin section are quartz, variety of muscovite, opaque grains, and carbonate grains that are all within a fine-grained carbonate matrix. The grain size average seen in this sample is about 50-62 μm and the matrix grain size, which is predominantly dolomite is 10 μm or less.

Facies A has distinct sedimentary structures, from graded beds to domal laminae. The layers become darker at the top of each laminae package. The lamina geometry is convoluted, discontinuous to irregular and sub-parallel. There are minor crenulations and the individual laminae are 1 mm-3 mm thick. Minor plant fragments appear as black elongated material within the laminae. The boundary between facies A and facies B is relatively sharp. There were no pictures taken of this facies.

Facies B: Continuous Dolosiltite

Facies B is present in all the domes sampled and is distinguished by its dark planar and continuous laminae with crinkled layers at the top of each sequence (Fig. 5.4). It has a mixed lithology of carbonate and clastic. The average thickness of this package is 2.5 cm- 5.5 cm. In hand sample, this facies is laminated dark grey to grey. In thin section, the dark laminae are made up predominantly of quartz, muscovite,

opaque minerals (pyrite) and dolomite, and appear lighter grey in plane-polarized light. The same minerals present in facies A are present in facies B. Quartz and dolomite are the predominant minerals identified using XRD analysis (see below). There are isolated lenses with quartz grains diameters that exceed 250 μm in size. However on average, the range of grain size is between 54 μm to 62.5 μm with fine grains within the matrix of less than 10 μm . The larger grains of quartz are predominantly coated by a fine-grained matrix, which gives the appearance that the grain is floating.

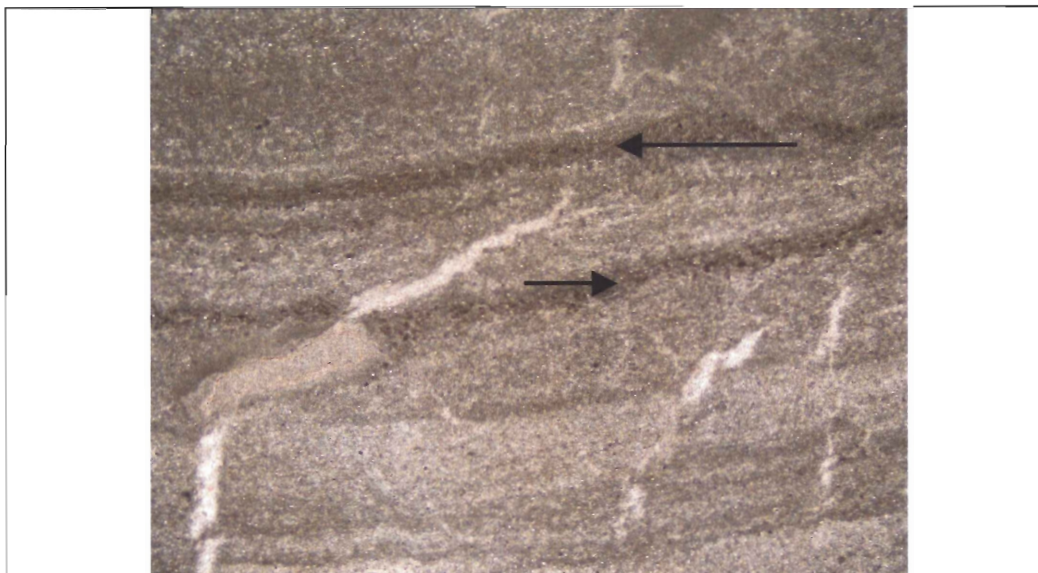
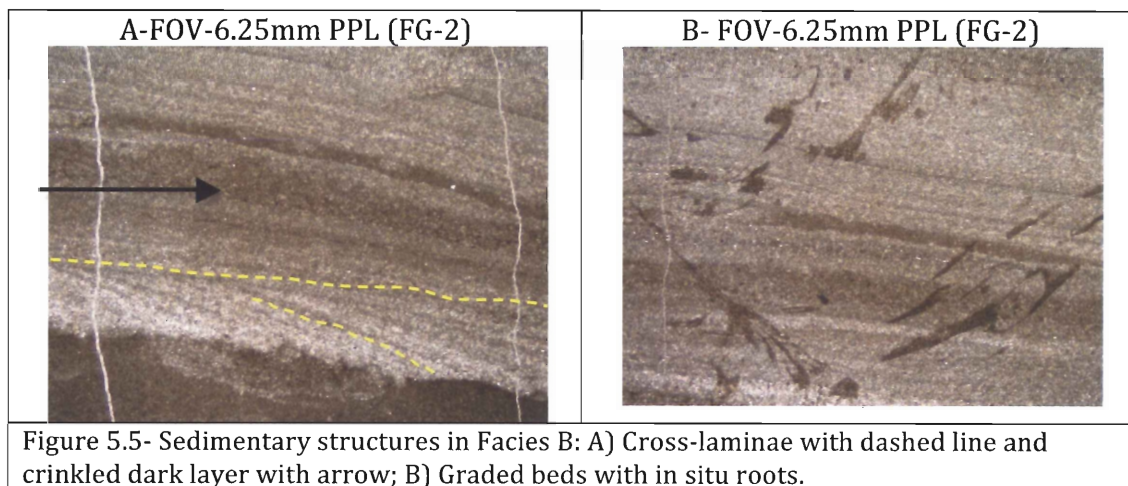


Figure 5.4

FOV: 6.25 mm; PPL

Facies B: Graded beds with dark crinkled layer at the top of each sequence marked by arrows. Detrital grains appear to be floating in these layers.

Facies B has distinct sedimentary structures that include graded beds, cross-laminated beds and domal beds. There are root and plant fragments within this facies (Fig. 5.5). There is evidence for grain imbrication and alignment within the lenses of quartz grains. The geometry of the laminae is wavy, parallel and crenulated in some beds. The graded beds all have crinkled darker layers at the top with what appears to be 'coated sand and silt-size grains', which are grains surrounded by a finer-grained material.



In Figure 5.6, silty sand infills a finer-grained wrinkled surface or possibly rests on a scoured base. There is microfaulting within this sandy package that does not penetrate into the finer grained sediment below and the top of the bed has crinkled, almost mesh-like, laminae in which the quartz grains appear to be floating within a fine-grained material.

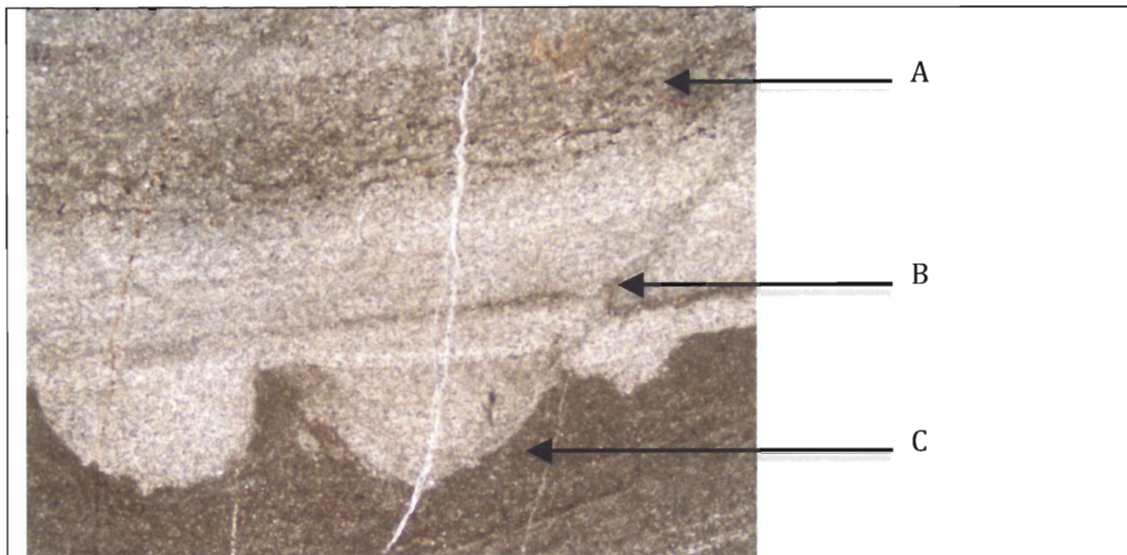


Figure 5.6: FOV-6.25mm PPL (FG-1)
 Fabric elements in Facies B. A) Graded bedding with crinkled laminae (dark) at the top of these beds, B) Non-penetrative microfaulting that seems to be isolated within the sandy layers and C) Erosional layers with scoured bases or possibly infill of fine-grained wrinkled surfaces.

Microfaulting is prominent in facies B. The dark crinkled laminae do not seem to separate cleanly where faulted, and appear to have folded around the faults, suggesting a cohesive texture. In contrast, faulting separates the silty-sandy layers cleanly. The crinkled layer boundary is highlighted in figure 5.7, showing that it does not separate due to faulting and the silty-sandy layers are highlighted in figure 5.8, showing that with faulting these layers have separated. The microfacies boundary between facies B and facies C is gradational.

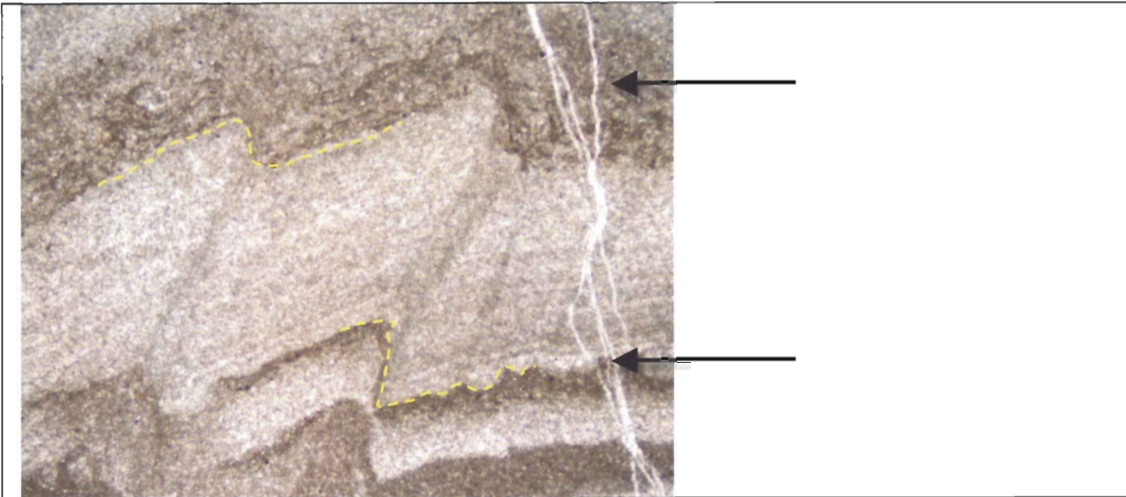


Figure 5.7- FOV-6.25mm PPL (FG-4)

Microfault sets were observed predominantly in facies B. Note the crinkled layer at the top of each sequence represented by arrows does not separate with faulting showing a cohesive texture.

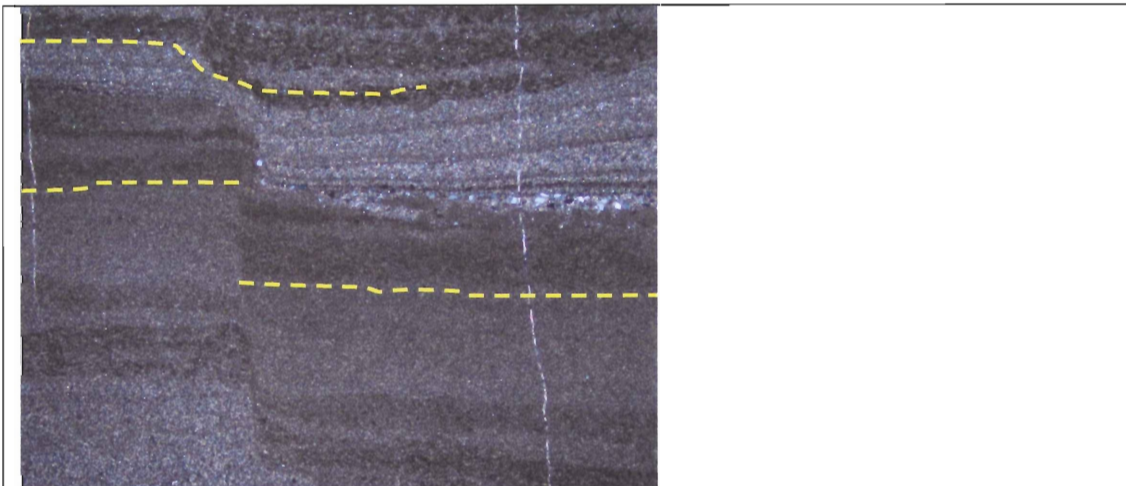


Figure 5.8- FOV- 6.25mm XN (FG-7)

Cohesive texture observed within the crinkled dark laminae and the thicker silty-sand layers do not show cohesion and are separated during faulting.

Facies C: Massive Dololomite

Facies C is almost entirely carbonate in composition and its range in thickness is between 3 cm to 5.5 cm. In hand sample, Facies C is pale grey and in thin section, it is dark brown to dark grey. The average grain size observed under high magnification on the optical microscope is about 10 μm or less making this layer exceptionally fine-grained.

This layer has no sedimentary structures evident. It is predominantly massive fine-grained carbonate and a homogeneous single bed. There are some plant fragments and veins are prominent within this layer. The veins mainly cut vertically (Fig. 5.8), and are dolomitic with large rhomb-shaped crystals. The microfacies boundary between Facies C and D is gradational.

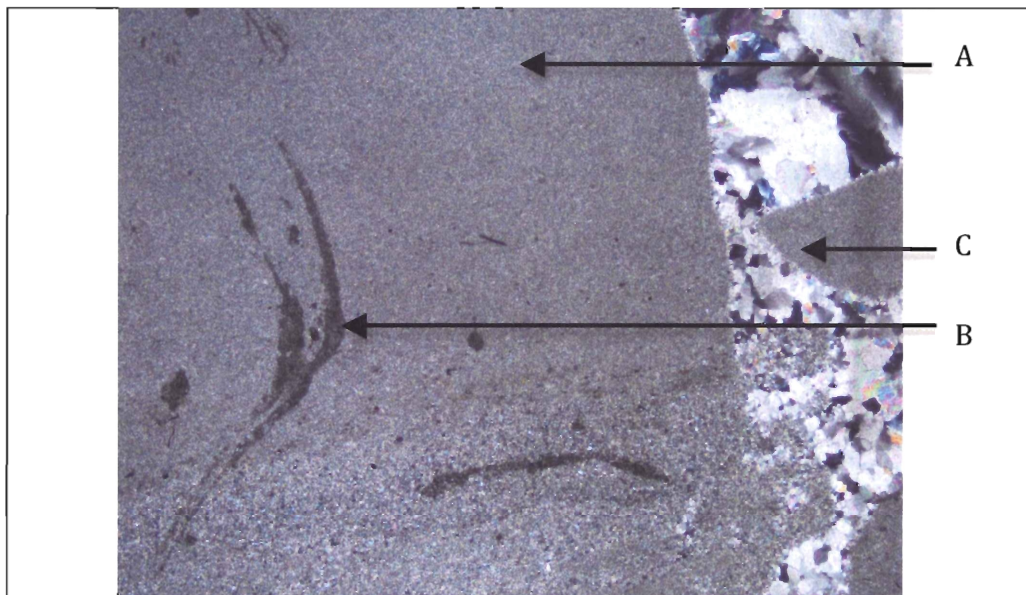


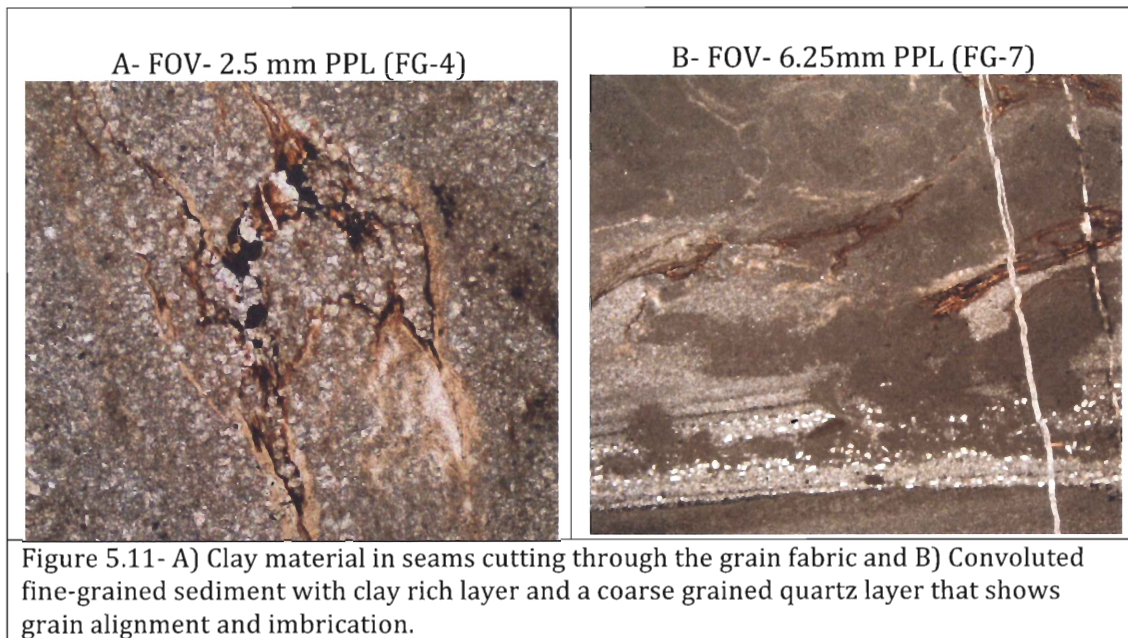
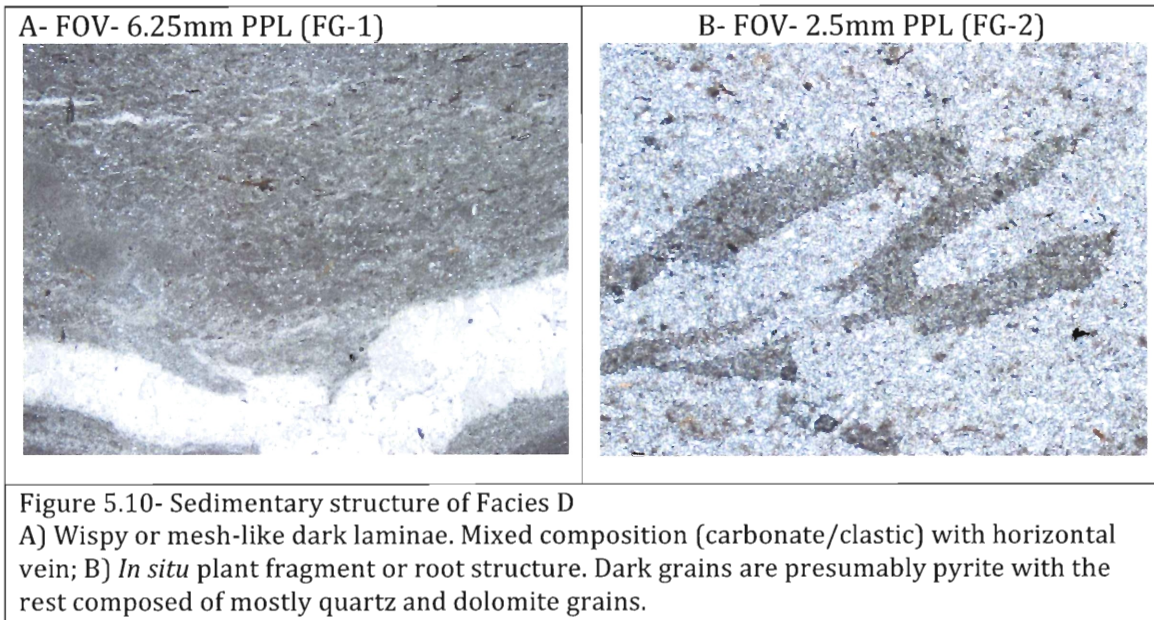
Figure 5.9-FOV- 6.25 mm XN (FG-2)

A) Massive dolomite, with a homogeneous composition. B) Large in situ plant fragments and C) vein cuts down through the layer vertically breaking a piece of the facies C layer.

Facies D: Banded Dolosiltite/Dololite

Facies D contains a mixed composition of carbonate and clastic bands. The range of total thickness of the banded layers is 4 cm-8 cm. In hand sample, the bands alternate from pale grey massive to dark brown-black in colour. In thin section, the pale grey massive layers are fine-grained, similar to Facies C, and the dark brown-black layers are predominantly mixed with fine-grained material wrapping around detrital grains, which gives a wispy appearance. Roots and plant fragments were predominantly seen in this facies.

The minerals identified are the same as Facies A and B: quartz, variety of muscovite, opaque grains (pyrite) and carbonate grains, predominantly dolomite. The sedimentary fabric is different in this section. The dark banded laminae are distinct under thin section for the mesh-like appearance (Fig. 5.9). The geometry of the laminae is continuous but crinkly. The veins are prominent. Some root structures are present and are lined with dark organic debris with iron-rich clay (Fig. 5.10).



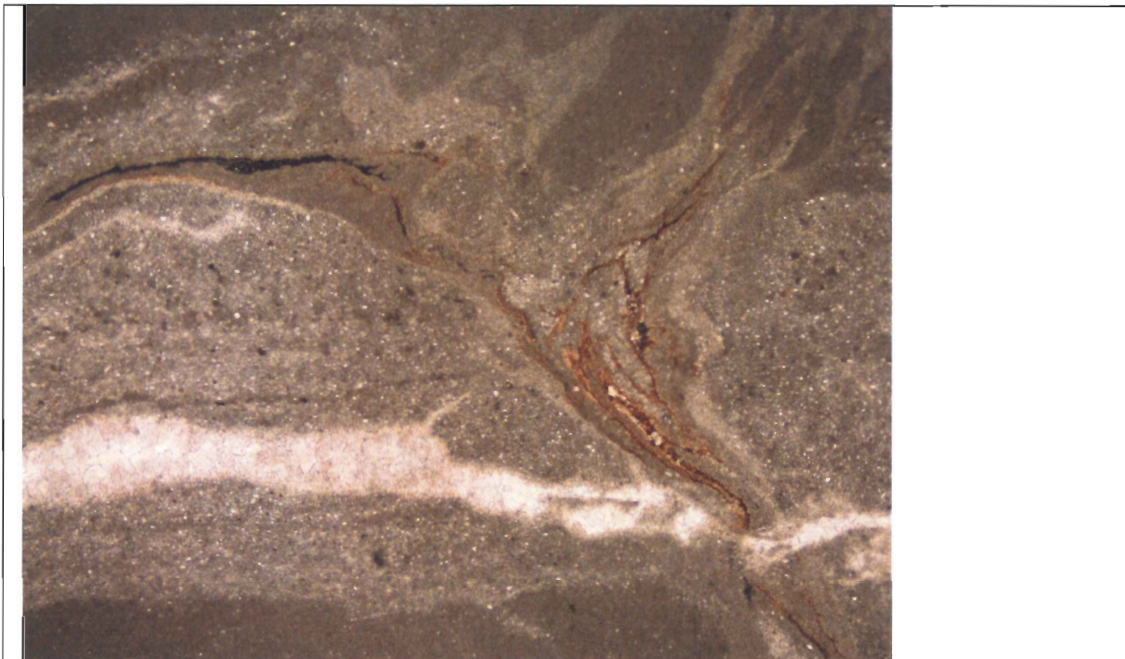
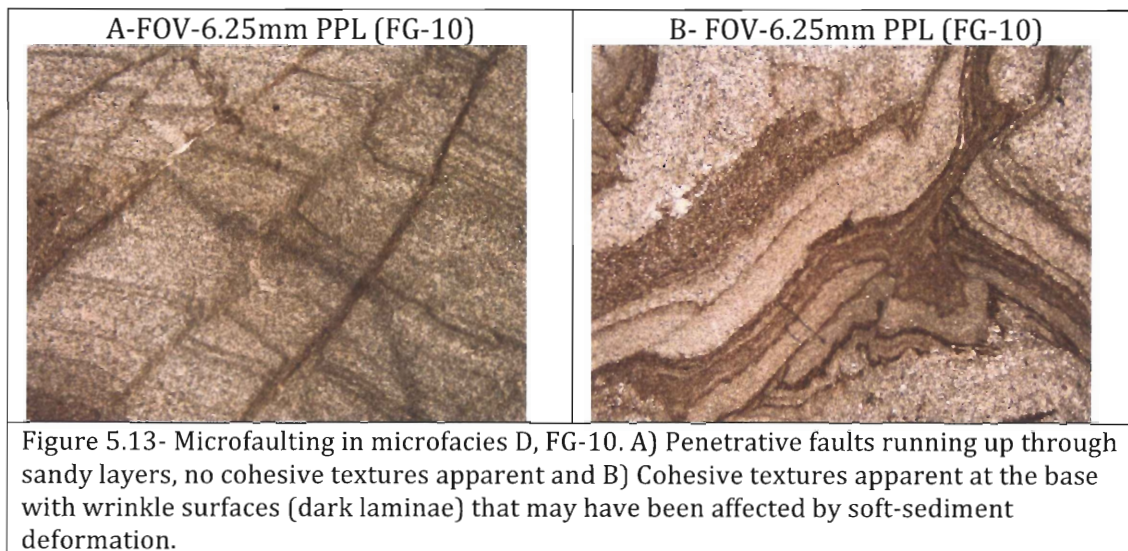


Figure 5.12- FOV- 6.25mm PPL (FG-11) Iron rich clay material that has penetrated down a crack or root within wispy lamination and horizontal vein. The opaque to black grains are presumably pyrite and the lighter grains are quartz with a fine-grained carbonate matrix wrapping around the detrital grains. A dolomitic vein runs horizontally through this band of sediment.

Iron- rich clay material is present, typically in association with root-like structures (Fig. 5.11 and Fig. 5.12). Opaque minerals, provisionally identified as pyrite or ilmenite, are present throughout the wispy bands. Faulting is also evident within this layer, but appears slightly different than the faulting observed in Facies B. The faulting here is more disrupted and may have formed in conjunction with soft-sediment deformation (Fig. 5.13).



In sample FG-10, the laminae display sharp curves within the banded dolosiltite/dololutite facies (Fig. 5.14). The top of the bedding contains the crinkled layer with 'coated grain fabric' present. The sediment above is disturbed but the graded beds that are curved have not been disrupted from deformation showing stabilization.



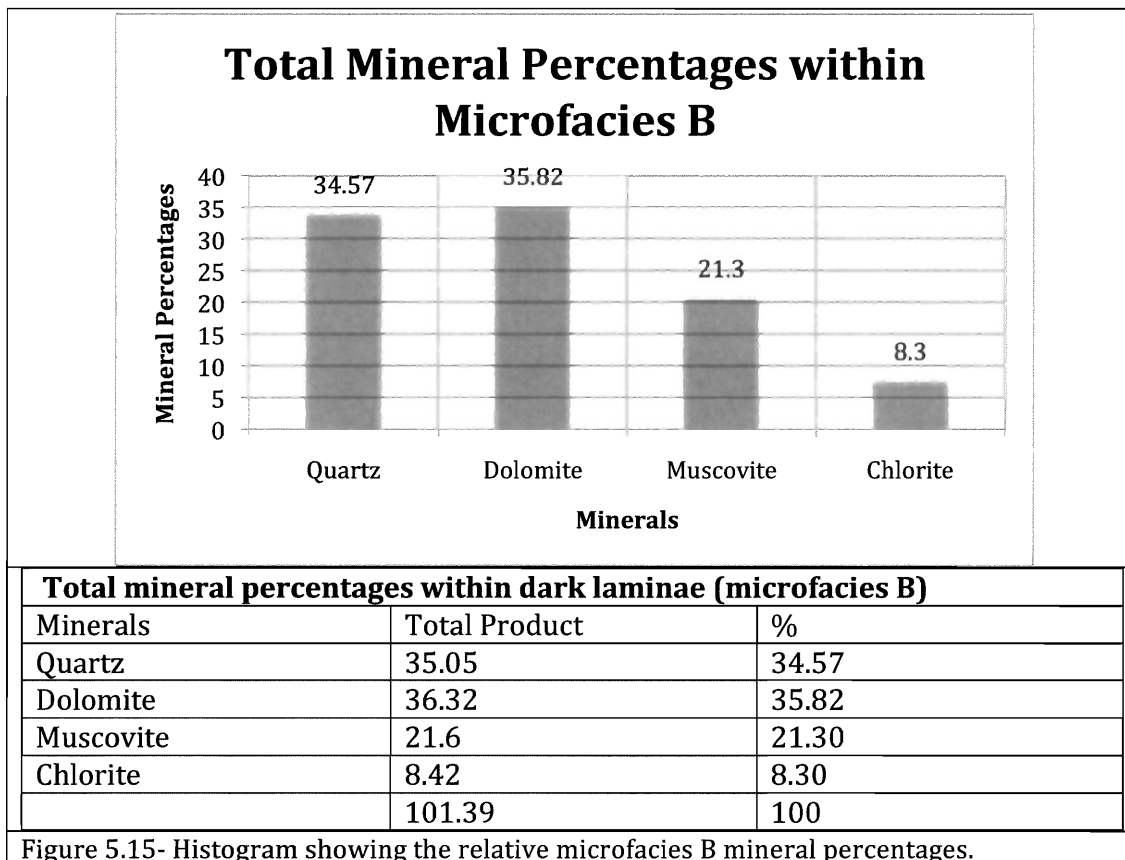
5.4.0 Mineralogy Results

X-ray diffraction analysis was completed on four of the twelve available samples: FG-1, FG-7, FG-8 and FG-10. There were three areas of interest: microfacies B, microfacies C, and the veining. Fragments of these three materials were cut and crushed for analysis. The samples were labeled based on the key identifying features. Facies B was the dark laminated layers within the stromatolite domes. In the XRD analysis the dark laminae were abbreviated to the letter d. Facies C, was the largely massive layer that was pale in hand sample and was therefore labeled with the letter p. The veining was labeled v. See XRD data and quantitative results in Appendix C.

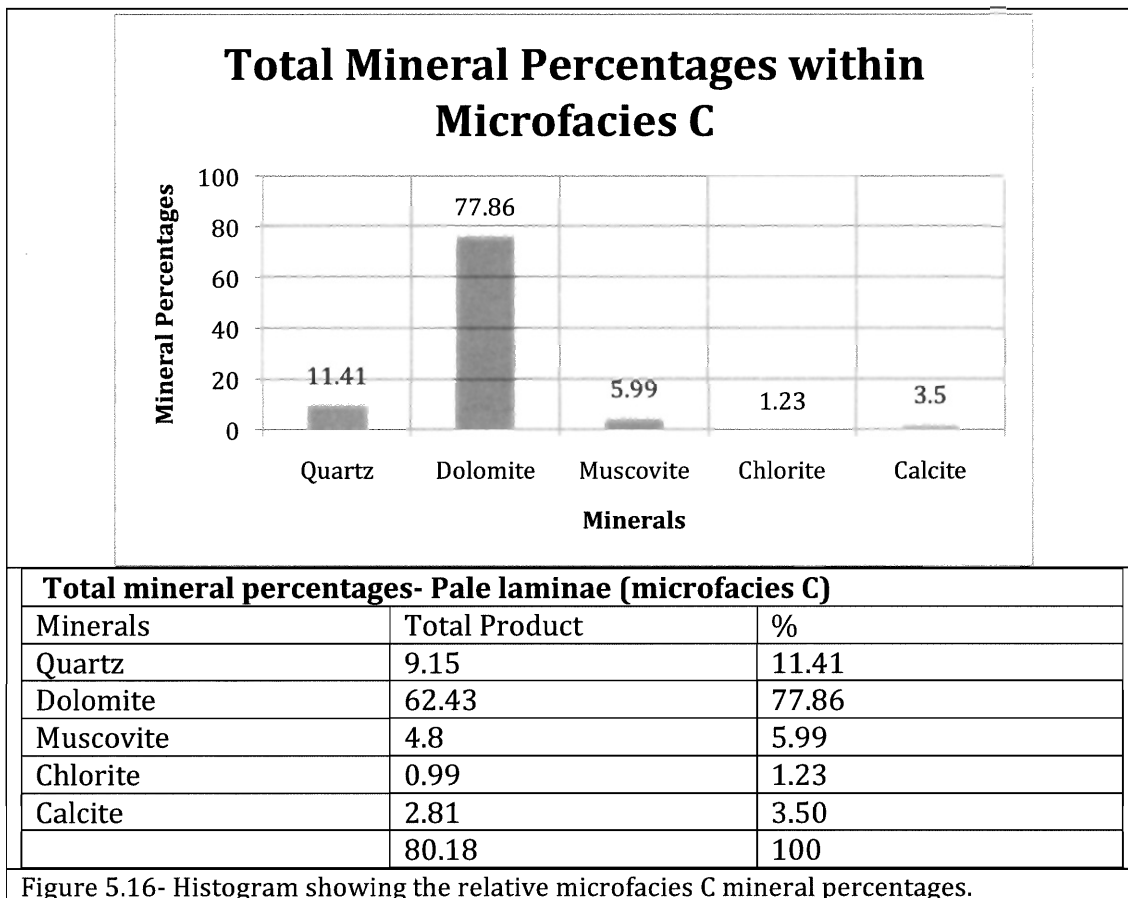
After the computer analysis was complete, and the key peaks were plotted on the XRD graphs, semi-quantitative mineral percentages were calculated using the specific mineral intensity factors and measuring the diagnostic peaks from the XRD data.

The five major minerals that were identified through the XRD analysis were Dolomite ($\text{CaMg}(\text{CO}_3)_2$), Quartz (SiO_2), Muscovite ($\text{KAl}_2\text{AlSi}_3\text{O}_{10}(\text{OH})_2$) or the clay mineral Illite, Calcite (CaCO_3) and Chlorite ($(\text{Mg,Fe,Al})_6(\text{Si,Al})_4\text{O}_{10}(\text{OH})_8$). The mineral percentages for these minerals were completed using the semi-quantitative approach. Figures 5.15, 5.16 and 5.17 are the different areas of interest and their mineral percentages in graphical form.

The main minerals present in microfacies B are quartz, dolomite, muscovite and chlorite (Fig. 5.15). Dolomite and quartz have approximately the same percentage of about 35%, while muscovite and chlorite are lower. Microfacies B was distinguished by its planar laminae and graded bedding with the dark crinkled layers at the top of each sequence. According to Figure 5.15, siliciclastic minerals are predominant but there is a high percentage of a carbonate mineral, which means that the conditions during deposition had to support both types of deposit or early diagenesis resulted in the precipitation and lithification of carbonate minerals.



The predominant mineral in microfacies C is dolomite with a mineral percentage of approximately 80% and a small fraction of quartz at around 10%. The other minerals that make up the remaining 10% are muscovite, chlorite and calcite (Fig. 5.16). Microfacies C was determined to be a single homogeneous layer that contained very-fine carbonate grains that were under 10 μm and this layer was directly under thick, dark laminated layers within microfacies D. Microfacies C also contains many of the veins, which are composed of mostly dolomite crystals.



Finally, as already stated, the veins consist mostly of dolomite, with minor calcite and a small amount of quartz (Fig. 5.17). The dolomite forms approximately 78% of the sample suite, calcite 20% and quartz 2%. In some cases, these veins appear to have formed where original root systems existed.

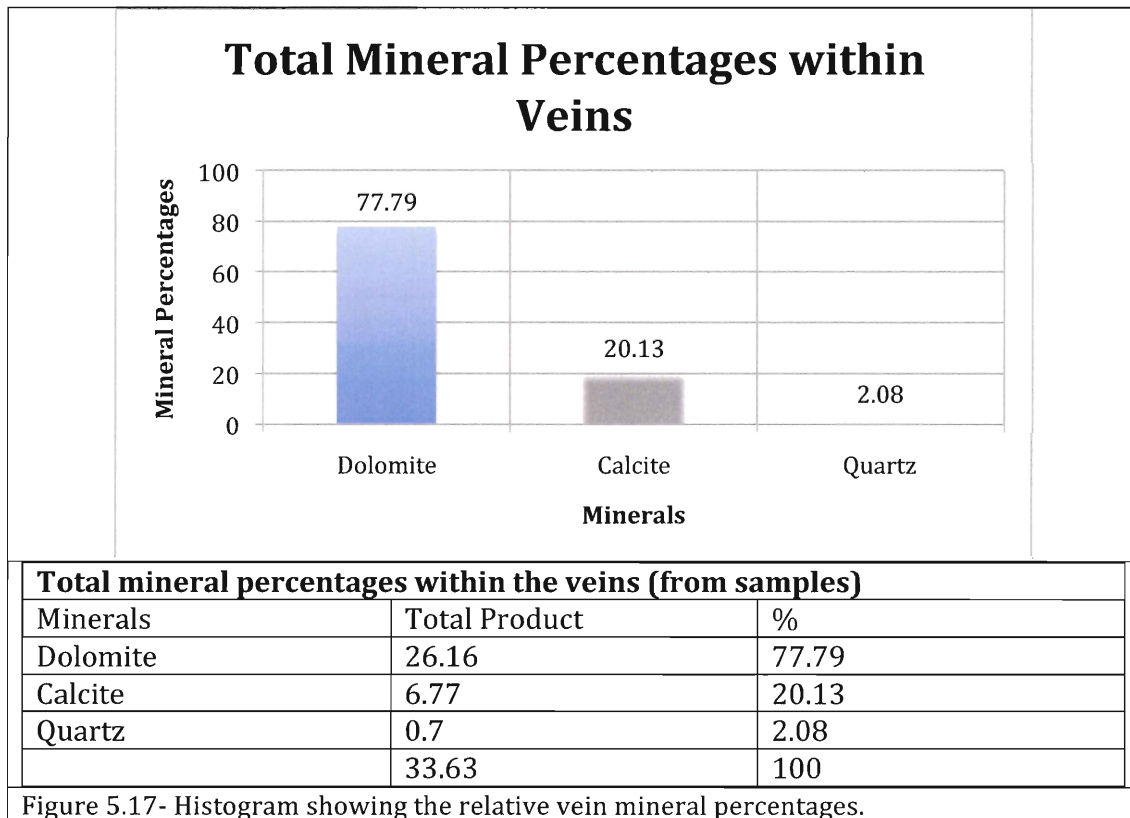


Figure 5.17- Histogram showing the relative vein mineral percentages.

5.5.0 Microfacies Interpretations

The principal reason for petrological analysis was to take an in-depth look at the internal structures of the domal stromatolites on the rock platform and distinguish the different microfacies. Thin sections were used to obtain a detailed view of the sedimentary structures and relict microbial structures. The XRD analysis was carried out to obtain a better understanding of the mineralogy of these stromatolites and draw conclusions to why carbonate was present in a largely siliciclastic setting, which is discussed in further detail in Chapter 6.

Based on the slab analysis, the platform stromatolites were split up into different microfacies, which were comparatively linked back to the cliff-section stromatolites. Although no microscopic analysis was performed on samples from the cliff section, the stromatolites in the cliff face and on the rock platform have similar upward trends of microfacies from A to D (Fig. 5.18). Microfacies A, which is convoluted and green-grey colour can be linked to the greenish-grey mudstone layer seen in the cliff face, which was interpreted earlier as a coastal marsh deposit and is located just below the horizontal base of the stromatolites in the cliff section. Microfacies B contains planar lamination and cross-laminae, and matches well with the lower portion of laminae observed in the cliff section, also part of the shallow water setting. Microfacies C and D, both of which contain considerable amounts of pale fine-grained dolomite, could be combined as one major microfacies, but microfacies C is predominant in most of the rock samples, so this division is kept. The thicker lamina at the top of the stromatolite within the cliff section probably represents microfacies C and D within the platform stromatolites. These two

microfacies were heavily veined and consist of distinct bands of pale massive dolomite, and dark bands, which were possibly thick microbial mat layers.

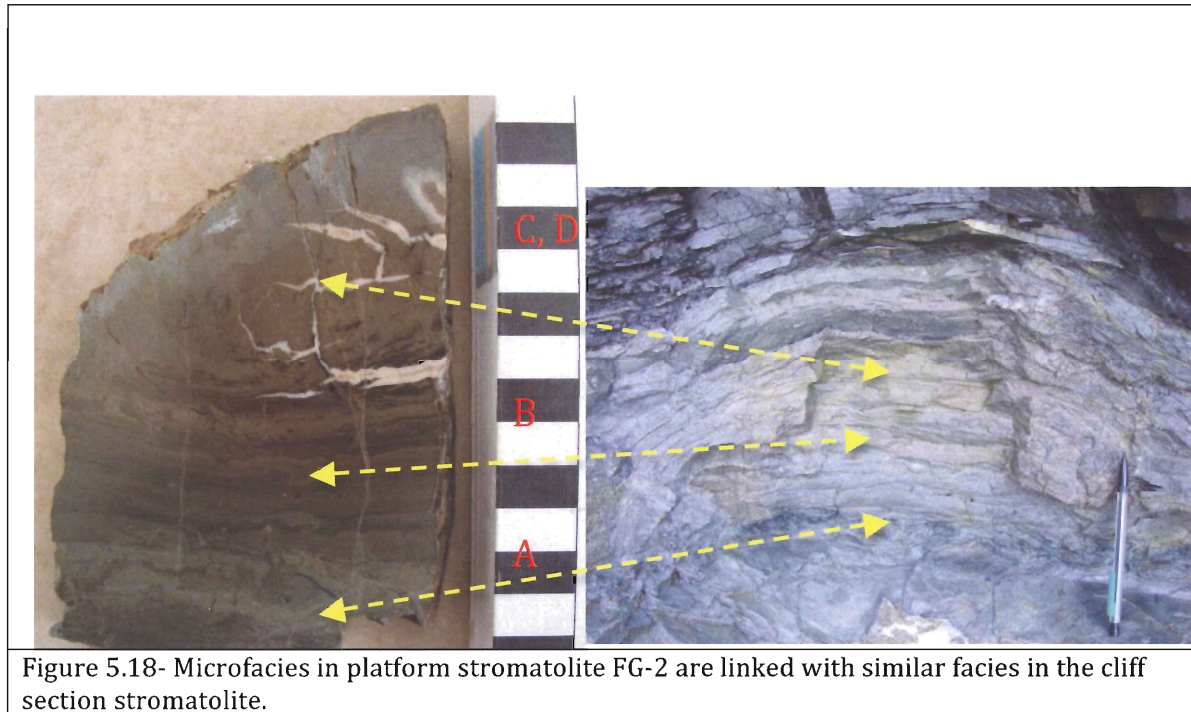


Figure 5.18- Microfacies in platform stromatolite FG-2 are linked with similar facies in the cliff section stromatolite.

In the thin section analysis, the darker laminae are predominantly present in microfacies B and D. These layers are relatively more enriched in pyrite or possibly ilmenite. Pyrite may reflect the metabolic activity of sulphate-reducing bacteria beneath the photosynthetic surface layer of a mat (Schieber, 1989). The cohesive texture of the dark laminae seen within the faulted layers is a good indication that these layers were microbial, and deformation around the non-penetrative faults suggests that the microbial mats were gluing the sediment together and making it stronger.

The 'coated grain fabric' with aligned detrital grains may be remnants of mat-like structures. According to Draganitis and Noffke (2004), if mat-internal carbonate precipitation is voluminous enough, detrital grains of quartz and mica may be encased in a carbonate matrix and form 'floating grains' upon lithification. In ancient examples, a coated grain fabric denotes sand- and silt-sized grains that are surrounded by a fine-grained material. Coated grains have been related to the presence of intergranular coccoidal bacteria and their mucilages.

XRD results show that dolomite is the predominant carbonate mineral and quartz the predominant clastic mineral present in all the samples. Microfacies B, C and the veins were tested. Microfacies B has a large amount of clastic grains that are encased in the fine-grained dolomitic matrix. This matrix is presumably related to earlier microbial mats that had bound and glued the detrital grains into a mesh-like layer.

With regard to microfacies C, according to Kennard and James (1986), massive carbonate cement can form under formative microbial communities due to oxidation and bacterial decay. It is likely that microfacies C and microfacies D, with thick layers of pale, fine-grained carbonate, were formed directly underneath the thicker banded dark laminae of microfacies D, which are interpreted as thick microbial mats. The rooting system that may have existed shortly after the stromatolites were formed disrupted the internal layers of microfacies C and D. The early stages of diagenesis of the organic material may have promoted precipitation of dolomite and minor calcite.

Generally in siliciclastic environments, high sediment mobility and frequent disturbance by waves may prevent the growth of microbial communities. However, periods of low or zero sedimentation could be critical if microbial communities are to flourish (Druschke et al., 2009). Features within the different microfacies record interactions between hydraulic action and microbial colonization. The microbial mats in the Blue Beach Member may have colonized the muddy surfaces of the coastal marsh initially during periods of relatively low-energy conditions and oxygenated surfaces.

The presence of cross-bedding in microfacies B indicates high-energy conditions in general, but reduction in grain-size, sorting and the presence of detrital clay in darker laminae of the stromatolites suggest that periods of relatively low-energy conditions favoured microbial mat growth. With the onset of the silty and sandy layers of microfacies B, the microbial mats were relatively thin but present at the top of each laminae set, identified in thin section by their distinct wispy to crinkly layers. Microfacies C and D are composed of predominantly fine-grained carbonate with thick black layers made up of floating quartz grains, micas, and opaque minerals, presumably pyrite. These dark bands are assumed to be thicker mats.

In summary, it is inferred that these microscopic features are indicative of what microbial structures would accomplish on a sandy substrate. The darker crinkled laminae, dolomitic material, pyrite and floating detrital quartz grains provide evidence that microbial mats contributed strongly to the formation of stromatolite domes in the shallow marine setting of the Blue Beach Member.

Chapter 6.0- Discussion of Blue Beach microbial structures

6.1.0 Paleoenvironment of microbial features and modern analogue

Although it is not the purpose of the thesis to reconstruct the paleogeography of the Horton Bluff Formation (HBF), a brief discussion follows pertaining to the major phases of deposition.

Tibert (1996) subdivided the HBF into three main phases during deposition (Fig 6.1). The underlying strata of the Curry Brook Member represents the initial phase of ponding on the alluvial plain in response to tectonic subsidence, basal compaction, and a rise in a relative base level. Fluvio/lacustrine deposition predominated while fish lived in the fresh water shallow ponds (phase 1).

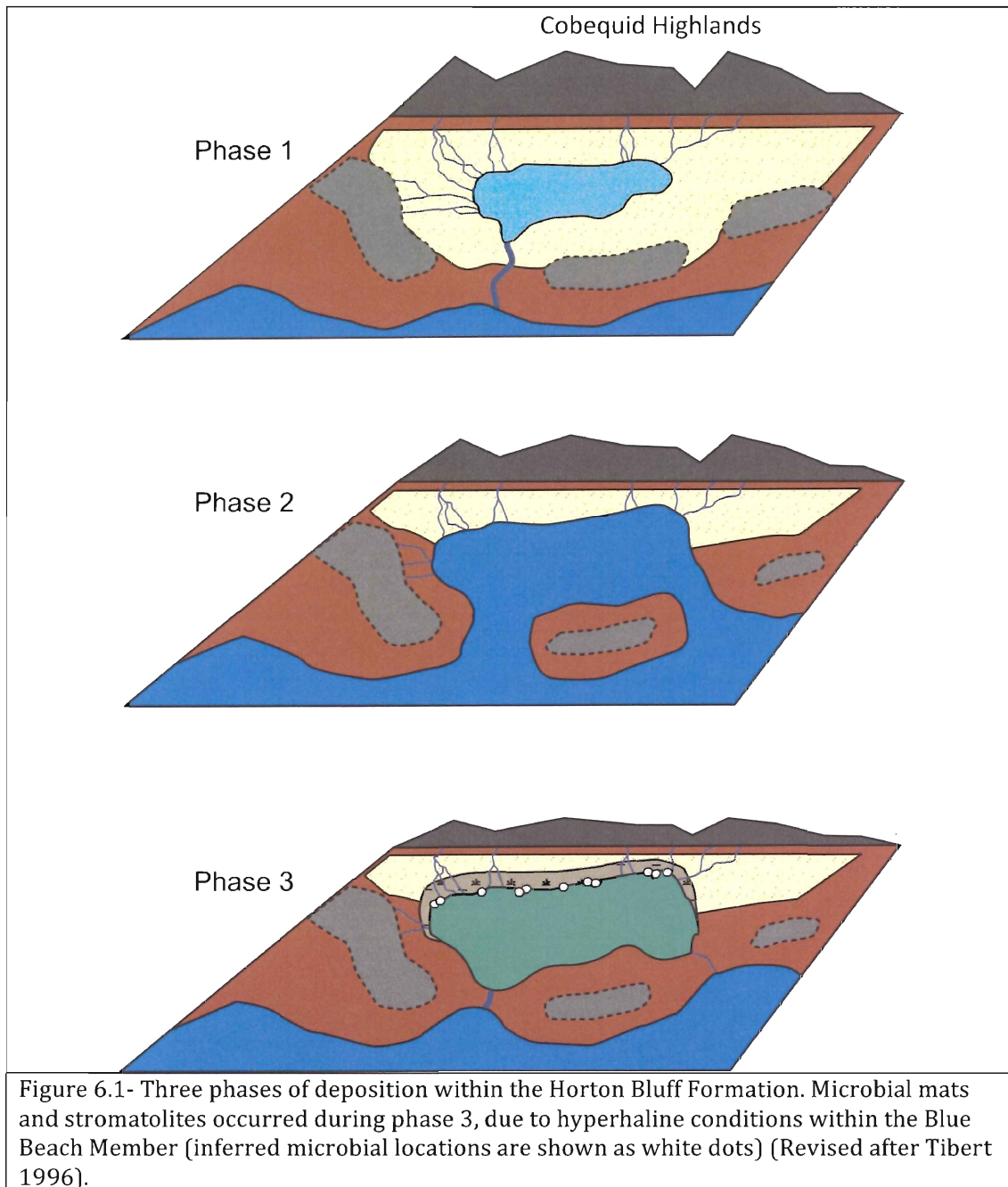
The Blue Beach Member represents the phase during which sea level continued to rise, causing the coastal ponds to be flooded, introducing a largely marine ostracode population (phase 2). The deeper areas of the basin contained a relatively diverse brackish/marine population. At the peak of marine transgression, glaucony grains formed on the sandy substrate of the outer lagoon in water depths in excess of 60 m. The more nearshore areas during the lagoonal phase contained a mixed marine/freshwater component (Tibert, 1996).

Plants were relatively sparse in the saline waters of the littoral zone. Energy levels were moderate as suggested by the hummocky cross-stratification. Shallowing during the second depositional phase was brief. Density-driven silt and sand sheets draped the deeper areas of the basin. Eventually the lagoon became restricted and periodic stagnation of the basin resulted. At this time tabular layers of penecontemporaneous dolomite formed in the shallow subsurface of the muddy

sediments. Pyrite also formed during these periods of dysoxia. At times, when bottom waters became anoxic, the benthic ostracode community was killed. Eventually the free-swimming fish of the upper oxygenated waters were also killed.

Phase three, also part of the BBM, saw the onset of lagoonal termination and infilling. Diversity decreased and shallowing was more frequent as indicated by the green mudstones, mudcracked horizons, and carbonate nodules. Marsh foraminifera, associated with plant-rich mudstone horizons (A5) were common. Ostracodes became less frequent.

Hyperhaline conditions (water with a salinity greater than 40 p.p.t from ocean-based salts) occurred in the uppermost beds of the Blue Beach Member/Hurd Creek transition. The limited amount of fauna suggests elevated salinities because the lagoon became isolated from its marine source and experienced a high degree of evaporation. All the stenohaline and oligohaline genera were wiped out leaving only the true euryhaline opportunists. Finally, the Hurd Creek Member was deposited in a lacustrine/infringing marsh during the end of phase three.



The microbial mats and stromatolites occur in the upper BBM, which has been interpreted as part of phase 3 of the depositional environment. Following the model of Tibert (1996), the microbial community would have flourished in hyperhaline conditions when the lagoon was disconnected from the sea and

evaporitic conditions occurred. The tree stumps are rooted in the green mudstone below the stromatolite bed, where plant detritus is also present. This suggests that a terrestrial marsh was drowned by a rise in sea level, allowing the establishment of a microbial community and the growth of domal forms. As the sea continued to rise, organic-rich black shale was deposited, filling the areas between the algal domes and eventually covering them.

Tibert's model suggests that hyperhaline conditions prevailed at cycle tops as embayments became cut off from the sea, leading to evaporation of isolated water bodies. However, the observation noted above that the domal stromatolites are founded on a paleosol with rooted trees implies a variant on Tibert's model (Fig. 6.2). In this variant, hypersaline embayments formed during the early stages of transgression that led to open-marine conditions and the formation of a new cycle. In a compromise viewpoint, hyperhaline episodes may have taken place in local bays during both the later stages of progradation (cycle tops) and subsequent transgression (cycle bases). However, the presence of roots that penetrate the mounds implies that vegetation became re-established after formation of the mounds, suggesting a more complex alternation of low and high salinity episodes. Tibert's model represents a trend in the long-term evolution of the Horton Bluff Formation, but a similar succession of phases may also have taken place on shorter timescales, within the timeframe of individual cycles or groups of cycles at numerous levels in the formation.

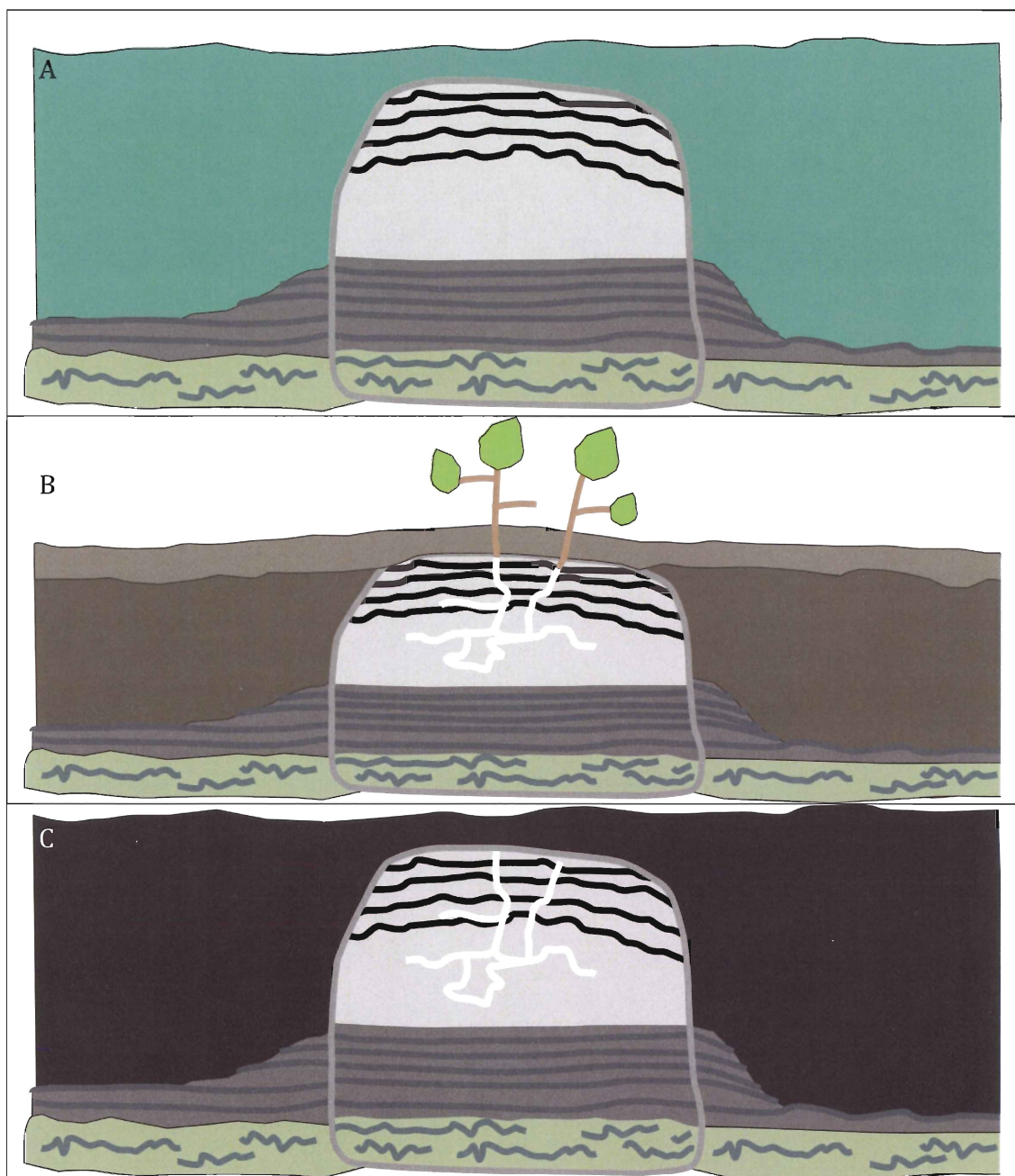


Figure 6.2: Variant to Tibert's long-term model suggests that fluctuations occurred to the paleoenvironment on a shorter time span. A) Hyperhaline conditions would have influenced the onset of microbial communities to flourish. B) Short time span where vegetation became re-established and roots penetrated into stromatolite mounds before they were completely lithified. C) Marine transgression eroded away existing paleosol and only left stromatolites with the rooted structures embedded in the top portions of the mounds. (Gallacher, 2010)

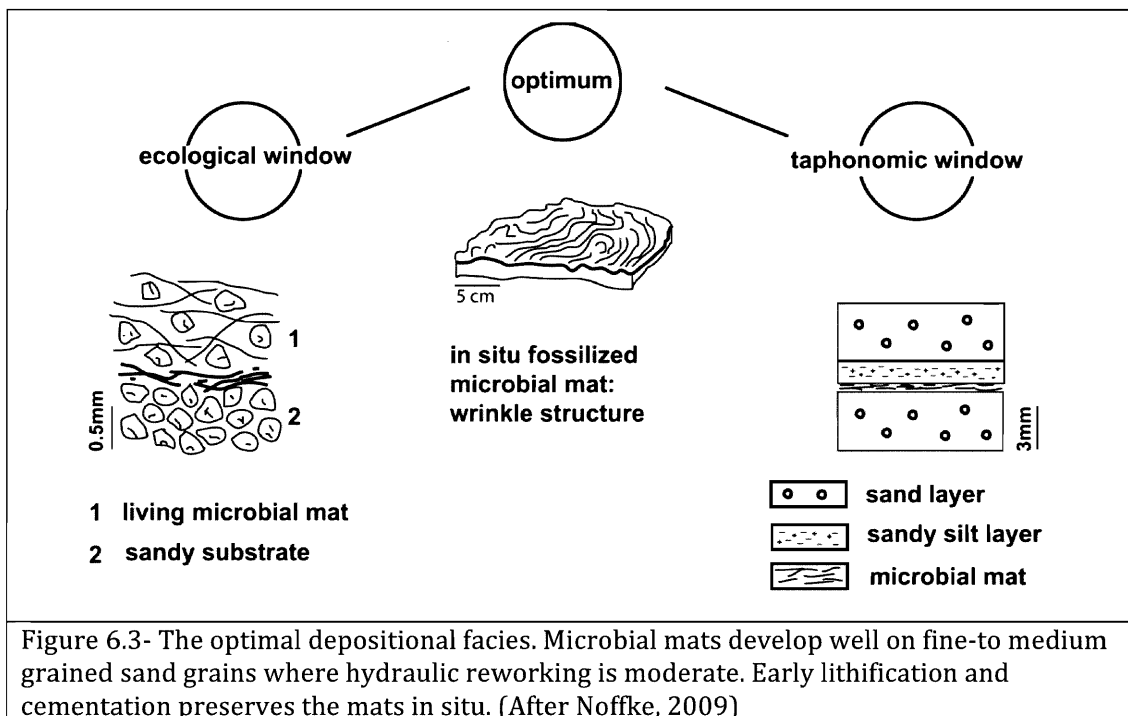
These types of marine embayments are still present today and living stromatolites are seen growing in Hamelin pool, Shark Bay in Australia. Living cyanobacteria are building stromatolites that are over 3,000 years old. Shark Bay has a hot and dry climate, where evaporation exceeds annual precipitation (Hoffman, 1976). The bay is connected to the sea but large areas of sea grass restrict the tidal flow, preventing the tides from mixing the ocean water with the concentrated bay water. The bay becomes highly saline with high salt concentrations (hyperhaline) that are double the salinity of normal seawater. Few predators and competitors can survive in these conditions, allowing the microbes to flourish and form stromatolites, much as they did billions of years ago worldwide and during the Mississippian in Nova Scotia.

6.2.0 Siliciclastic stromatolites in the Blue Beach Member

Both modern and fossil microbial mats preferentially develop on fine sand. Cyanobacteria are relatively large microbes and they are able to move actively through sediment. Fine-grained sediment such as mud has a strong adhesive force that would keep the cyanobacterial cells from roaming easily through the sediment, and typically microbes avoid these deposits. By contrast, if the substrate grains are too large and exceed medium sand diameters, cyanobacteria cannot build up their characteristic microbial fabrics (Noffke, 2009). The optimal facies is clean, translucent, fine-grained to medium-grained quartz sand, which is often predominant in siliciclastic environments. The quartz sand may permit increased light penetration into the sediment allowing filamentous cyanobacteria to grow

below the sediment/water interface as long as hydraulic reworking is moderate (Fig. 6.3) (Noffke et al., 2002).

Microbial mats preferentially develop in moderate hydrodynamic conditions where waves or tides prevent the deposition of mud but lack the energy required to remove bacterially bound sand grains under fair-weather conditions (Noffke et al., 2001). The Blue Beach environment was optimal for microbes when the lagoonal setting became isolated from the sea during phase 3, and this would have reduced the energy of the water column, allowing the time for microbial mat fixation on clean translucent quartz sands. The presence of well-developed mats on bedding surfaces in Cycle 3, along with crinkled surfaces and the floating quartz grains observed in thin sections, is evidence that the microbial structures were within their optimal setting within the siliciclastic environment that dominates the BBM.



Microbes such as cyanobacteria commonly have short generation times, ranging from a few hours to a few days. The high porosity of sandstone is significant during burial because compaction is less therefore early cementation and lithification is essential for preserving domal stromatolites. In siliciclastic environments, stromatolites may experience early lithification only when localized environments induce high carbonate alkalinity through evaporation or by strong mineralization of microbial mats (Druschke et al., 2009).

In phase 3 of the depositional setting of the Blue Beach Member, the lagoon probably became isolated from its marine source and experienced a high amount of evaporation. After the microbial mats began to bind loose detrital clastic grains, high carbonate alkalinity developed through evaporation, producing carbonate laminae and biostabilizing the stromatolites against compaction and erosion.

6.3.0 Carbonate Diagenesis

In modern mats, metabolic processes such as photosynthesis have been observed to shift carbonate solubility enough to cause precipitation of carbonate minerals between and along filaments within the growing mats (Chafetz, 1994). The mineral precipitates can be preserved within the rock record as irregular ooids, disseminated carbonate grains, micritic cement between terrigenous grains, and carbonate cement within laminated sandstones. Another metabolic effect may be the formation of very early diagenetic dolomite from high Mg concentrations in sheaths of living filamentous cyanobacteria (Gebelein and Hoffman, 1973).

Modern lithifying microbial mats produce a range of carbonate precipitates resulting from the interplay of the biological activities of microorganisms and the

environmental conditions. The degree of lithification depends on equilibrium between dissolution and precipitation, which is controlled by the balance among photosynthesis, sulphate reduction, respiration and sulphide oxide (Spadafora et al., 2010). Even when stromatolite accretion is influenced strongly by a large amount of trapped grains, the biologically induced mineral precipitation processes follow similar biochemical paths and indisputably are fundamental to the formation of the microbialitic deposit (Spadafora et al., 2010). Enrichment of iron minerals such as pyrite in dark microbial laminae of the stromatolites suggest that microbial mat mineralization may have facilitated early cementation of sand grains by increasing carbonate alkalinity in pore spaces.

In the XRD results, dolomite was the predominant carbonate mineral observed within all the samples collected. According to Schieber (1999), relics of dolomite matrix within microbial laminae suggest early cementation/lithification of microbial mats. Microfacies B, dolosiltite, had comparable amounts of dolomite and quartz, and in thin sections these graded beds all contained dark crinkled laminae at the top of each sequence, interpreted as relic microbial mat structures. A reasonable inference is that these microbial mats had the metabolic effect of forming very early diagenetic dolomite as a result of high Mg concentrations in the sheaths of living filamentous cyanobacteria.

Microfacies C is predominantly carbonate and is massive with relatively no sedimentary structures. The dolomite may have replaced something else in this layer that is not evident in thin section or XRD analysis. There is the possibility that

the cohesive mats of the banded layer created this new layer of entirely precipitated minerals, but a comprehensive explanation for microfacies C is not yet available.

6.4.0 Microbial influences in the Blue Beach strata

Microbial mats syndepositionally influenced the erosional and depositional dynamics of the ancient sedimentary system of the Blue Beach strata. Firstly, the well-preserved microfacies B shows that biostabilization by the microbial mats successfully protected the surface against erosion. The varied effect of non-penetrative faults on detrital and inferred microbial layers shows the effects of microbial cohesion.

Secondly, the mat laminae entangled mineral particles such as quartz and mica grains that were incorporated and enriched by baffling, trapping and binding. The floating quartz grains within the fine-grained wispy laminae are considered here to be evidence of the baffling, trapping and binding. Biostabilization preserves sedimentary structures from erosion over time. Thirdly, the mass of bacteria within the fine-grained siltstone-sandstone layer and their ability to promote early carbonate precipitation contributed to the total amount of sediment, making it a thicker and stronger bed. Today, the bed shows distinct stromatolite mounds and wrinkled microbial mats that have been well preserved and have not been altered greatly by erosion during Blue Beach Member times.

Chapter 7.0- Conclusions

This section summarizes the main conclusions of this study. The final section provides a closing statement concerning microbial mats and stromatolites within the Blue Beach Member.

7.1.0 Results

7.1.1 Sedimentology

The sedimentary facies comprise cyclic asymmetrical shallowing-up packages that generally decrease in thickness up section. These facies were identified by previous workers, and were confirmed in the present study, as relevant to the occurrence of microbial structures. The facies are defined in ascending order as follows: 1) Black shale is interpreted as deposited below wave base in the profundal zone of a low-oxygen quiescent lagoon or marine arm; 2) Alternating siltstone and sandstone are interpreted as deposited in the shallow littoral zone of the lagoon where energies fluctuated; 3) Green mudstones are pedogenic in origin. Plant detritus and foraminifera indicate proximity to a terrestrial source on the outer fringes of the shallow marine embayment and 4) Dolomite duricrust formed in the subsurface below the shallow water sediment surface, and nodular dolostones formed in the vadose zone of the fluctuating shoreline.

Twelve metres of the upper Blue Beach Member was logged in this project and compared to the stratigraphic log of Tibert (1996). Cycles 14 and 15 of his log are the same cycles that were logged in this thesis.

7.1.2 Microbial Mat and Stromatolites

1. Wrinkle structures, identified as microbial mats, and domal stromatolites were found on and within a fine-grained siltstone-sandstone in the cliff section of the Blue Beach Member. These microbial structures were correlated with the stromatolites observed on the modern rock platform.

2. Key diagnostic features for identifying microbial mats and stromatolites in the field were used to make conclusions that these were accurately identified. Microbial mats were identified based on appearance with their irregular, wrinkled and patchy structures. The stromatolites were identified by the horizontal bases, convex up structure and over-steepened laminae at the margins of the dome, showing an angle of repose greater than normal for subaqueous sediments. These features are indicative of microbial binding.

3. The microbial mats and stromatolites were concluded to have flourished in phase three of the depositional setting within the Blue Beach Member (Tibert, 1996). Phase three conditions may have occurred when the marine waters regressed and slowly isolated a lagoon, allowing the development of hyperhaline conditions. Alternatively, hyperhaline conditions may have developed in the earliest phases of transgression, or during short-term variations in environment and salinity. Only the euryhaline opportunistic species could survive and the stenohaline marine species declined.

4. Translucent quartz sand permitted light penetration into the sediment and allowed filamentous cyanobacteria to grow below the sediment surface. Quiescent periods of low sediment flux in the upper shoreface allowed microbial mats to

escape burial and repeatedly re-establish after storm events. Biostabilization due to established microbial mats prevented further mat removal during erosive episodes, and baffling, trapping and binding of medium-grained to fine-grained sands by filamentous cyanobacteria accelerated accretion of thicker microbial laminae.

7.1.3 Microscopic conclusions

1. Four microfacies were identified within the stromatolite domes:

Microfacies A was identified as disrupted dolosiltite; Microfacies B was identified as continuous dolosiltite; Microfacies C was identified as massive dololite and Microfacies D was identified for its banded dolosiltite/dololite. These microfacies developed in upward succession in numerous individual domes on the modern rock platform, in close comparison with the stromatolite mounds seen in the cliff section.

2. Diagnostic features of microbial mats structures were identified within the thin sections: crinkled and wispy layers at the top of laminae sets, 'floating' detrital grains in mesh-like fine-grained fabric, non-penetrative faulting showing cohesion, dolomitic laminae, and pyrite may all be indicators of microbially induced sediment.

3. XRD conclusions. Based on the results of samples FG-1, FG-7, FG-8 and FG-10 from three sedimentary types, microfacies C, D and the veins, dolomite is the predominant carbonate mineral and quartz the predominant clastic mineral.

Microfacies B shows similar proportions of quartz and dolomite, and the fine intercalation of quartz- and dolomite-rich laminae suggests that early diagenesis associated with the microbial mat filaments elevated Mg component and formed dolomite laminae. Microfacies C with 80% dolomite and minimal clastic material may be a massive carbonate cement that formed under a thick microbial community

due to oxidation and bacterial decay. The veins are dolomitic, and may be related in part to the organic decay of root systems that penetrate the upper part of some domes.

In summary, drawing together megascopic and microscopic conclusions, the paleoenvironment for microbial structures in the Blue Beach Member was a hyperhaline shallow lagoon that was subaerially exposed at times, as evidenced by mudcracks on the siltstone layers. Tree stumps and plant detritus show a terrestrial influence. Cross-bedding and graded bedding with interbedded dolomitic laminae suggest alternate hydraulic activity and microbial growth. Wrinkled surfaces in outcrop and crinkled textures in thin section are good indications that microbial mats developed on or in the accumulating sediment and stabilized it from future erosion. The domal stromatolites are the major indicators in the field that microbial communities thrived in this setting, and over-steepened laminae are indicative of microbial binding. The veins that cut the stromatolite mounds appear in places to have followed root systems that penetrated into the established banded microbial layer, and are presumed to have formed part of a coastal marsh setting that supported terrestrial growth. The organics of the roots later decomposed and veins rich in dolomite crystals were produced.

7.2.0 Recommendations for Further Analysis

In order to fully understand the environment in which these stromatolites and microbial mats flourished, further analysis would need to look at distinct mineral identifications, with geochemical analysis to establish the precise composition of the

mineral phases to provide accurate paleoenvironmental evidence. Further analytical techniques could include (Scholle, 2003):

1) SEM X-ray dispersive analysis- the scanning electron microscope is used to study very small objects and three-dimensional grains. Being equipped with an energy dispersive analyzer, it also can be used for mineral identification and semi-quantitative chemical analysis.

2) Electron microprobe analysis-This analysis provides quantitative geochemical analyses of areas as small as 1 micrometer on a polished sample surface. This type of analysis is valuable for assessing the composition of sample material and giving detailed determination of mineral composition of small crystals for trace element contents.

3) Stable isotopic geochemistry of carbonate rocks involves the measurement of $^{18}\text{O}/^{16}\text{O}$ and $^{13}\text{C}/^{12}\text{C}$ ratios, and comparing these to the ratios in a standard PDB (a belemnite) for carbonate rocks and/or SMOW (standard mean ocean water) for waters and for some carbonate and silicate rocks. Oxygen isotopic analysis may confirm whether precipitation took place under normal marine, hypersaline or fresh water conditions. Carbon isotopic analysis may provide insight into bacterial processes and carbon fractionation.

4) Cathodoluminescence (CL) involves the emission of characteristic visible luminescence by a substance when bombarded by an electron stream or ionized gas beam, and may provide information on the composition, growth and quality of the material.

8.0- References

- Ailsa Allaby and Michael Allaby. "fenestrae." A Dictionary of Earth Sciences. 1999. Retrieved February 27, 2010 from Encyclopedia.com: <http://www.encyclopedia.com/doc/1013-fenestrae.html>
- Chafetz, H.S., 1994. Bacterially induced precipitates of calcium carbonate and lithification in microbial mats. *In*: Krumbein, W.E., Paterson, D.M., Stal, L.J. (Eds.), *Biostabilization of Sediments*. Bibliotheks- und Information system der Carl von Ossietzky Universitat Oldenburg, (BIS)- Verlag, Oldenburg, pp 149-164.
- Cook, H.E., Johnson, P.D., Matti, J.C., and Zemmels, I., 1975, Methods of sample preparation and X-ray diffraction data analysis, in Hayes, D.E.e.a, ed., *Initial Reports of Deep Sea Drilling Project: Washington, X-Ray Mineralogy Laboratory, Deep Sea Drilling Project*, p. 999-1007.
- Draganitis, E. and Noffke, N. 2004. Siliciclastic stromatolites and other microbially induced sedimentary structures in an Early Devonian Barrier- Island Environment (Muth Formation, NW Himalayas). *Journal of Sedimentary Research*; v.74, n.2 p 191-202.
- Druschke, P., Jiang, G., Anderson, T. and Hanson, A. 2009. Stromatolites in the late Ordovician Eureka Quartzite: Implications for microbial growth and preservation in siliciclastic settings. , *Sedimentology*; v.56 p 1275-1291.
- Gebelein, C., Hoffman, P., 1973. Algal origin of dolomite laminations in stromatolitic limestone. *J. Sediment. Petrol.* V. 43 p 603-613.
- Hagadorn, J. and Bottjer, D. 1997. Wrinkle Structures: microbially mediated sedimentary structures common in subtidal siliciclastic settings at the Proterozoic-Phanerozoic transition. *Geology*; v.25, n.11 p 1047-1050.
- Hagadorn, J. and Bottjer, D. 1999. Restriction of a Late Neoproterozoic Biotope: Suspect-Microbial Structures and Trace Fossils at the Vendian-Cambrian Transition. *Palaios*; v.14 p 73-85.
- Hoffman, P.F., 1976. Stromatolite morphogenesis in Shark Bay, western Australia. *In*: Walter, M.R (Ed.), *Stromatolite. Developments in Sedimentology* 20, Elsevier, Amsterdam, pp. 261-271.
- Kennard, J. and James, N. 1986. Thrombolites and Stromatolites: Two Distinct Types of Microbial Structures. *Palaios*. v. 1 p 494-503.
- Mamet, B. 1995. *Hortonella uttingii*, gen. nov., sp. nov., Udoteacees? (Algues vertes?) du Carbonifere inferieur. *Can. J. Earth Sci.* v.32 p 1267-1272.

- Martel, T. 1990. Stratigraphy, Fluvio-lacustrine Sedimentology and Cyclicity of the Late Devonian/Early Carboniferous Horton Bluff Formation, Nova Scotia, Canada. Ph. D thesis. Department of Earth Science, Dalhousie University, Halifax N.S.
- Martel, T. and Gibling, M. 1991. Wave-dominated lacustrine facies and tectonically controlled cyclicity in the Lower Carboniferous Horton Bluff Formation, Nova Scotia, Canada. *Spec. Publications Int. Ass. Sediment.* v.13 p 223-243.
- Martel, T. and Gibling, M. 1996. Stratigraphy and tectonic history of the Upper Devonian to Lower Carboniferous Horton Bluff Formation, Nova Scotia. *Atlantic Geology*; v. 32 p 13-38.
- Nesse, W.D. 2000. Introduction to X-ray crystallography. *In* Introduction to Mineralogy. Edited by Oxford Printing Press, New York, New York, p 160-168.
- Noffke, N. 2000. Extensive microbial mats and their influences on the erosional and depositional dynamics of a siliciclastic cold water environment. (Lower Arenigian, Montagne Noir, France) *Sedimentary Geology*. v. 136 p 207-215.
- Noffke, N., Gerdes, G., Klenke, T., Krumbein, W., 2001. Microbially induced sedimentary structures-a new category within the classification of primary sedimentary structures. *J. Sediment. Res.* A71: 649-656.
- Noffke, N., Knoll, A. and Grotzinger, J. 2002. Sedimentary Controls on the Formation and Preservation of Microbial Mats in Siliciclastic Deposits: A Case study from the Upper Neoproterozoic Nama Group, Namibia. *SEPM (Society of Sedimentary Geology)*; v. 17 p 163-176.
- Noffke, N., Gerdes, G. and Klenke, T. 2003. Benthic cyanobacteria and their influence on the sedimentary dynamics of peritidal depositional systems (siliciclastic, evaporitic salty, evaporitic carbonatic). *Earth Science Reviews*, v. 62 p 163-176.
- Noffke, N., Eriksson, K., Hazen, R., and Simpson, E. 2006. A new window into Early Archean life: Microbial mats in Earth's oldest siliciclastic tidal deposits (3.2 Ga Moodies Group, South Africa). *Geology*. P 253-256.
- Noffke, N., Beukes, N., Bower, R., Hazen, M and Swift, J.P. 2008. An actualistic perspective into Archean worlds – (cyano)bacterially induced sedimentary structures in the siliciclastic Nhlazatse Section, 2.9 Ga Pongola Supergroup, South Africa. *Geobiology*; v. 6 p 5-20.

- Noffke, N. 2009. The criteria for the biogenicity of microbially induced sedimentary structures (MISS) in Archean and younger, sandy deposits. *Earth Science Reviews*. V.96 p 173-180.
- Pflugler, F. 1999. Matground Structures and Redox Facies. *Palaaios*; v.14 p 25-39.
- Schieber, J. 1999. Microbial Mats in Terrigenous Clastics: The Challenge of Identification in the Rock Record. *Palaaios*; v.14 p 3-12.
- Schieber, J., 2004. Microbial mats in the siliciclastic rock record: a summary of the diagnostic features. In: Eriksson, P.G., Altermann, W., Nelson, D.R., Mueller, W.U., Catuneanu, O. (Eds.), *The Precambrian Earth: Tempos and Events. Developments in Precambrian Geology 12*, Elsevier, Amsterdam, p. 663-673.
- Scholle, P. and Ulmer-Scholle, D. 2003. A Color guide to the petrography of Carbonate Rocks: Grains, textures, porosity, diagenesis. The American Association of Petroleum Geologist. Tulsa, Oklahoma, U.S.A.
- Spadafora, A. Perri.E. , Mckenzie,J and Vasconcelos,C. 2010. Microbial biomineralization processes forming modern Ca:Mg carbonate stromatolites. *Sedimentology*. v. 57 p27-40.
- Stow, D. 2006. Carbonate Rocks. *In Sedimentary Rocks in the Field: A Color Guide. Edited by Manson Publishing Ltd. London, UK. p 164-183.*
- Tibert, N. 1996. A Paleoeological interpretation for the ostracodes and agglutinated Foraminifera from the earliest Carboniferous marginal marine Horton Bluff Formation (Blue Beach Member). Nova Scotia. Canada. M.Sc. thesis, Department of Earth Science, Dalhousie University, Halifax N.S.
- Tibert, N. and Scott, D. 1999. Ostracodes and Agglutinated Foraminifera as Indicators of Paleoenvironmental Change in an Early Carboniferous Brackish Bay, Atlantic Canada. *SEPM (Society for Sedimentary Geology)*; v.14 p 246-260.
- Webster, AG. 1919. On the angle of repose of wet sand. *In Proceedings of the National Academy of Sciences of the United States of America*. v. 5 p 263-265.

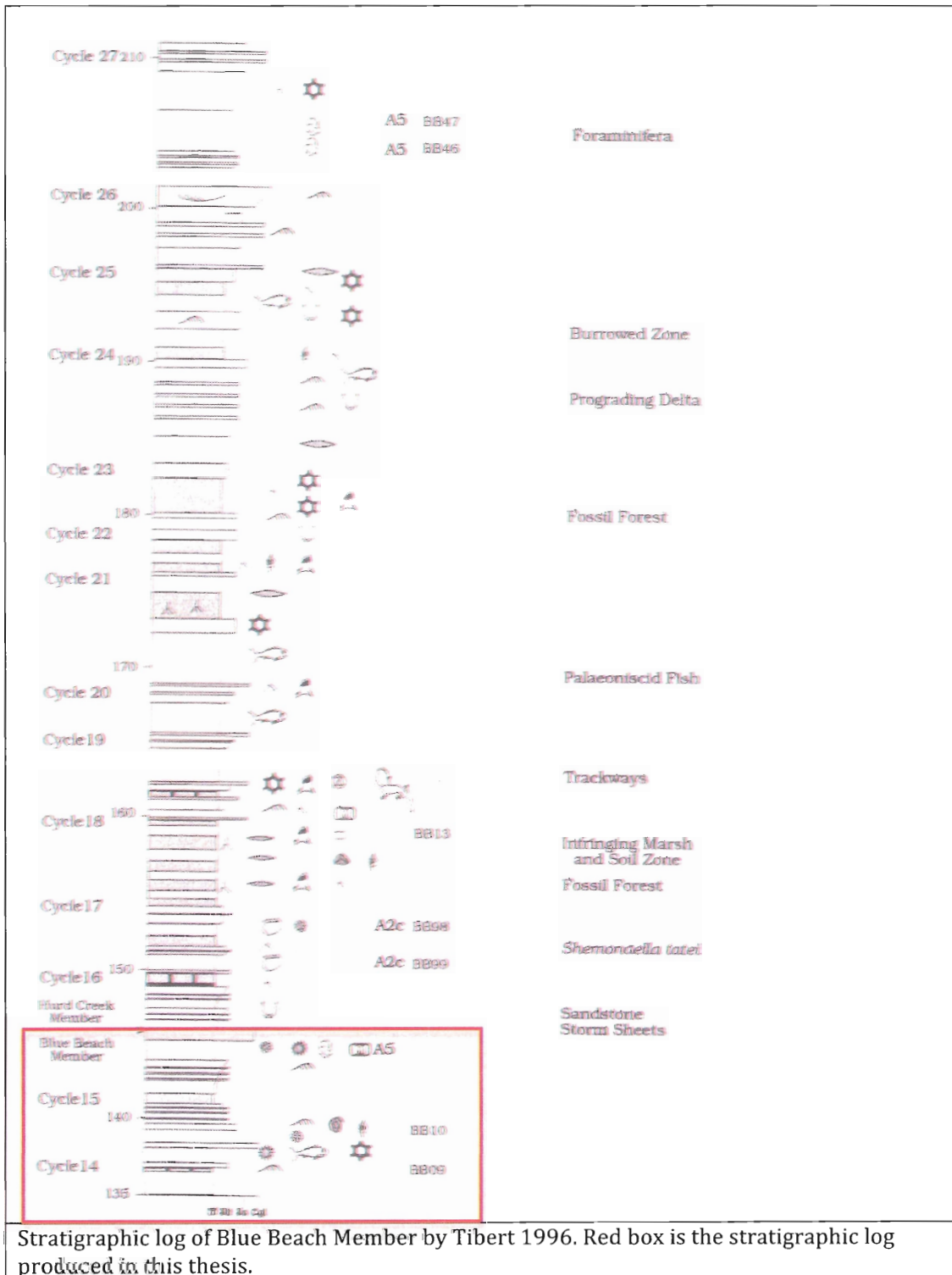
Appendix A- Field Data Paleontology-

Fossil Assemblages	Sedimentary Features	Paleontological Features	Interpretation
Assemblage 1 (A1) Beyrichiacea	carbonate and organic rich shale; framboidal pyrite; glauconized grains; horizontal laminae with minor ripple cross-laminae	<i>Copelandella</i> sp., <i>Shemonaella</i> sp., <i>Carbonita</i> spp., agglutinated foraminifera, abundant paleoniscid fish	below wave base kenoxic profundal sediments; euryhaline marine/brackish
Assemblage 2a (A2a) Paraparchitacea Carbonitacea	siltstone with abundant mica; minor hummocky cross-stratification; ripple cross-laminae; rare pyrite and glauconite pellets	<i>Shemonaella scotoburdigalensis</i> , <i>Carbonita</i> , and sparse <i>Chamishaella</i> sp.; palaeoniscid fish scales, bones and teeth; sparse serpulid worms	shallow littoral zone where moderate wave and current activity keep bottom well-oxygenated; Mesohaline (low salinity) due to fresh/saline water mixing
Assemblage 2b (A2b) Paraparchitacea Koedenellacea	siltstone, fine sandstone, and conglomeratic fish lenses; strongly associated with hummocky cross-stratification; abundant quartz and mica grains	<i>Shemonaella scotoburdigalensis</i> (disarticulated) and <i>Cavellina lovatia</i> (most juvenile articulate carapaces); serpulids and fish debris abundant; macrospores	high energy/ high fluvial recharge; <i>Cavellina</i> (oligohaline) transported into brackish nearshore during storms resulting in a pathological death assemblage; associated with other brackish/ marine species; salinity variable (mixo/oligohaline)
Assemblage 2c (A2c) Paraparchitacea	coarse siltstone and muddy shale; sandstone sheets	<i>Shemonaella tatei</i> and <i>Chamishaella</i> sp.; minor occurrence of stenohaline ostracodes; rare fish and serpulids	high energy shallow nearshore with rapidly changing salinities; low diversity; polyhaline/hyperhaline
Assemblage 3 (A3) Carbonitacea	muddy shale; octahedral pyrite; calcareous micro-concretions and mica	<i>Carbonita</i> sp. abundant; Foraminifera; fish teeth, scales, bones, and coprolites very abundant; serpulids common; plant detritus	shallow muddy wave attenuated shoreline; fluvial recharge high; herbivore ostracodes; some reworked brackish species; oligohaline
Assemblage 4 (A4) Paraparchitacea Koedenellacea Youngiella Bairdia	coarse silty shale; abundant glaucorty grains and possible hard ground	<i>Chamishaella</i> sp., <i>Shemonaella tatei</i> , <i>Geisina</i> sp., <i>Youngiella</i> sp., and <i>Bairdia</i> ; euryhaline and stenohaline marine species; highest diversity of study	stable marine lagoon; low current activity; stenohaline?
Assemblage 5 (A5) agglutinated Foraminifera large Carbonitacea	mudstone, coarse silty interbeds; euhedral pyrite common to abundant; slightly reactive to HCl; micaceous; associated carbonate nodules and desiccation cracks	<i>Trochammia</i> sp., <i>Amnobaeculites</i> sp., and <i>Arivrotium</i> sp.; rare fish debris and coprolites; pyritized foraminiferal tests?; plant detritus common	upper salt marsh associated with vegetation (humic matter); stable shoreline during ponding; reduced fluvial recharge; limnetic/oligohaline

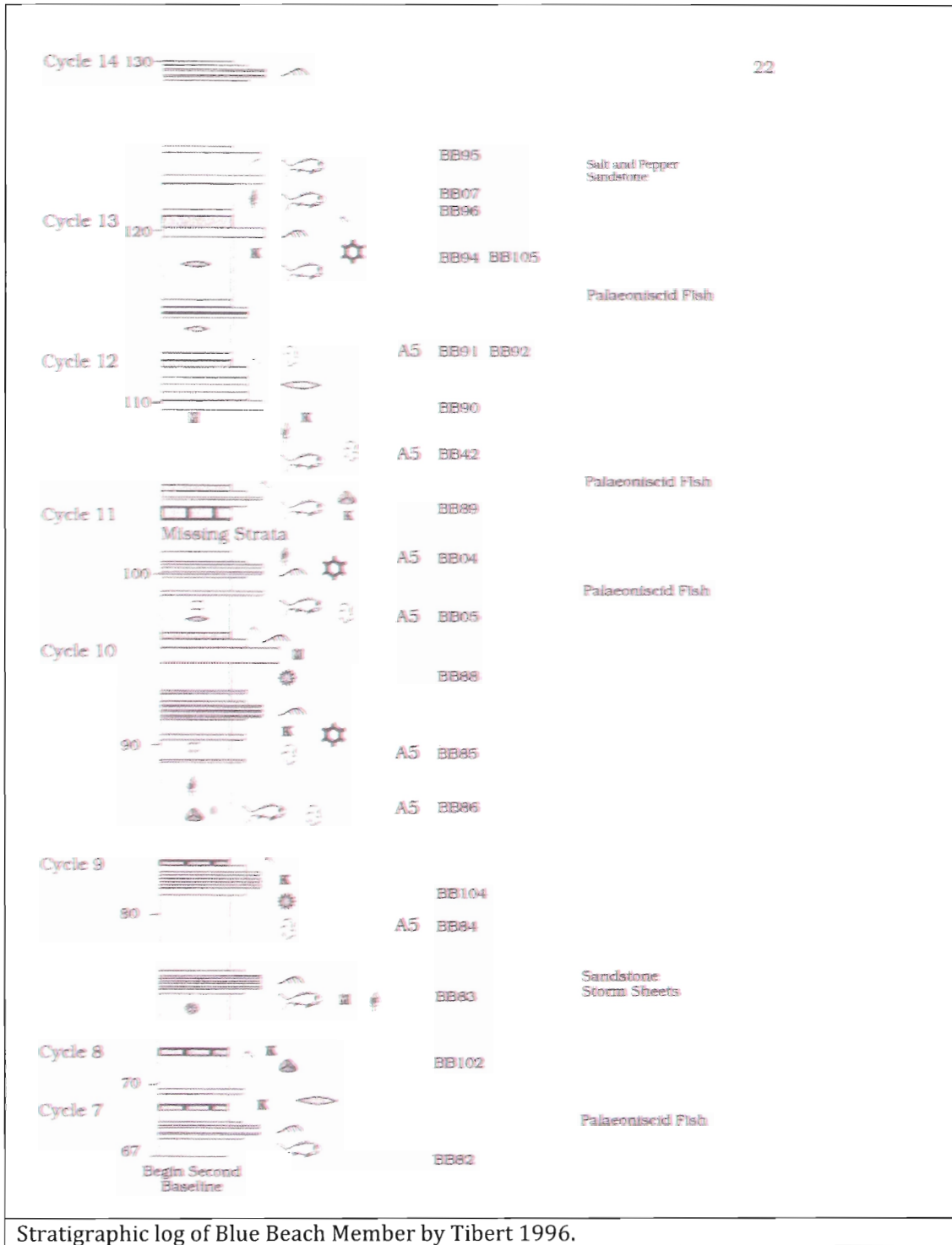
Five Fossil Assemblages present in the BBM along with the interpretations, After Tibert 1996.

	Agglutinated Foraminifera		Insitu Lycopside Trees
	Paraparchitacean Ostracodes		Disarticulated Plant Matter
	<i>Copelandella novascotica</i>		Root Traces (pedoturbation)
	Bairdiacean Ostracodes		Hummocky Strata
	<i>Carbonita sp.</i>		Bioclastic Ggl Scours
	Bivalves		Trough Cross-beds
	Serpulid Worms		Ripple Laminae
	Worm Burrows		Desiccation Cracks
	Palaeoniscid Fish		Pyrite (euhedral and Framboidal)
	Coprolites		Glauconite (euhedral and pelloidal)
	Algal Bodies		Nodular Dolomite
	Megaspores		Micaceous
	Tetrapod Trackways		Slickenside Structures
	Dolomite Horizons		Green Calcareous Mudstone

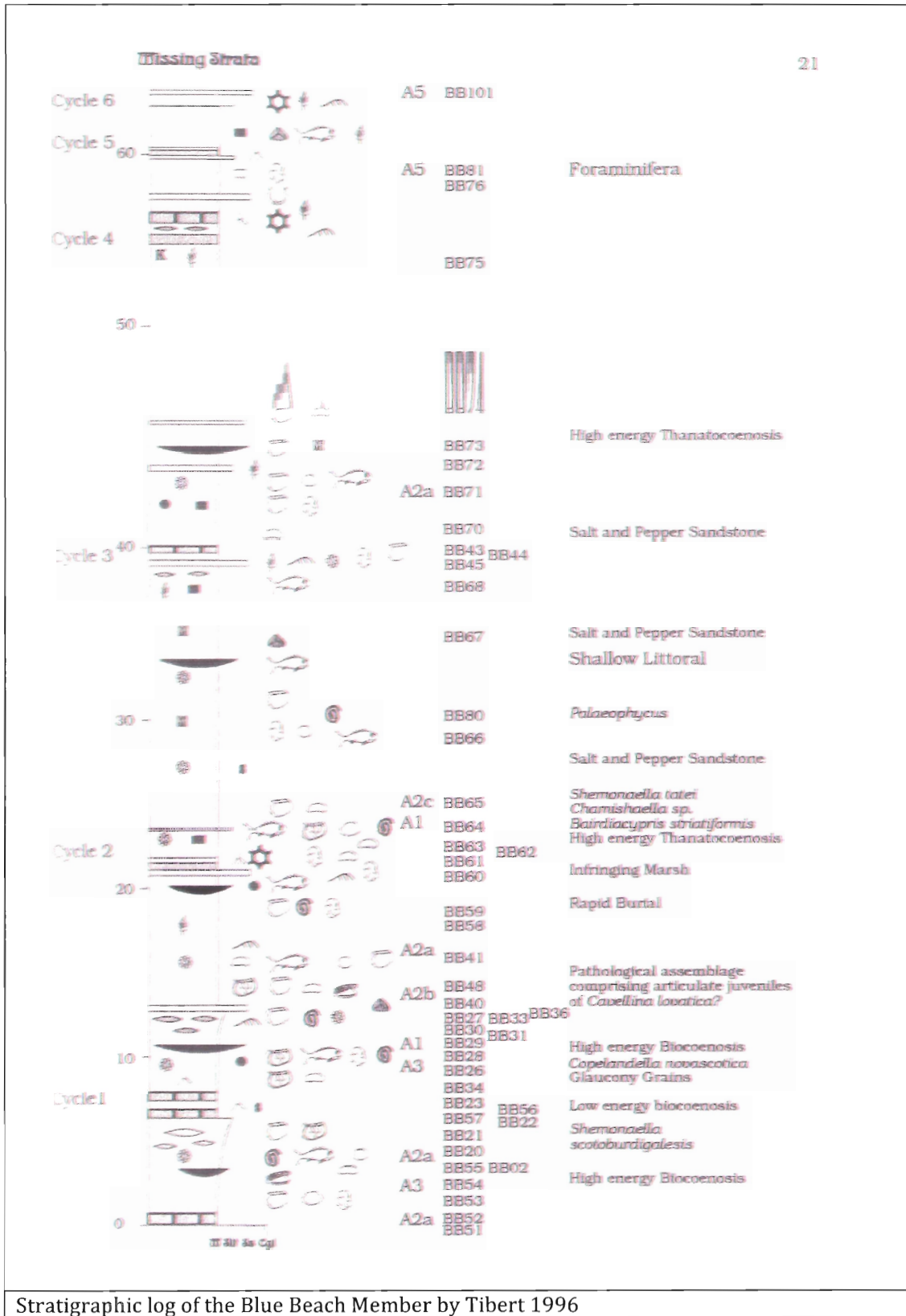
Legend for stratigraphic log. After Tibert 1996.



Stratigraphic log of Blue Beach Member by Tibert 1996. Red box is the stratigraphic log produced in this thesis.



Stratigraphic log of Blue Beach Member by Tibert 1996.



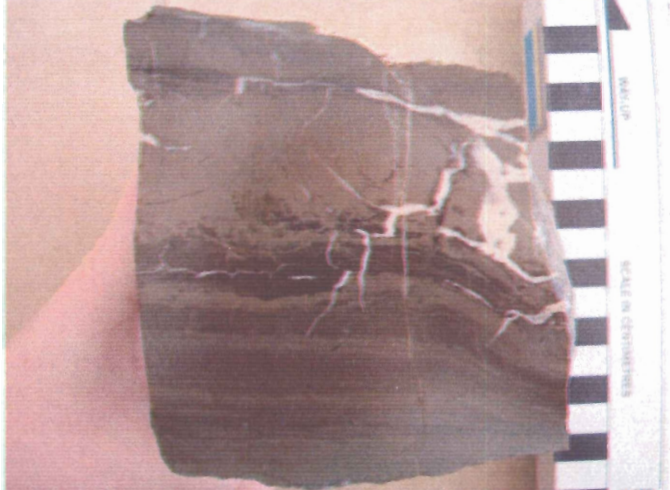
Label	Description	Symbol	Latitude	Longitude
Parking	Parking Lot of Blue Beach	• Dot	N45.09776	W064.21603
S1	Stromatolite mound	• Dot	N45.10551	W064.21861
S10	Stromatolite mound 10	• Dot	N45.10558	W064.21803
S11	Stromatolite mound 11	• Dot	N45.10559	W064.21796
S12	Stromatolite mound 12	• Dot	N45.10556	W064.21792
S13	Stromatolite mound 13	• Dot	N45.10556	W064.21785
S14	Stromatolite mound 14	• Dot	N45.10553	W064.21780
S15	Stromatolite mound 15	• Dot	N45.10546	W064.21773
S16	Stromatolite mound 16	• Dot	N45.10541	W064.21771
S17	Stromatolite mound 17	• Dot	N45.10534	W064.21765
S18	Stromatolite mound 18	• Dot	N45.10530	W064.21764
S2	Stromatolite mound 2	• Dot	N45.10554	W064.21847
S3	Stromatolite mound 3	• Dot	N45.10558	W064.21839
S4	Stromatolite mound 4	• Dot	N45.10556	W064.21834
S5	Stromatolite mound 5	• Dot	N45.10555	W064.21835
S6	Stromatolite mound 6	• Dot	N45.10557	W064.21831
S7	Stromatolite mound 7	• Dot	N45.10556	W064.21822
S8	Stromatolite mound 8	• Dot	N45.10556	W064.21819
S9	Stromatolite mound 9	• Dot	N45.10555	W064.21815
Study Area Cliff	Blue Beach Member	• Dot	N45.10543	W064.21920

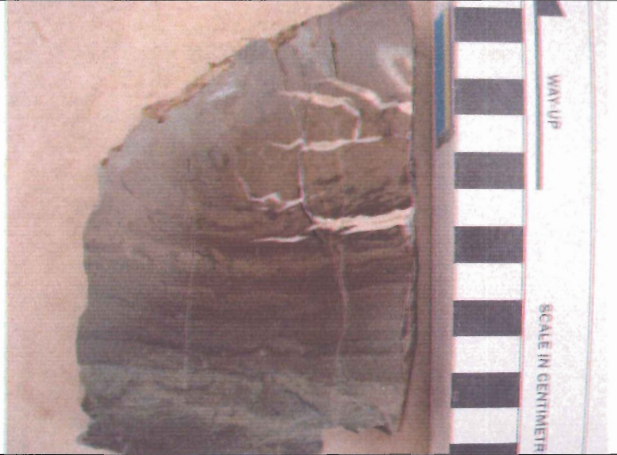
GPS Coordinates of Stromatolite mounds on the Blue Beach platform

SAND	WATER	ANGLE OF REPOSE	REMARKS
<i>pounds</i>	<i>pounds</i>		
10	0	33°	Dry
10	0.5	65°	Not hard
10	1.0	120°	Not accurate, but large obtuse angle, hard
10	1.5	120°-140°	Not accurate, but large obtuse angle, hard
10	2.0	120°-140°	Not accurate, but large obtuse angle, hard
10	2.5	120°	Not accurate, but large obtuse angle, hard
10	3.0	48°	Fairly hard
10	3.5	19°	All mixes
10	3.75	14.5°	Very slight excess of water
10	4.0	13°	Water not all absorbed
10	5.0	12°	Excess of water

Angle of repose for sand, Webster 1919,

Appendix B- Slab Observations

	<p>FG-1</p> <p>Microfacies A, B, C and D present. Root structure cutting through top microfacies D, but veining goes down to microfacies C and is more filled in. Microfacies A and B are very thin in this sample.</p>
	<p>FG-2</p> <p>Microfacies A, B, C and a tiny bit of D present. Microfacies B shows oversteepened laminae at the margins of the dome. Veining occurring mostly in microfacies C.</p>
	<p>FG-3</p> <p>Microfacies A, B, C and D present. Very good evidence of root system (black lined) and cutting down vertically into microfacies C. Microfacies D seems to be cut and domal shaped on the left section of the slab. Extensive veining present.</p>

	<p>FG-4 Microfacies A, B and C present. Microfacies A is presumably related to the mudstone layer in the cliff section, microfacies B is the very thinly laminated continuous layers with thin microbial features at the top of these laminae sets. Microfacies C is predominant in this slab with intricate veining.</p>
	<p>FG-5 Horizontal cut through stromatolite showing a birds eye view of the internal fabric. Circular laminae go around the right side of the sample but become very massive towards the centre, with veining going through the middle.</p>
	<p>FG-6 An oblique cut through the stromatolite. Goes through microfacies C and highlights the intricate veining system.</p>

	<p>FG-7</p> <p>Microfacies A, B, C and D are shown in this sample. Domal laminae sets are observed in the lower section of the stromatolite, disrupted layers near the top section show deformed layers due to possibly soft sediment deformation or root system (note black organic material in the middle of most of the disrupted layers). Veining could also be a result of post-depositional major faulting that resulted in fractures that were later infilled by hydrothermal reactions.</p>
	<p>FG-8</p> <p>Microfacies A, B and C are present in this sample. Domal laminae in microfacies C visible and intricate veining visible in microfacies C.</p>

	<p>FG-9 Root system evident in this sample that is cutting down most of it. Veining could be caused from root systems disrupting and fracturing the existing layers causing infill of vein crystals later.</p>
	<p>FG-10 Disrupted microfacies C</p>

 A photograph of a rock sample, FG-11, held next to a scale bar. The rock is dark grey to black and shows distinct horizontal layering. A scale bar with alternating black and white segments is visible on the right side of the rock. The text "WAY UP" is printed vertically on the scale bar, and "SCALE IN CENTIMETRES" is printed vertically below it. The rock surface has some faint white markings.	<p>FG-11 Microfacies B, C and D present in this sample. Thick banding for the darker laminae in microfacies D.</p>
 A photograph of a rock sample, FG-12, held next to a scale bar. The rock is dark grey to black and shows a more convoluted and disrupted sedimentary structure compared to FG-11. A scale bar with alternating black and white segments is visible on the right side of the rock. The text "SCALE IN CENTIMETERS" is printed vertically below the scale bar. The rock surface has some faint white markings.	<p>FG-12 Very disrupted sample with possible root penetrating existing layers. Microfacies C is very convoluted.</p>

Appendix C- XRD Results- Semi-quantitative approach to mineral percentages

p- pale laminae; d -dark laminae; v- vein material

Sample: Fg-1-p				
Minerals	Peak Height (cm)	Intensity Factor	Product	% within sample
Quartz	1.25	1.00	1.25	4.06
Dolomite	15.9	1.53	24.33	79.02
Calcite	1.7	1.65	2.81	9.13
Muscovite	0.4	6.00	2.40	7.80
			30.79	100.01

Sample: Fg-7-p				
Minerals	Peak Height (cm)	Intensity Factor	Product	% within sample
Dolomite	8.3	1.53	12.70	85.81
Quartz	2.1	1.0	2.1	14.19
			14.80	100

Sample: Fg-8-p				
Minerals	Peak Height (cm)	Intensity Factor	Product	% within sample
Dolomite	8.4	1.53	12.85	94.14
Quartz	0.8	1.00	0.8	5.86
			13.65	100

Sample: Fg-10-p				
Minerals	Peak Height (cm)	Intensity Factor	Product	% within sample
Dolomite	8.2	1.53	12.55	59.93
Quartz	5.0	1.0	5.0	23.88
Muscovite	0.4	6.00	2.4	11.46
Chlorite	0.2	4.95	0.99	4.73
			20.94	100

Total mineral percentages within pale laminae (from samples)		
Minerals	Total Product	%
Quartz	9.15	11.41
Dolomite	62.43	77.86
Muscovite	4.8	5.99
Chlorite	0.99	1.23
Calcite	2.81	3.50
	80.18	100

Sample: Fg-1-d				
Minerals	Peak Height (cm)	Intensity Factor	Product	% within sample
Quartz	6.35	1.00	6.35	27.03
Dolomite	8.2	1.53	12.55	53.43
Muscovite	0.6	6.00	3.6	15.33
Chlorite	0.2	4.95	0.99	4.21
			23.49	100.0

Sample: Fg-7-d				
Minerals	Peak Height (cm)	Intensity Factor	Product	% within sample
Quartz	12.60	1.00	12.60	47.0
Dolomite	2.95	1.53	4.51	16.8
Muscovite	1.20	6.00	7.20	26.9
Chlorite	0.50	4.95	2.48	9.2
			26.79	100

Sample: Fg-8-d				
Minerals	Peak Height (cm)	Intensity Factor	Product	% within sample
Quartz	8.1	1.0	8.1	32.74
Dolomite	6.2	1.53	9.47	38.28
Muscovite	0.7	6.00	4.2	16.98
Chlorite	0.6	4.95	2.97	12.00
			24.74	100

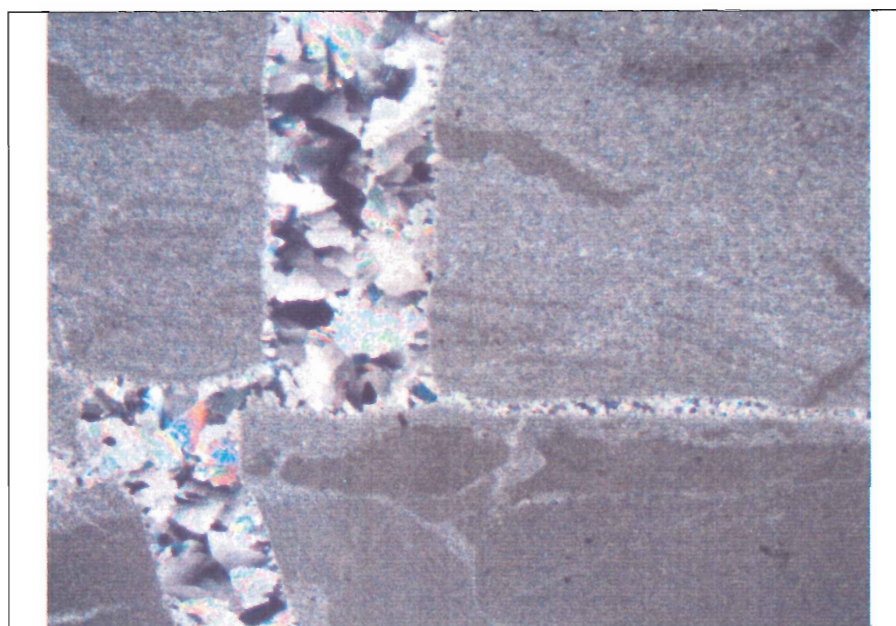
Sample: Fg-10-d				
Minerals	Peak Height (cm)	Intensity Factor	Product	% within sample
Quartz	8.0	1.0	8.0	30.34
Dolomite	6.4	1.53	9.79	37.13
Muscovite	1.1	6.00	6.6	25.03
Chlorite	0.4	4.95	1.98	7.51
			26.37	100.01

Total mineral percentages within dark laminae (from samples)		
Minerals	Total Product	%
Quartz	35.05	34.57
Dolomite	36.32	35.82
Muscovite	21.6	21.30
Chlorite	8.42	8.30
	101.39	100

Sample: Fg-1-v				
Minerals	Peak Height (cm)	Intensity Factor	Product	% within sample
Dolomite	8.6	1.53	13.16	76.16
Calcite	2.5	1.65	4.13	23.90
			17.28	100.00

Sample: Fg-10-v				
Minerals	Peak Height (cm)	Intensity Factor	Product	% within sample
Dolomite	8.5	1.53	13.00	79.56
Quartz	0.7	1.0	0.7	4.28
Calcite	1.6	1.65	2.64	16.16
			16.34	100

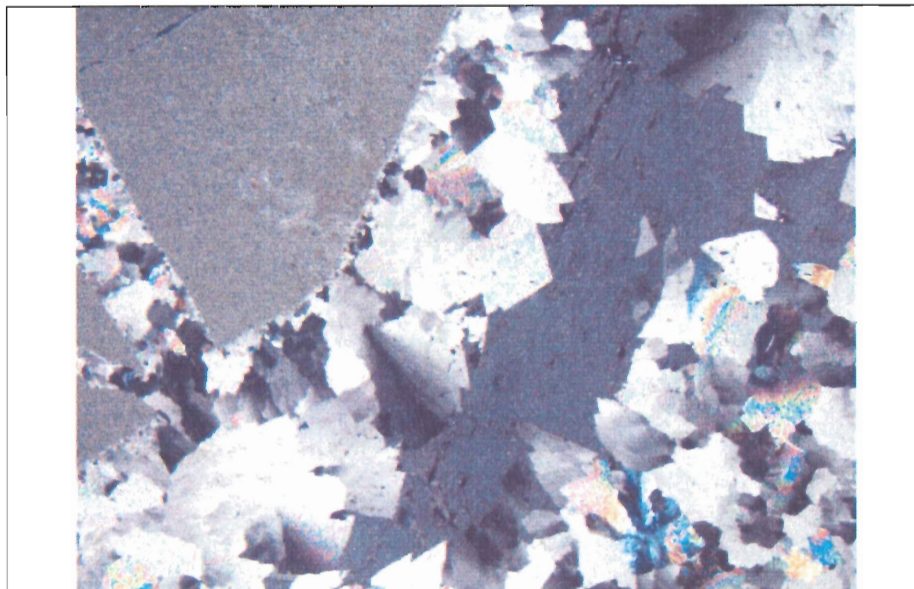
Total mineral percentages within the veins (from samples)		
Minerals	Total Product	%
Dolomite	26.16	77.79
Calcite	6.77	20.13
Quartz	0.7	2.08
	33.63	100



Fine grained material with vein and coarse grained material



Graded beds dark laminae

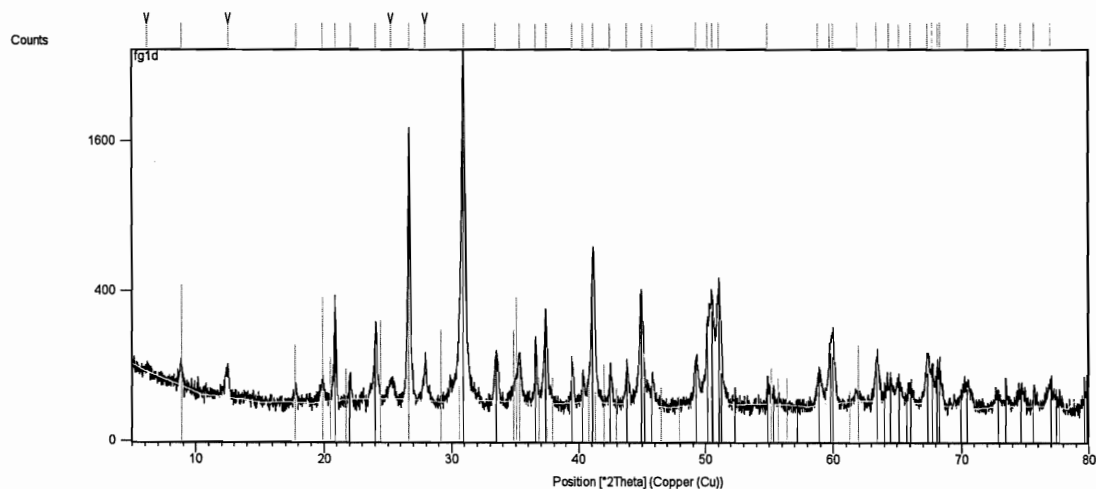


Vein Material

Measurement Parameters: (Bookmark1)

Dataset Name fg1d
File name C:\Program Files\PANalytical\X'Pert
Quantify\RESULTS\KT\fg1d.XRDML
Measurement Date / Time 2/9/2010 11:48:18 AM
Start Position [°2Th.] 5.0000
End Position [°2Th.] 80.0000
Step Size [°2Th.] 0.0200
Scan Step Time [s] 1.0000
Scan Type Pre-set time
Divergence Slit Type Fixed
Divergence Slit Size [°] 1.0329
Specimen Length [mm] 10.00
Receiving Slit Size [mm] 0.1000
Measurement Temperature [°C] 25.00
Anode Material Cu
K-Alpha1 [Å] 1.54060
K-Alpha2 [Å] 1.54443
K-Beta [Å] 1.39225

Graphics: (Bookmark2)



Peak List
00-038-0428
01-070-3755
00-007-1002

Identified Phases: (Bookmark 3)

Ref. Code	Score	Compound Name	Chemical Formula
00-036-0426	74	Dolomite	Ca Mg (C O ₃) ₂
01-070-3755	69	Quartz	Si O ₂
00-007-0025	18	Muscovite-1M, syn	K Al ₂ Si ₃ Al O ₁₀ (O H) ₂

Candidate Patterns: (Bookmark4)

Ref. Code	Score	Compound Name	Chemical Formula
01-073-9669	26	Sodium manganese(IV) manganese(III) oxide hydrate	Na _{0.58} Mn _{1.42} Mn _{0.58} O ₄ (H ₂ O) _{2.3}
01-087-1497	25	birnessite (K), syn	K _{0.5} Mn ₂ O _{4.3} (H ₂ O) _{0.5}
01-072-7297	24	Birnessite, syn	Na _{0.58} Mn ₂ O ₄ (H ₂ O) _{1.5}
01-074-7891	23	Birnessite	K _{0.312} Mn _{0.976} O ₂ (H ₂ O) _{0.37}
00-029-0885	21	Kellyite-2H	(Mn , Al) ₃ (Si , Al) ₂ O ₅ (O H) ₄
01-070-7027	20	trilanthanum pentagallosilicate	La ₃ (Ga ₅ Si O ₁₄)
00-038-0327	20	Linde B1	0.95 Na ₂ O · Al ₂ O ₃ · 3.35 Si O ₂ · 4.79 H ₂ O
00-046-1475	20	Grossite	Ca Al ₄ O ₇
00-047-1821	19	Jianshuiite	(Mg , Mn +2) Mn ₃ +4 O ₇ · 3 H ₂ O
01-085-1356	19	Chamosite	(Mg _{1.5} Fe _{7.9} Al _{2.6}) (Si _{6.2} Al _{1.8} O ₂₀) (O H) ₁₆
01-074-9333	19	Langasite	La ₃ (Ga ₄ (Ga _{1.25} Si _{0.75}) O ₁₄)
01-074-9331	19	Langasite	La ₃ (Ga ₄ (Ga _{1.22} Si _{0.78}) O ₁₄)
04-006-7956	19	Baddeleyite, cerian, syn	Ce _{0.05} Zr _{0.95} O ₂
01-074-9337	19	Langasite	La ₃ (Ga ₄ (Ga _{1.05} Si _{0.95}) O ₁₄)
01-074-9335	19	Langasite	La ₃ (Ga ₄ (Ga _{1.07} Ge _{0.07} Si _{0.86}) O ₁₄)
01-074-9336	18	Langasite	La ₃ (Ga ₄ (Ga _{1.01} Ge _{0.02} Si _{0.97}) O ₁₄)
00-041-1480	18	Albite, calcian, ordered	(Na , Ca) Al (Si , Al) ₃ O ₈
00-049-1867	18	Rosiaite	Pb Sb ₂ O ₆
01-074-9339	18	Langasite	La ₃ (Ga ₄ (Ga _{0.978} Ge _{0.048} Si _{0.942}) O ₁₄)
00-021-1227	17	Chamosite-1MIIB	(Fe , Al , Mg) ₆ (Si , Al) ₄ O ₁₀ (O H) ₈
00-030-0691	17	Geocronite	Pb ₁₄ (Sb , As) ₆ S ₂₃
01-084-1477	17	pyrochlore (Sm-exchanged), syn	(Na _{0.5} Sm _{1.5}) (Ti Sb) O ₇
04-011-1100	17	Sodium Samarium Titanium Antimony Oxide	Na _{0.5} Sm _{1.5} Ti Sb O ₇

01-073-7865	17	Potassium manganese(IV) manganese(III) oxide hydrate	K0.27 (Mn0.96 O2) (H2 O)0.69
01-084-0752	17	Albite, (low)	Na Al0.91 Si3 O8
01-089-5472	17	Baddeleyite, scandian, syn	Zr0.96 Sc0.04 O1.98
01-074-9332	16	Langasite	La3 (Ga4 (Ga1.07 Si0.93) O14)
01-074-9338	16	Langasite	La3 (Ga4 (Ga0.77 Ge0.252 Si0.876) O14)
01-083-1763	16	Rhodochrosite	Mn (C O3)
00-037-1484	16	zirconia, zirconium dioxide, zirkite	Zr O2
01-076-0927	16	sodium calcium tecto-alumosilicate	(Na0.84 Ca0.16) Al1.16 Si2.84 O8
04-006-7955	16	Baddeleyite, cerian, syn	Ce0.02 Zr0.98 O2
01-089-5471	15	Baddeleyite, scandian, syn	Zr0.98 Sc0.02 O1.99
01-074-9092	15	Langanite	La3 ((Ga5.55 Ta0.45) O14)
00-017-0933	15	Indium Borate	In B O3
01-074-9094	15	Langanite	La3 ((Ga5.48 Nb0.52) O14)
04-010-6455	15	Baddeleyite, vanadian, syn	Zr0.95 V0.05 O2
01-070-2491	15	Baddeleyite, syn	Zr O2
04-003-2101	15	cobalt antimonide	Co Sb3
01-081-1314	15	Baddeleyite, syn	Zr0.944 O2
04-004-4339	15	zirconium dioxide	Zr O2
01-075-3883	15	Skutterudite	In0.05 Co Sb3
00-044-0308	14	Silver Aluminum Nitrite Silicate	Ag8 (Al Si O4)6 (N O2)2
00-006-0427	14	Klockmannite	Cu Se
01-074-9093	14	Langanite	La3 ((Ga5.47 Nb0.53) O14)
01-074-9091	14	Langanite	La3 ((Ga5.4 Ta0.6) O14)
01-072-6680	14	Baddeleyite, vanadian, syn	(V0.03 Zr0.97) O2
01-072-6682	14	Baddeleyite, vanadian, syn	(V0.09 Zr0.91) O2
01-072-6684	14	Baddeleyite, vanadian, syn	(V0.12 Zr0.88) O2
01-072-6683	14	Baddeleyite, vanadian, syn	(V0.06 Zr0.94) O2

Peak List: (Bookmark 5)

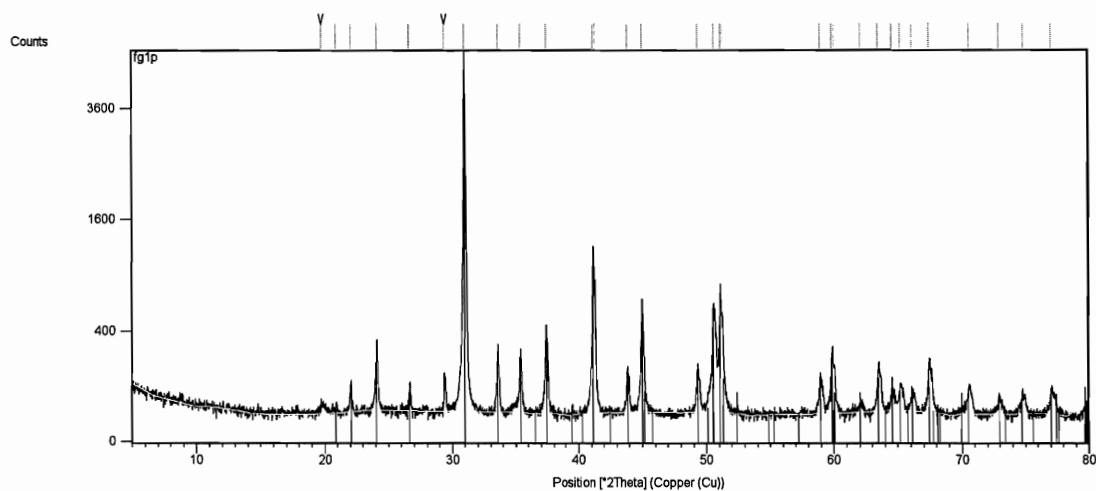
Pos. [°2Th.]	Height [cts]	d-spacing [Å]	Rel. Int. [%]
6.1923	12.01	14.27340	0.45
8.8814	66.86	9.95691	2.50
12.5613	57.20	7.04703	2.14
17.8314	27.22	4.97439	1.02
19.8993	36.50	4.46188	1.37
20.9137	272.91	4.24770	10.23
22.1026	50.41	4.02183	1.89
24.0651	211.38	3.69811	7.92
25.2372	36.37	3.52897	1.36
26.6908	1690.68	3.33999	63.35
27.9962	68.83	3.18714	2.58
30.9607	2668.95	2.88840	100.00
33.4673	97.89	2.67758	3.67
35.3104	105.96	2.54193	3.97
36.5633	173.24	2.45765	6.49

37.3857	256.44	2.40546	9.61
39.5010	84.66	2.28138	3.17
40.3482	47.07	2.23541	1.76
41.1506	647.46	2.19366	24.26
42.4646	82.10	2.12878	3.08
43.8124	79.51	2.06637	2.98
44.9720	345.12	2.01574	12.93
45.8192	61.73	1.98043	2.31
49.2764	107.11	1.84927	4.01
50.1731	250.82	1.81830	9.40
50.5321	349.71	1.80623	13.10
51.1028	432.03	1.78739	16.19
54.8784	43.44	1.67302	1.63
58.8379	52.66	1.56952	1.97
59.7539	138.89	1.54635	5.20
59.9908	209.70	1.54209	7.86
61.9181	12.00	1.49864	0.45
63.4390	99.19	1.46633	3.72
64.3791	32.11	1.44717	1.20
65.1715	35.08	1.43147	1.31
66.0341	23.90	1.41485	0.90
67.4007	105.12	1.38830	3.94
67.7496	83.03	1.38543	3.11
68.1572	83.99	1.37473	3.15
68.3384	89.24	1.37152	3.34
70.5003	42.34	1.33467	1.59
72.8254	19.61	1.29768	0.73
73.4665	21.56	1.28793	0.81
74.6634	25.65	1.27022	0.96
75.6988	30.26	1.25540	1.13
76.9393	34.43	1.23822	1.29

Measurement Parameters: (Bookmark1)

Dataset Name fg1p
File name C:\Program Files\PANalytical\X'Pert
Quantify\RESULTS\KT\fg1p.XRDML
Measurement Date / Time 2/8/2010 3:52:03 PM
Start Position [°2Th.] 5.0000
End Position [°2Th.] 80.0000
Step Size [°2Th.] 0.0200
Scan Step Time [s] 1.0000
Scan Type Pre-set time
Divergence Slit Type Fixed
Divergence Slit Size [°] 1.0329
Specimen Length [mm] 10.00
Receiving Slit Size [mm] 0.1000
Measurement Temperature [°C] 25.00
Anode Material Cu
K-Alpha1 [Å] 1.54060
K-Alpha2 [Å] 1.54443
K-Beta [Å] 1.39225

Graphics: (Bookmark2)



Peak List
00-036-0426
01-070-3755

Identified Phases: (Bookmark 3)

Ref. Code	Score	Compound Name	Chemical Formula
00-036-0426	86	Dolomite	Ca Mg (C O3)2
01-070-3755	24	Quartz	Si O2

Candidate Patterns: (Bookmark4)

Ref. Code	Score	Compound Name	Chemical Formula
00-026-0919	21	Halite, potassian, syn	K0.4 Na0.6 Cl
01-079-1347	20	Ankerite	Ca.997 (Mg.273 Fe.676 Mn.054) (C O3)2
00-007-0230	18	Manganosite, syn	Mn +2 O
01-073-3934	18	Tennantite	Cu12.54 (As0.98 Sb.02)4 S13
01-080-2197	18	Kutnohorite, magnesian	(Ca0.82 Mn0.18) (Ca0.18 Mn0.46 Fe0.13 Mg0.23) (C O3)2
04-009-9721	17	silver catena-antimonate	Ag Sb O3
01-074-1027	16	Tennantite	Cu12 As4 S13
00-043-0695	15	Kutnohorite, magnesian	Ca (Mn , Mg) (C O3)2
00-036-0394	15	Nordenskiöldine	Ca Sn +4 (B O3)2
01-074-7802	15	Dolomite	Ca (Ca0.13 Mg0.87) (C O3)2
01-084-2066	15	Ankerite	Ca1.01 Mg0.45 Fe0.54 (C O3)2
00-043-0693	14	Uranmicrolite	(Ca , U)2-x Ta2 O6 (O H)
01-074-7800	14	Dolomite	Ca (Ca0.17 Mg0.83) (C O3)2
00-003-0854	14	Chloromagnesite, syn (NR)	Mg Cl2
01-083-1531	14	Ankerite	Ca Mg0.32 Fe0.68 (C O3)2
01-075-3883	14	Skutterudite	In0.05 Co Sb3
04-011-1103	14	Sodium Ytterbium Titanium Antimony Oxide	Na0.5 Yb1.5 Ti Sb O7
01-084-1480	14	pyrochlore (Yb-exchanged), syn	(Na.5 Yb1.5) (Ti Sb) O7
04-001-2746	14	Copper, syn	Cu0.99
01-084-1479	14	pyrochlore (Dy-exchanged), syn	(Na.5 Dy1.5) (Ti Sb) O7
04-011-1102	14	Sodium Dysprosium Titanium Antimony Oxide	Na0.5 Dy1.5 Ti Sb O7
01-084-2067	14	Ankerite	Ca Mg0.27 Fe0.73 (C O3)2
00-051-1421	14	Niobocarbide	(Nb , Ta) C
00-004-0836	13	á-brass	Cu
01-075-1486	13	calcium tin bis(borate)	Ca Sn (B O3)2
00-014-0255	13	embolite, Species originally called embolite	Ag (Cl , Br)
04-011-1098	13	Cadmium Ytterbium Titanium Antimony Oxide	Cd Yb Ti Sb O7
01-084-1475	13	pyrochlore (Cd, Yb-exchanged), syn	(Cd Yb) (Ti Sb) O7
04-003-2101	13	cobalt antimonide	Co Sb3

00-012-0197	13	Trikalsilite, syn	(K , Na) Al Si O ₄
04-011-1097	13	Cadmium Gadolinium Titanium Antimony Oxide	Cd Gd Ti Sb O ₇
01-084-1474	13	pyrochlore (Cd, Gd-exchanged), syn	(Cd Gd) (Ti Sb) O ₇
04-007-5571	13	chlorapatite, syn	Na _{0.5} Ba ₄ Y _{0.5} (P O ₄) ₃ Cl
04-008-8038	13	Kutnohorite	Ca Mn (C O ₃) ₂
00-046-1378	13	Mengxianminite (NR)	(Ca , Na) ₄ (Mg , Fe , Zn) ₅ Sn ₄ Al ₁₆ O ₄₁
00-047-1846	12	Crerarite	(Pt , Pb) Bi ₃ (S , Se) ₄
00-048-1873	12	Microlite	(Ca , Na) ₂ (Ta , Nb) ₂ O ₆ (O H , F)
00-017-0933	12	Indium Borate	In B O ₃
01-075-4111	12	Putzite	Cu _{4.68} Ag _{3.48} Ge S ₆
01-076-0101	12	dodecacopper(I) tetraarsenic sulfide	Cu ₁₂ As ₄ S ₁₂
01-074-9568	12	Stistaite	Sb Sn
04-009-7320	12	̂-Cu ₇ P Se ₆ , argyrodite, syn	Cu ₇ P Se ₆
00-057-0616	12	Putzite	Cu _{4.7} Ag _{3.3} Ge S ₆
04-005-4310	12	manganosite, syn	Mn O
01-072-1451	12	Gersdorffite	Ni ₄ S _{4.7} As _{3.3}
00-046-1279	12	Rebulite	Tl ₅ Sb ₅ As ₈ S ₂₂
04-007-5561	11	chlorapatite, syn	Na _{0.5} Ba ₄ Sm _{0.5} (P O ₄) ₃ Cl
00-041-0586	11	Ankerite	Ca (Fe + ₂ , Mg) (C O ₃) ₂
00-038-0450	11	Zirkelite, heated	(Ca , Fe) (Nb , Ti , Ta , Zr) O ₄
01-078-1501	11	̂-Cr _{18.93} Fe _{4.07} C ₆ , isovite, syn	Cr _{18.93} Fe _{4.07} C ₆

Peak List: (Bookmark 5)

Pos. [°2Th.]	Height [cts]	d-spacing [Å]	Rel. Int. [%]
19.7998	18.52	4.48408	0.37
20.9074	15.53	4.24897	0.31
22.0969	84.27	4.02286	1.70
24.0946	312.62	3.69366	6.29
26.6629	77.89	3.34342	1.57
29.3921	116.13	3.03888	2.34
30.9952	4970.10	2.88526	100.00
33.6030	268.22	2.66708	5.40
35.3554	246.28	2.53880	4.96
37.3910	417.38	2.40513	8.40
41.1696	1236.90	2.19088	24.89
41.2959	637.28	2.18990	12.82
43.8361	151.31	2.06359	3.04
44.9757	621.56	2.01392	12.51
49.3064	143.65	1.84669	2.89
50.5933	577.17	1.80269	11.61
51.1119	668.82	1.78561	13.46
51.2799	441.20	1.78458	8.88
58.9516	125.23	1.56547	2.52

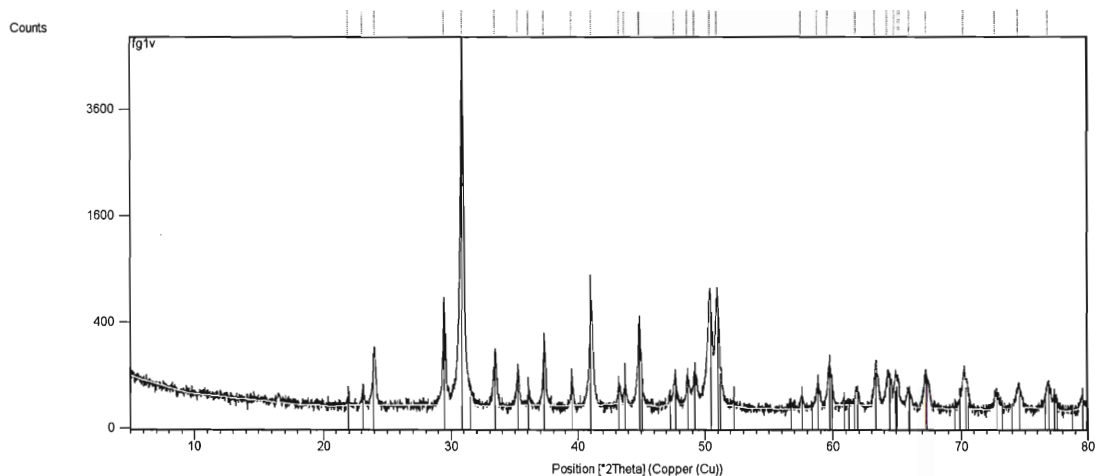
59.8640	262.11	1.54377	5.27
60.0477	148.19	1.54331	2.98
62.1038	19.48	1.49336	0.39
63.4722	160.30	1.46443	3.23
64.5506	60.80	1.44254	1.22
65.2350	69.58	1.42905	1.40
66.1102	54.78	1.41224	1.10
67.4524	186.59	1.38736	3.75
70.5605	73.50	1.33368	1.48
72.9329	43.76	1.29603	0.88
74.8402	42.50	1.26766	0.86
77.0460	67.01	1.23677	1.35

59.8640	262.11	1.54377	5.27
60.0477	148.19	1.54331	2.98
62.1038	19.48	1.49336	0.39
63.4722	160.30	1.46443	3.23
64.5506	60.80	1.44254	1.22
65.2350	69.58	1.42905	1.40
66.1102	54.78	1.41224	1.10
67.4524	186.59	1.38736	3.75
70.5605	73.50	1.33368	1.48
72.9329	43.76	1.29603	0.88
74.8402	42.50	1.26766	0.86
77.0460	67.01	1.23677	1.35

Measurement Parameters: (Bookmark1)

Dataset Name fg1v
File name C:\Program Files\PANalytical\X'Pert
Quantify\RESULTS\KT\fg1v.XRDML
Measurement Date / Time 2/9/2010 1:12:26 PM
Start Position [°2Th.] 5.0000
End Position [°2Th.] 80.0000
Step Size [°2Th.] 0.0200
Scan Step Time [s] 1.0000
Scan Type Pre-set time
Divergence Slit Type Fixed
Divergence Slit Size [°] 1.0329
Specimen Length [mm] 10.00
Receiving Slit Size [mm] 0.1000
Measurement Temperature [°C] 25.00
Anode Material Cu
K-Alpha1 [Å] 1.54060
K-Alpha2 [Å] 1.54443
K-Beta [Å] 1.39225

Graphics: (Bookmark2)

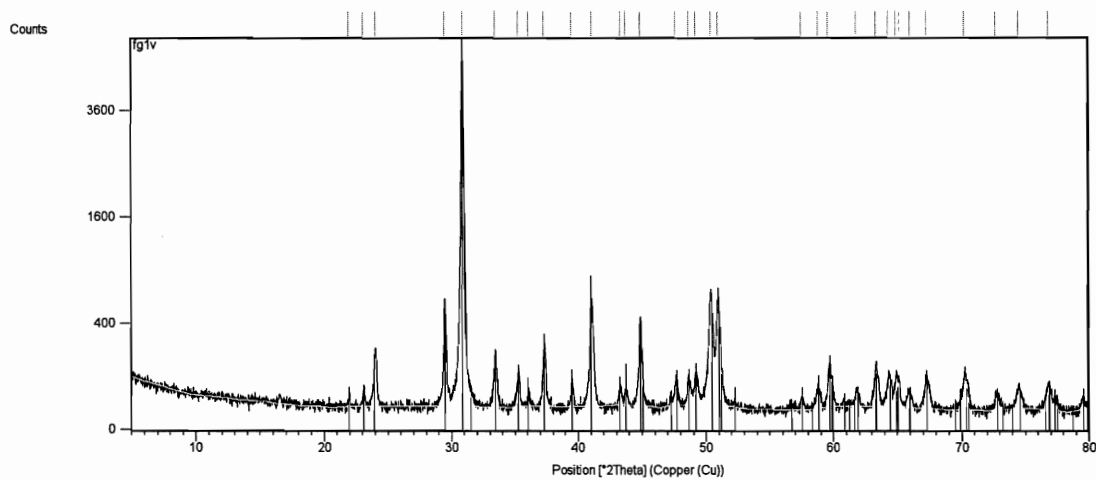


Peak List
00-036-0426
01-086-2335

Measurement Parameters: (Bookmark1)

Dataset Name fg1v
File name C:\Program Files\PANalytical\X'Pert
Quantify\RESULTS\KT\fg1v.XRDML
Measurement Date / Time 2/9/2010 1:12:26 PM
Start Position [°2Th.] 5.0000
End Position [°2Th.] 80.0000
Step Size [°2Th.] 0.0200
Scan Step Time [s] 1.0000
Scan Type Pre-set time
Divergence Slit Type Fixed
Divergence Slit Size [°] 1.0329
Specimen Length [mm] 10.00
Receiving Slit Size [mm] 0.1000
Measurement Temperature [°C] 25.00
Anode Material Cu
K-Alpha1 [Å] 1.54060
K-Alpha2 [Å] 1.54443
K-Beta [Å] 1.39225

Graphics: (Bookmark2)



Peak List
00-036-0426
01-086-2335

Identified Phases: (Bookmark 3)

Ref. Code	Score	Compound Name	Chemical Formula
00-036-0426	73	Dolomite	Ca Mg (C O3)2
01-086-2335	46	Calcite, magnesian	(Mg.064 Ca.936) (C O3)

Candidate Patterns: (Bookmark4)

Ref. Code	Score	Compound Name	Chemical Formula
01-071-5046	19	Tazheranite	Ca0.22 Ti0.22 Zr0.56 O1.78
04-011-1100	19	Sodium Samarium Titanium Antimony Oxide	Na0.5 Sm1.5 Ti Sb O7
01-084-1477	19	pyrochlore (Sm-exchanged), syn	(Na.5 Sm1.5) (Ti Sb) O7
01-083-1531	18	Ankerite	Ca Mg0.32 Fe0.68 (C O3)2
00-043-0695	18	Kutnohorite, magnesian	Ca (Mn , Mg) (C O3)2
04-011-3970	18	Rhodochrosite, syn	Mn (C O3)
01-080-2197	18	Kutnohorite, magnesian	(Ca0.82 Mn0.18) (Ca0.18 Mn0.46 Fe0.13 Mg0.23) (C O3)2
01-089-9069	18	zirconium dioxide	Zr O2
00-043-1478	17	binnite	(Cu , Fe)12 As4 S13
01-074-1027	17	Tennantite	Cu12 As4 S13
04-010-2078	17	tennantite	Cu6.48 Fe5.52 As4 S13
00-035-0801	16	Tantalcarbide, syn	Ta C
04-010-0837	16	pyrochlore	Ir4 Pb4 O13
01-079-1347	16	Ankerite	Ca.997 (Mg.273 Fe.676 Mn.054) (C O3)2
04-008-8038	16	Kutnohorite	Ca Mn (C O3)2
01-071-4759	16	Ninningerite, syn	Mg S
04-010-1154	16	binnite	Cu10 Zn2 Sb0.6 As3.4 S13
04-007-6102	16	Ru,Pb pyrochlore, syn	Ru2 Pb2 O7
01-076-0101	16	dodecacopper(I) tetraarsenic sulfide	Cu12 As4 S12
01-084-1478	16	pyrochlore (Gd-exchanged), syn	(Na.5 Gd1.5) (Ti Sb) O7
04-011-1101	16	Sodium Gadolinium Titanium Antimony Oxide	Na0.5 Gd1.5 Ti Sb O7
01-089-2001	16	Bornhardtite	Co3 Se4
04-011-1097	16	Cadmium Gadolinium Titanium Antimony Oxide	Cd Gd Ti Sb O7
01-084-1474	16	pyrochlore (Cd, Gd-exchanged), syn	(Cd Gd) (Ti Sb) O7
01-074-4547	15	Zirconia - synthetic	Zr0.88 O1.78
01-083-1763	15	Rhodochrosite	Mn (C O3)
04-011-2415	15	fluorite	Zr4 N2 O5
01-075-3659	15	Perovskite	Sr Mn0.91 Ga0.09 O2.93
01-075-3883	15	Skutterudite	In0.05 Co Sb3
01-084-1479	14	pyrochlore (Dy-exchanged), syn	(Na.5 Dy1.5) (Ti Sb) O7

04-011-1102	14	Sodium Dysprosium Titanium Antimony Oxide	Na _{0.5} Dy _{1.5} Ti Sb O ₇
01-074-1071	14	Tennantite	Cu ₁₂ As _{3.40} Sb _{.60} S ₁₃
00-041-0599	14	osmium, iridian, Previously called iridosmine	(Ir , Os)
00-029-0901	13	Wodginite	(Ta , Mn , Sn) O ₂
00-017-0933	13	Indium Borate	In B O ₃
01-073-3684	13	Perovskite	La Al O ₃
00-043-0693	13	Uranmicrolite	(Ca , U) _{2-x} Ta ₂ O ₆ (O H)
01-074-7357	13	Unnamed_Columbite	(Fe _{0.24} Mn _{0.76}) (Nb ₂ O ₆)
04-003-2101	13	cobalt antimonide	Co Sb ₃
00-032-0731	12	Potassium Aluminum Silicate	K _{1.25} Al _{1.25} Si _{0.75} O ₄
04-009-9721	12	silver catena-antimonate	Ag Sb O ₃
00-003-0854	12	Chloromagnesite, syn (NR)	Mg Cl ₂
01-073-3934	12	Tennantite	Cu _{12.54} (As _{0.98} Sb _{.02}) ₄ S ₁₃
00-046-1378	12	Mengxianminite (NR)	(Ca , Na) ₄ (Mg , Fe , Zn) ₅ Sn ₄ Al ₁₆ O ₄₁
04-008-6181	11	Eskolaite, syn	Cr ₂ O ₃
01-073-8127	11	Pyrite, syn	Fe S _{1.96}
00-033-0659	11	Ferrocolumbite	(Fe , Mn) (Nb , Ta) ₂ O ₆
01-071-5036	11	bronze ç', syn	(Cu ₆ Sn ₅) _{0.1818}
04-007-2613	11	Pyrite, syn	Fe S ₂
00-054-1131	11	Zirconolite-3O	Ca Zr Ti ₂ O ₇

Peak List: (Bookmark 5)

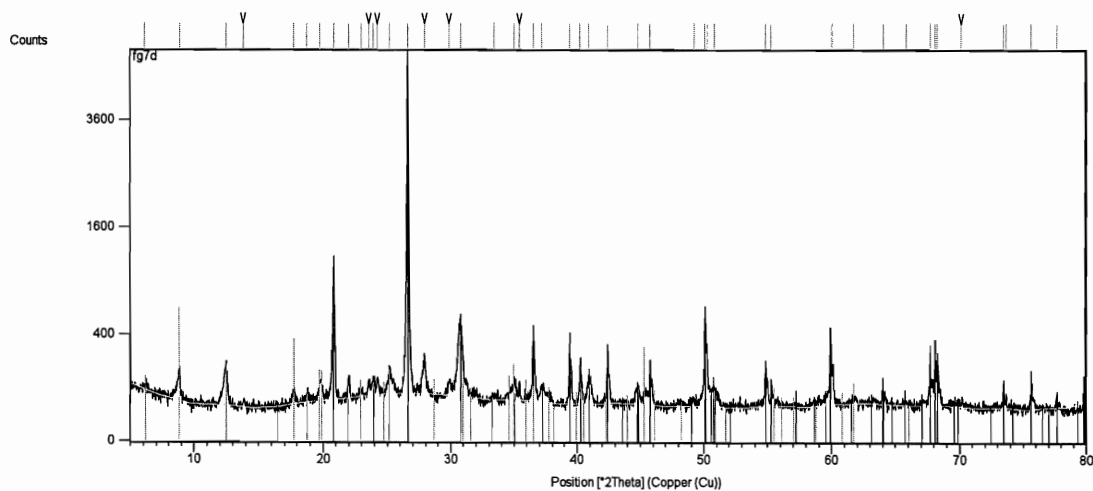
Pos. [°2Th.]	Height [cts]	d-spacing [Å]	Rel. Int. [%]
21.9585	10.49	4.04790	0.20
23.1187	40.43	3.84733	0.77
24.0535	188.20	3.69987	3.56
29.4564	575.25	3.03239	10.89
30.9127	5282.99	2.89278	100.00
33.4538	207.26	2.67863	3.92
35.2400	111.76	2.54684	2.12
36.0747	38.59	2.48981	0.73
37.3076	270.07	2.41032	5.11
39.5196	75.17	2.28035	1.42
41.0635	574.25	2.19812	10.87
43.3188	45.61	2.08876	0.86
43.7160	32.83	2.07070	0.62
44.8463	369.36	2.02110	6.99
47.6665	72.21	1.90790	1.37
48.6441	84.09	1.87182	1.59
49.1954	101.10	1.85213	1.91
50.4225	637.33	1.80989	12.06
50.9752	684.66	1.79156	12.96
57.5331	21.67	1.60197	0.41
58.8140	53.99	1.57010	1.02
59.6370	102.62	1.55039	1.94
61.7939	36.60	1.50135	0.69
63.3205	117.76	1.46878	2.23

64.3405	90.76	1.44794	1.72
64.9243	90.56	1.43514	1.71
65.1355	63.30	1.43455	1.20
65.9888	38.69	1.41454	0.73
67.2562	93.79	1.39093	1.78
70.2340	104.66	1.33907	1.98
72.6751	30.68	1.29999	0.58
74.4975	51.70	1.27264	0.98
76.8233	59.37	1.23980	1.12

Measurement Parameters: (Bookmark1)

Dataset Name fg7d
File name C:\Program Files\PANalytical\X'Pert
Quantify\RESULTS\KT\fg7d.XRDML
Measurement Date / Time 2/10/2010 12:21:04 PM
Start Position [°2Th.] 5.0000
End Position [°2Th.] 80.0000
Step Size [°2Th.] 0.0200
Scan Step Time [s] 1.0000
Scan Type Pre-set time
Divergence Slit Type Fixed
Divergence Slit Size [°] 1.0329
Specimen Length [mm] 10.00
Receiving Slit Size [mm] 0.1000
Measurement Temperature [°C] 25.00
Anode Material Cu
K-Alpha [Å] 1.54060
K-Alpha2 [Å] 1.54443
K-Beta [Å] 1.39225

Graphics: (Bookmark2)



Peak List
00-048-1045
00-007-0042
00-057-1044
01-074-7800

Identified Phases: (Bookmark 3)

Ref. Code	Score	Compound Name	Chemical Formula
00-046-1045	71	Quartz, syn	Si O ₂
00-007-0042	22	Muscovite-3T	(K , Na) (Al , Mg , Fe) ₂ (Si _{3.1} Al _{0.9}) O ₁₀ (O H) ₂
00-052-1044	39	Chlorite-serpentine (NR)	(Mg , Al) ₆ (Si , Al) ₄ O ₁₀ (O H) ₈
01-074-7800	42	Dolomite	Ca (Ca _{0.17} Mg _{0.83}) (C O ₃) ₂

Candidate Patterns: (Bookmark4)

Ref. Code	Score	Compound Name	Chemical Formula
01-076-0927	31	sodium calcium tecto-alumosilicate	(Na _{0.84} Ca _{0.16}) Al _{1.16} Si _{2.84} O ₈
01-084-0752	27	Albite, (low)	Na Al _{0.91} Si ₃ O ₈
01-083-1466	25	sodium alumosilicate	Na _{0.986} (Al _{1.005} Si _{2.995} O ₈)
00-041-1480	24	Albite, calcian, ordered	(Na , Ca) Al (Si , Al) ₃ O ₈
01-070-3752	24	Albite	(Na _{0.98} Ca _{0.02}) (Al _{1.02} Si _{2.98} O ₈)
00-009-0466	22	Albite, ordered	Na Al Si ₃ O ₈
00-021-0982	22	Polyhalite	K ₂ Ca ₂ Mg (S O ₄) ₄ · 2 H ₂ O
01-070-2157	19	Polyhalite	K ₂ Ca ₂ Mg (S O ₄) ₄ (H ₂ O) ₂
00-018-0877	19	Taenite	(Fe , Ni)
00-010-0393	18	Albite, disordered	Na (Si ₃ Al) O ₈
00-019-1184	18	Albite, ordered	Na Al Si ₃ O ₈
01-089-7574	17	titanite (Al-rich, F-containing), syn	Ca (Ti _{0.181} Al _{0.819}) (O _{0.181} F _{0.819}) (Si O ₄)
00-029-0348	17	Brandtite	Ca ₂ Mn + ₂ (As O ₄) ₂ · 2 H ₂ O
00-020-0528	17	Anorthite, sodian, ordered	(Ca , Na) (Al , Si) ₂ Si ₂ O ₈
04-011-6768	17	albite high	K _{0.22} Na _{0.78} Al Si ₃ O ₈
01-076-0926	16	sodium calcium tecto-alumosilicate	(Na _{0.75} Ca _{0.25}) (Al _{1.26} Si _{2.74} O ₈)
01-083-2215	16	potassium sodium alumosilicate	K _{0.2} Na _{0.8} Al Si ₃ O ₈
01-079-1254	15	albite, Ca-rich, calcium sodium tecto-alumosilicate	(Ca _{.38} Na _{.62}) (Al _{1.38} Si _{2.62} O ₈)
00-025-0306	15	Clinopyroxene, titanian aluminian (NR)	Ca (Ti , Mg , Al) (Si , Al) ₂ O ₆
01-083-1371	15	calcium sodium alumosilicate	Ca _{0.64} Na _{0.35} (Al _{1.63} Si _{2.37} O ₈)
00-035-0463	15	á-Li Al Si ₄ O ₁₀	Li Al Si ₄ O ₁₀
00-034-0185	15	Aegirine, syn	Na Fe + ₃ (Si O ₃) ₂
00-029-0865	14	Kanoite	(Mn + ₂ , Mg) ₂ (Si ₂ O ₆)
00-041-1370	14	Diopside	Ca (Mg , Al) (Si , Al) ₂ O ₆
00-047-1782	14	Unnamed mineral (NR)	Ba (Ti , V) ₈ (O , O H) ₁₆
04-007-5466	14	sodium tecto-alumotrisilicate	Na Al Si ₃ O ₈
00-014-0346	14	Magnesium Aluminum Silicate	Mg O · Al ₂ O ₃ · Si O ₂
01-071-1066	14	sodium iron(III) catena-silicate	Na Fe (Si ₂ O ₆)

00-041-1483	14	Augite, aluminian	Ca (Mg , Fe , Al) (Si , Al) ₂ O ₆
01-070-7027	14	trilanthanum pentagallosilicate	La ₃ (Ga ₅ Si O ₁₄)
00-037-1484	14	zirconia, zirconium dioxide, zirkite	Zr O ₂
00-047-2499	14	Tsaregorodtsevit	C ₄ H ₁₂ Al N O ₁₂ Si ₅
01-085-0878	14	sodium calcium aluminosilicate	Na _{0.48} Ca _{0.52} Al _{1.52} Si _{2.48} O ₈
01-077-0433	14	distrontium zinc digermanate, strontium-melilite gemanian	Sr ₂ Zn Ge ₂ O ₇
01-073-8555	13	Calcium sodium magnesium Aluminum iron catena- aluminosilicate*	(Ca _{0.96} Na _{0.04}) (Mg _{0.86} Al _{0.07} Fe _{0.06}) (Si _{1.89} Al _{0.11} O ₆)
01-084-1302	13	Muscovite-2M1	K Al _{2.9} Si _{3.1} O ₁₀ (O H) ₂
01-071-5178	13	gallium-sodalite, syn, octasodium tecto- hexagallohexasilicate dibromide	Na ₈ (Ga Si O ₄) ₆ Br ₂
01-078-1392	13	calcium magnesium aluminium catena-aluminosilicate	Ca (Mg _{0.70} Al _{0.30}) ((Si _{1.70} Al _{0.30}) O ₆)
01-072-6045	13	sodium lithium iron(III) catena- disilicate	(Na _{0.948} Li _{0.052}) Fe (Si ₂ O ₆)
04-011-6849	13	muscovite	K Al ₂ Si ₄ O ₁₀ (O H) ₂
01-078-0433	13	sodium calcium aluminosilicate	Na _{0.45} Ca _{0.55} Al _{1.55} Si _{2.45} O ₈
00-030-0691	13	Geocronite	Pb ₁₄ (Sb , As) ₆ S ₂₃
01-076-0668	13	Muscovite-2M1	K ₂ (Al _{3.74} Fe _{0.26}) (Si ₆ Al ₂ O ₂₀) (O H) ₄
01-073-9860	13	Potassium sodium Aluminum iron magnesium phyllo- aluminosilicate hydroxide fluoride *	K _{0.92} Na _{0.08} Al _{1.86} Fe _{0.14} Mg _{0.02} (Al _{0.97} Si _{3.03} O ₁₀) (O H) _{1.91} F _{0.09}
00-021-1198	13	Tantite, syn	Ta ₂ O ₅
00-044-1429	13	Natromontebasite	Na Al (P O ₄) (O H)
01-087-0691	13	Muscovite-2M1, magnesian, manganian	(K _{.94} Na _{.06}) (Mg _{.08} Al _{1.75} Fe _{.15} Mn _{.02}) (Al _{.92} Si _{3.08}) O ₁₀ (O H) ₂
01-078-0434	13	sodium calcium aluminosilicate	Na _{0.45} Ca _{0.55} Al _{1.55} Si _{2.45} O ₈
00-043-1474	13	Geocronite	Pb ₁₄ Sb ₆ S ₂₃
01-073-9861	13	Potassium sodium Aluminum iron phyllo-aluminosilicate hydroxide fluoride *	K _{0.96} Na _{0.04} Al _{1.71} Fe _{0.29} (Al _{0.91} Si _{3.09} O ₁₀) (O H) _{1.78} F _{0.22}

Peak List: (Bookmark 5)

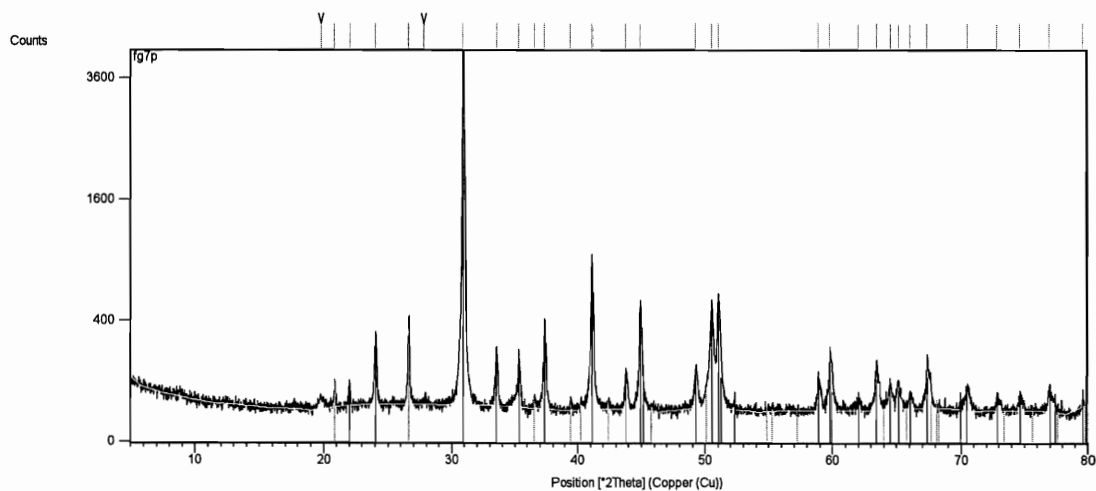
Pos. [°2Th.]	Height [cts]	d-spacing [Å]	Rel. Int. [%]
6.1467	17.56	14.37921	0.33
8.8702	130.29	9.96947	2.44
12.4952	167.93	7.08418	3.15
13.8030	10.92	6.41579	0.20
17.7650	42.85	4.99282	0.80

18.7869	33.76	4.72349	0.63
19.8013	68.12	4.48376	1.28
20.8607	1128.80	4.25838	21.14
22.0391	77.07	4.03329	1.44
22.9487	23.28	3.87543	0.44
23.5629	54.27	3.77578	1.02
23.9282	56.45	3.71897	1.06
24.2556	55.16	3.66951	1.03
25.1779	113.98	3.53714	2.14
26.6278	5338.46	3.34773	100.00
27.9411	160.20	3.19330	3.00
29.9146	52.47	2.98698	0.98
30.7934	445.16	2.90371	8.34
33.4639	11.26	2.67784	0.21
35.0041	57.78	2.56347	1.08
35.4316	27.68	2.53351	0.52
36.5270	370.32	2.46001	6.94
37.1651	45.91	2.41923	0.86
39.4461	293.10	2.28443	5.49
40.2673	155.76	2.23972	2.92
40.8856	75.62	2.20727	1.42
42.4186	247.66	2.13098	4.64
44.8101	62.42	2.02265	1.17
45.7801	121.43	1.98203	2.27
49.2466	14.34	1.85032	0.27
50.1180	509.38	1.81867	9.54
50.2667	279.64	1.81814	5.24
50.8084	61.82	1.79556	1.16
54.8572	121.74	1.67223	2.28
55.3154	68.66	1.65945	1.29
59.9523	309.53	1.54171	5.80
60.1146	160.90	1.54176	3.01
61.7131	12.84	1.50188	0.24
64.0876	26.90	1.45184	0.50
65.8982	6.58	1.41627	0.12
67.7178	134.49	1.38257	2.52
68.1135	186.77	1.37550	3.50
68.2853	186.61	1.37246	3.50
70.1348	10.63	1.34072	0.20
73.4534	62.47	1.28813	1.17
73.6632	35.18	1.28498	0.66
75.6433	73.00	1.25618	1.37
77.6548	34.77	1.22859	0.65

Measurement Parameters: (Bookmark1)

Dataset Name fg7p
File name C:\Program Files\PANalytical\X'Pert
Quantify\RESULTS\KT\fg7p.XRDML
Measurement Date / Time 2/10/2010 11:13:36 AM
Start Position [°2Th.] 5.0000
End Position [°2Th.] 80.0000
Step Size [°2Th.] 0.0200
Scan Step Time [s] 1.0000
Scan Type Pre-set time
Divergence Slit Type Fixed
Divergence Slit Size [°] 1.0329
Specimen Length [mm] 10.00
Receiving Slit Size [mm] 0.1000
Measurement Temperature [°C] 25.00
Anode Material Cu
K-Alpha1 [Å] 1.54060
K-Alpha2 [Å] 1.54443
K-Beta [Å] 1.39225

Graphics: (Bookmark2)



Peak List
00-035-0426
01-070-3755

Identified Phases: (Bookmark 3)

Ref. Code	Score	Compound Name	Chemical Formula
00-036-0426	83	Dolomite	Ca Mg (C O ₃) ₂
01-070-3755	36	Quartz	Si O ₂

Candidate Patterns: (Bookmark4)

Ref. Code	Score	Compound Name	Chemical Formula
04-011-1102	19	Sodium Dysprosium Titanium Antimony Oxide	Na _{0.5} Dy _{1.5} Ti Sb O ₇
01-084-1479	19	pyrochlore (Dy-exchanged), syn	(Na _{0.5} Dy _{1.5}) (Ti Sb) O ₇
01-074-4547	17	Zirconia - synthetic	Zr _{0.88} O _{1.78}
01-071-5046	17	Tazheranite	Ca _{0.22} Ti _{0.22} Zr _{0.56} O _{1.78}
04-011-1103	17	Sodium Ytterbium Titanium Antimony Oxide	Na _{0.5} Yb _{1.5} Ti Sb O ₇
01-084-1480	17	pyrochlore (Yb-exchanged), syn	(Na _{0.5} Yb _{1.5}) (Ti Sb) O ₇
01-084-1475	16	pyrochlore (Cd, Yb-exchanged), syn	(Cd Yb) (Ti Sb) O ₇
04-011-1098	16	Cadmium Ytterbium Titanium Antimony Oxide	Cd Yb Ti Sb O ₇
01-070-0622	16	á-Cr O O D	Cr O O D
01-085-1375	16	á-Cr O (O D), grimaldiite deuterated, syn	Cr O (O D)
01-074-1027	15	Tennantite	Cu ₁₂ As ₄ S ₁₃
01-076-0101	15	dodecacopper(I) tetraarsenic sulfide	Cu ₁₂ As ₄ S ₁₂
04-010-1154	15	binnite	Cu ₁₀ Zn ₂ Sb _{0.6} As _{3.4} S ₁₃
00-043-1478	15	binnite	(Cu , Fe) ₁₂ As ₄ S ₁₃
01-074-1071	15	Tennantite	Cu ₁₂ As _{3.40} Sb _{0.60} S ₁₃
01-084-1474	15	pyrochlore (Cd, Gd-exchanged), syn	(Cd Gd) (Ti Sb) O ₇
04-011-1097	15	Cadmium Gadolinium Titanium Antimony Oxide	Cd Gd Ti Sb O ₇
04-010-2078	15	tennantite	Cu _{6.48} Fe _{5.52} As ₄ S ₁₃
00-036-0394	15	Nordenskiöldine	Ca Sn +4 (B O ₃) ₂
00-051-1421	15	Niobocarbide	(Nb , Ta) C
00-017-0933	15	Indium Borate	In B O ₃
04-009-9721	14	silver catena-antimonate	Ag Sb O ₃
01-074-7800	14	Dolomite	Ca (Ca _{0.17} Mg _{0.83}) (C O ₃) ₂
01-073-3934	14	Tennantite	Cu _{12.54} (As _{0.98} Sb _{0.02}) ₄ S ₁₃
00-047-1846	14	Crerarite	(Pt , Pb) Bi ₃ (S , Se) ₄
04-008-9876	14	Grimaldiite, syn	H Cr O ₂
01-084-2067	14	Ankerite	Ca Mg _{0.27} Fe _{0.73} (C O ₃) ₂
04-003-2101	14	cobalt antimonide	Co Sb ₃
01-075-1486	13	calcium tin bis(borate)	Ca Sn (B O ₃) ₂
00-014-0409	13	Huntite	Mg ₃ Ca (C O ₃) ₄

01-089-6287	13	hydroxylpyromorphite, syn, pentalead tris(phosphate(V)) hydroxide	Pb ₅ (P O ₄) ₃ (O H)
04-011-1101	13	Sodium Gadolinium Titanium Antimony Oxide	Na _{0.5} Gd _{1.5} Ti Sb O ₇
01-084-1478	13	pyrochlore (Gd-exchanged), syn	(Na _{0.5} Gd _{1.5}) (Ti Sb) O ₇
01-075-3883	13	Skutterudite	In _{0.05} Co Sb ₃
00-046-1378	13	Mengxianminite (NR)	(Ca , Na) ₄ (Mg , Fe , Zn) ₅ Sn ₄ Al ₁₆ O ₄₁
04-007-2551	13	iron silicide	Fe Si
00-038-0450	12	Zirkelite, heated	(Ca , Fe) (Nb , Ti , Ta , Zr) O ₄
01-074-9338	12	Langasite	La ₃ (Ga ₄ (Ga _{0.77} Ge _{0.252} Si _{0.876}) O ₁₄)
04-011-2415	12	fluorite	Zr ₄ N ₂ O ₅
00-043-0693	12	Uranmicrolite	(Ca , U) _{2-x} Ta ₂ O ₆ (O H)
04-005-4310	11	manganosite, syn	Mn O
00-007-0230	11	Manganosite, syn	Mn +2 O
01-076-1694	11	Salesite	Cu (I O ₃) (O H)
01-074-9333	11	Langasite	La ₃ (Ga ₄ (Ga _{1.25} Si _{0.75}) O ₁₄)
00-043-0695	11	Kutnohorite, magnesian	Ca (Mn , Mg) (C O ₃) ₂
00-041-0586	11	Ankerite	Ca (Fe +2 , Mg) (C O ₃) ₂
01-074-9092	11	Langanite	La ₃ ((Ga _{5.55} Ta _{0.45}) O ₁₄)
01-074-9093	11	Langanite	La ₃ ((Ga _{5.47} Nb _{0.53}) O ₁₄)
00-047-1769	11	Kieftite	Co Sb ₃
01-083-1763	11	Rhodochrosite	Mn (C O ₃)

Peak List: (Bookmark 5)

Pos. [°2Th.]	Height [cts]	d-spacing [Å]	Rel. Int. [%]
19.8577	17.51	4.47115	0.42
20.8829	71.72	4.25390	1.74
22.0482	54.52	4.03164	1.32
24.0698	278.10	3.69741	6.73
26.6549	368.39	3.34440	8.92
27.8736	17.68	3.20089	0.43
30.9456	4130.24	2.88978	100.00
33.5377	209.61	2.67212	5.07
35.3191	160.91	2.54132	3.90
36.5524	22.84	2.45836	0.55
37.3739	386.92	2.40619	9.37
39.4715	24.06	2.28302	0.58
41.1258	927.93	2.19311	22.47
41.2426	561.55	2.19261	13.60
43.8127	112.23	2.06464	2.72
44.9366	516.54	2.01558	12.51
49.2867	125.38	1.84738	3.04
50.5490	520.70	1.80417	12.61
51.0722	573.92	1.78690	13.90
58.8758	103.44	1.56730	2.50

59.8164	188.41	1.54489	4.56
62.0455	19.63	1.49463	0.48
63.4429	153.63	1.46503	3.72
64.5501	54.37	1.44255	1.32
65.1434	65.01	1.43084	1.57
66.0386	36.13	1.41360	0.87
67.4021	173.58	1.38828	4.20
70.4863	56.95	1.33490	1.38
72.8721	31.67	1.29696	0.77
74.6552	26.18	1.27034	0.63
76.9465	58.69	1.23813	1.42
79.6700	16.81	1.20251	0.41

Identified Phases: (Bookmark 3)

Ref. Code	Score	Compound Name	Chemical Formula
01-070-7344	68	Quartz	Si O ₂
01-074-7804	53	Dolomite	Ca (Ca _{0.14} Mg _{0.86}) (C O ₃) ₂

Candidate Patterns: (Bookmark4)

Ref. Code	Score	Compound Name	Chemical Formula
01-084-1478	37	pyrochlore (Gd-exchanged), syn	(Na _{0.5} Gd _{1.5}) (Ti Sb) O ₇
04-011-1101	37	Sodium Gadolinium Titanium Antimony Oxide	Na _{0.5} Gd _{1.5} Ti Sb O ₇
01-084-1474	35	pyrochlore (Cd, Gd-exchanged), syn	(Cd Gd) (Ti Sb) O ₇
04-011-1097	35	Cadmium Gadolinium Titanium Antimony Oxide	Cd Gd Ti Sb O ₇
04-011-1100	34	Sodium Samarium Titanium Antimony Oxide	Na _{0.5} Sm _{1.5} Ti Sb O ₇
01-084-1477	34	pyrochlore (Sm-exchanged), syn	(Na _{0.5} Sm _{1.5}) (Ti Sb) O ₇
04-007-6102	33	Ru,Pb pyrochlore, syn	Ru ₂ Pb ₂ O ₇
00-024-0201	32	Augite	Ca (Fe , Mg) Si ₂ O ₆
01-071-5046	32	Tazheranite	Ca _{0.22} Ti _{0.22} Zr _{0.56} O _{1.78}
01-071-6477	32	calcium magnesium iron catena- disilicate	Ca (Mg _{0.69} Fe _{0.31}) (Si ₂ O ₆)
04-009-9721	31	silver catena-antimonate	Ag Sb O ₃
00-040-0495	31	Petedunnite, syn	Ca Zn Si ₂ O ₆
00-013-0197	27	Betafite-C, heated	(Ca , U) _{2-x} (Nb , Ti) ₂ O ₆ (O H , F) _{1-z}
01-086-0747	26	sodium calcium scandium zinc catena-disilicate	(Na _{0.1} Ca _{0.9}) (Sc _{0.1} Zn _{0.9}) (Si ₂ O ₆)
00-052-1044	26	Chlorite-serpentine (NR)	(Mg , Al) ₆ (Si , Al) ₄ O ₁₀ (O H) ₈
01-072-7140	25	calcium potassium magnesium aluminum alumosilicate	(Ca _{0.75} K _{0.23} Mg _{0.02}) (Mg _{0.73} Al _{0.27}) (Si _{1.97} Al _{0.03}) O ₆
00-038-0413	25	Johannsenite	Ca Mn + ₂ Si ₂ O ₆
01-074-7891	24	Birnessite	K _{0.312} Mn _{0.976} O ₂ (H ₂ O) _{0.37}
01-072-0765	24	lead tungstate	Pb W O ₄
01-089-9069	24	zirconium dioxide	Zr O ₂
01-086-0746	23	sodium calcium scandium zinc catena-disilicate	(Na _{0.15} Ca _{0.85}) (Sc _{0.15} Zn _{0.85}) (Si ₂ O ₆)
03-065-3562	23	Klockmannite	Cu Se
00-018-0877	23	Taenite	(Fe , Ni)
00-029-0865	23	Kanoite	(Mn + ₂ , Mg) ₂ (Si ₂ O ₆)
04-010-0837	23	pyrochlore	Ir ₄ Pb ₄ O ₁₃
01-071-1498	23	calcium iron catena-silicate	Ca Fe Si ₂ O ₆

04-011-6677	23	hedenbergite, syn	Ca Fe Si ₂ O ₆
01-089-0832	23	calcium magnesium iron silicon oxide	Ca _{1.003} (Mg _{0.895} Fe _{0.105}) ((Si _{1.901} Fe _{0.1}) O ₆)
01-089-0836	22	calcium magnesium iron silicon oxide	Ca _{1.018} (Mg _{0.733} Fe _{0.293}) ((Si _{1.67} Fe _{0.304}) O ₆)
00-055-0572	22	Karupmoellerite-Ca	(Na , Ca , K) ₂ Ca (Nb , Ti) ₄ (Si ₄ O ₁₂) ₂ (O , O H) ₄ · 7 H ₂ O
00-011-0267	22	Simplotite	Ca V ₄ O ₉ · 5 H ₂ O
01-070-3753	22	Augite	(Ca Mg _{0.74} Fe _{0.25}) Si ₂ O ₆
01-086-0745	21	sodium calcium scandium zinc catena-disilicate	(Na _{0.25} Ca _{0.75}) (Sc _{0.25} Zn _{0.75}) (Si ₂ O ₆)
01-074-2426	21	Hedenbergite, manganoan	Ca _{0.91} Mn _{0.18} Fe _{0.91} Si ₂ O ₆
01-089-0837	21	calcium magnesium iron silicon oxide	Ca _{0.991} (Mg _{0.641} Fe _{0.342}) (Si _{1.6} Fe _{0.417}) O ₆
00-025-1456	21	Calcium Aluminum Silicate	Ca Al ₂ Si O ₆
01-089-0834	21	calcium magnesium iron silicon oxide	Ca _{1.022} (Mg _{0.857} Fe _{0.122}) ((Si _{1.877} Fe _{0.144}) O ₆)
01-086-0743	21	sodium calcium scandium zinc catena-disilicate	(Na _{0.35} Ca _{0.65}) (Sc _{0.35} Zn _{0.65}) (Si ₂ O ₆)
01-081-0487	21	calcium titanium magnesium aluminum catena-alumosilicate	(Ca _{0.959} Ti _{0.041}) (Mg _{0.987} Al _{0.013}) (Si _{1.905} Al _{0.095} O ₆)
01-076-0543	21	Pigeonite	Ca _{0.18} Mg _{1.21} Fe _{0.58} (Si O ₃) ₂
01-083-0094	21	magnesium iron calcium catena-disilicate	(Mg _{0.948} Fe _{0.052}) (Ca _{0.96} Mg _{0.04}) (Si ₂ O ₆)
01-073-9803	21	Magnesium iron Aluminum calcium sodium catena-alumosilicate *	(Mg _{0.88} Fe _{0.09} Al _{0.03}) (Ca _{0.95} Na _{0.01} Fe _{0.04}) (Si _{1.98} Al _{0.02} O ₆)
01-089-1997	21	disilver iron tetrathioantennate	Ag ₂ Fe Sn S ₄
01-083-0086	21	Diopside, ferroan	(Mg _{0.992} Fe _{0.008}) (Ca _{0.962} Mg _{0.038}) (Si ₂ O ₆)
01-083-0088	21	magnesium iron calcium catena-disilicate	(Mg _{0.984} Fe _{0.016}) (Ca _{0.976} Mg _{0.016} Fe _{0.008}) (Si ₂ O ₆)
01-083-0096	20	magnesium iron calcium catena-disilicate	(Mg _{0.976} Fe _{0.024}) (Ca _{0.972} Mg _{0.008} Fe _{0.020}) (Si ₂ O ₆)
01-083-0090	20	magnesium iron calcium catena-disilicate	(Mg _{0.970} Fe _{0.030}) (Ca _{0.97} Mg _{0.024} Fe _{0.006}) (Si ₂ O ₆)
01-075-4239	20	Diopside	Ca _{0.916} Na _{0.066} Mg _{0.926} Ti _{0.086} Si _{1.96} B _{0.018} O ₆
01-076-0927	20	sodium calcium tecto-alumosilicate	(Na _{0.84} Ca _{0.16}) Al _{1.16} Si _{2.84} O ₈
01-089-0835	20	calcium magnesium iron silicon oxide	Ca _{1.007} (Mg _{0.805} Fe _{0.214}) ((Si _{1.75} Fe _{0.241}) O ₆)

Peak List: (Bookmark 5)

Pos. [°2Th.]	Height [cts]	d-spacing [Å]	Rel. Int. [%]
8.8830	50.20	9.95517	2.69
10.4287	84.55	8.48282	4.53
12.4796	97.82	7.09301	5.24

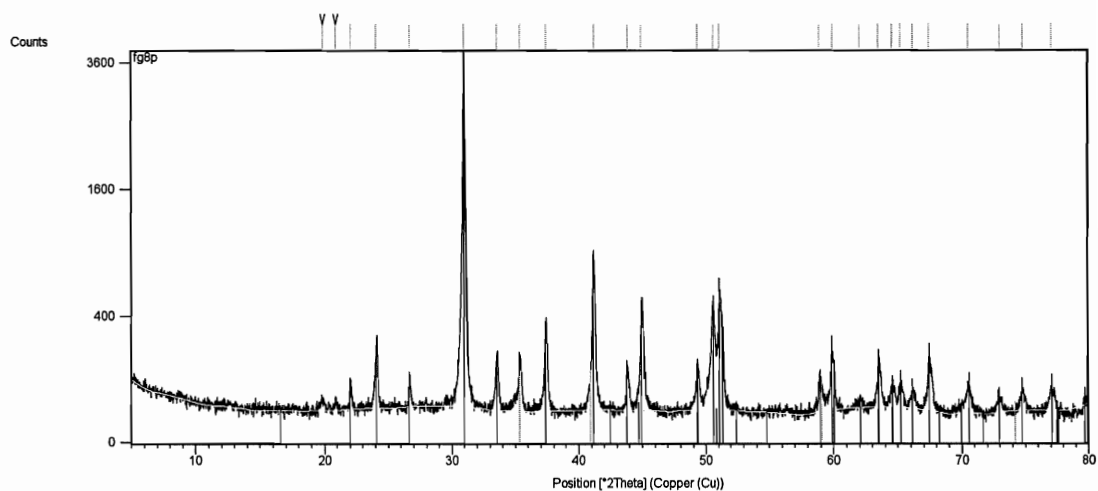
13.6040	32.03	6.50918	1.72
17.8627	27.44	4.96576	1.47
18.5919	20.18	4.77259	1.08
19.8076	34.56	4.48234	1.85
20.9132	412.60	4.24782	22.11
22.0597	33.89	4.02955	1.82
23.5817	23.04	3.77282	1.23
24.0661	105.54	3.69797	5.66
25.1961	57.50	3.53463	3.08
26.6668	1865.90	3.34293	100.00
27.3655	60.44	3.25915	3.24
27.9644	83.22	3.19070	4.46
28.3279	257.84	3.15057	13.82
29.7802	208.12	3.00015	11.15
30.0518	149.63	2.97366	8.02
30.9326	1178.83	2.89096	63.18
32.7823	29.31	2.73195	1.57
33.4765	47.09	2.67686	2.52
34.2155	25.48	2.62072	1.37
34.8138	82.80	2.57704	4.44
35.4076	202.82	2.53518	10.87
36.5671	157.25	2.45741	8.43
37.3580	125.21	2.40718	6.71
38.0781	24.35	2.36330	1.31
39.4880	134.75	2.28211	7.22
40.3161	91.96	2.23527	4.93
40.4345	78.04	2.23084	4.18
41.0939	272.72	2.19656	14.62
42.1818	109.67	2.14239	5.88
42.4459	81.00	2.12967	4.34
43.7911	28.18	2.06732	1.51
44.8854	186.18	2.01943	9.98
45.8268	71.98	1.98012	3.86
49.2040	63.42	1.85182	3.40
50.1521	320.93	1.81751	17.20
50.9835	184.30	1.79129	9.88
51.7204	36.54	1.76749	1.96
54.8957	59.60	1.67253	3.19
55.3223	35.35	1.66064	1.89
56.3541	32.23	1.63266	1.73
56.9356	32.68	1.61602	1.75
57.4864	28.63	1.60184	1.53
58.7837	22.79	1.57084	1.22
59.9742	201.75	1.54247	10.81
61.4836	21.17	1.50818	1.13
62.6187	20.22	1.48355	1.08
63.3927	37.56	1.46729	2.01
64.0688	46.32	1.45342	2.48
64.8851	30.97	1.43710	1.66
66.0218	26.04	1.41509	1.40
67.3348	58.23	1.39065	3.12
67.7418	89.10	1.38214	4.78
68.1540	127.24	1.37478	6.82
68.3345	116.88	1.37159	6.26

70.3656	34.61	1.33800	1.85
73.4868	50.36	1.28763	2.70
75.6816	68.50	1.25564	3.67
76.8023	13.14	1.24112	0.70
77.7133	16.97	1.22781	0.91

Measurement Parameters: (Bookmark1)

Dataset Name fg8p
File name C:\Program Files\PANalytical\X'Pert
Quantify\RESULTS\KT\fg8p.XRDML
Measurement Date / Time 2/8/2010 2:34:16 PM
Start Position [°2Th.] 5.0000
End Position [°2Th.] 80.0000
Step Size [°2Th.] 0.0200
Scan Step Time [s] 1.0000
Scan Type Pre-set time
Divergence Slit Type Fixed
Divergence Slit Size [°] 1.0329
Specimen Length [mm] 10.00
Receiving Slit Size [mm] 0.1000
Measurement Temperature [°C] 25.00
Anode Material Cu
K-Alpha1 [Å] 1.54060
K-Alpha2 [Å] 1.54443
K-Beta [Å] 1.39225

Graphics: (Bookmark2)



Peak List
04-008-0789
04-008-5764
04-005-4310

Identified Phases: (Bookmark 3)

Ref. Code	Score	Compound Name	Chemical Formula
04-008-0789	86	dolomite	Ca Mg (C O ₃) ₂
04-006-5764	32	Graphite-2H, syn	C
04-005-4310	32	manganosite, syn	Mn O

Candidate Patterns: (Bookmark4)

Ref. Code	Score	Compound Name	Chemical Formula
01-071-5046	20	Tazheranite	Ca _{0.22} Ti _{0.22} Zr _{0.56} O _{1.78}
01-073-3934	19	Tennantite	Cu _{12.54} (As _{0.98} Sb _{0.02}) ₄ S ₁₃
01-074-4547	19	Zirconia - synthetic	Zr _{0.88} O _{1.78}
01-082-0515	19	dimagnesium silicate	Mg ₂ (Si O ₄)
01-084-1480	18	pyrochlore (Yb-exchanged), syn	(Na _{0.5} Yb _{1.5}) (Ti Sb) O ₇
04-011-1103	18	Sodium Ytterbium Titanium Antimony Oxide	Na _{0.5} Yb _{1.5} Ti Sb O ₇
04-009-9721	18	silver catena-antimonate	Ag Sb O ₃
04-011-1102	18	Sodium Dysprosium Titanium Antimony Oxide	Na _{0.5} Dy _{1.5} Ti Sb O ₇
01-084-1479	18	pyrochlore (Dy-exchanged), syn	(Na _{0.5} Dy _{1.5}) (Ti Sb) O ₇
01-084-1475	18	pyrochlore (Cd, Yb-exchanged), syn	(Cd Yb) (Ti Sb) O ₇
04-011-1098	18	Cadmium Ytterbium Titanium Antimony Oxide	Cd Yb Ti Sb O ₇
04-011-1101	16	Sodium Gadolinium Titanium Antimony Oxide	Na _{0.5} Gd _{1.5} Ti Sb O ₇
01-084-1478	16	pyrochlore (Gd-exchanged), syn	(Na _{0.5} Gd _{1.5}) (Ti Sb) O ₇
00-018-0877	16	Taenite	(Fe , Ni)
04-011-1097	15	Cadmium Gadolinium Titanium Antimony Oxide	Cd Gd Ti Sb O ₇
01-084-1474	15	pyrochlore (Cd, Gd-exchanged), syn	(Cd Gd) (Ti Sb) O ₇
01-076-0101	15	dodecacopper(I) tetraarsenic sulfide	Cu ₁₂ As ₄ S ₁₂
00-046-1378	15	Mengxianminite (NR)	(Ca , Na) ₄ (Mg , Fe , Zn) ₅ Sn ₄ Al ₁₆ O ₄₁
00-011-0345	15	Kutnohorite	Ca (Mn , Mg) (C O ₃) ₂
04-010-2078	14	tennantite	Cu _{6.48} Fe _{5.52} As ₄ S ₁₃
04-008-8038	14	Kutnohorite	Ca Mn (C O ₃) ₂
04-003-2101	14	cobalt antimonide	Co Sb ₃
01-074-1071	14	Tennantite	Cu ₁₂ As _{3.40} Sb _{0.60} S ₁₃
00-043-1478	14	binnite	(Cu , Fe) ₁₂ As ₄ S ₁₃
00-017-0933	14	Indium Borate	In B O ₃
04-010-1154	14	binnite	Cu ₁₀ Zn ₂ Sb _{0.6} As _{3.4} S ₁₃
04-008-9876	14	Grimaldiite, syn	H Cr O ₂
01-074-1027	13	Tennantite	Cu ₁₂ As ₄ S ₁₃

01-075-3883	13	Skutterudite	In _{0.05} Co Sb ₃
00-014-0255	13	embolite, Species originally called embolite	Ag (Cl , Br)
01-085-1375	13	á-Cr O (O D), grimaldiite deuterated, syn	Cr O (O D)
03-065-2308	13	Crednerite, syn	Cu Mn O ₂
01-070-0622	13	á-Cr O O D	Cr O O D
01-072-0345	12	Calzirtite	Ca _{1.8125} Zr _{5.1625} Ti _{1.725} Fe _{0.275} O ₁₆
04-011-2415	12	fluorite	Zr ₄ N ₂ O ₅
01-075-0303	12	Halite, potassian, syn	Na _{6.990} K _{3.010} Cl
00-047-1846	12	Crerarite	(Pt , Pb) Bi ₃ (S , Se) ₄
00-035-0783	12	Isovite, syn	Cr ₂₃ C ₆
01-073-9838	12	Antimony diantimony(V) oxide hydroxide	Sb Sb ₂ O ₆ (O H)
00-038-0450	12	Zirkelite, heated	(Ca , Fe) (Nb , Ti , Ta , Zr) O ₄
00-041-0586	12	Ankerite	Ca (Fe + ₂ , Mg) (C O ₃) ₂
00-043-0693	12	Uranmicrolite	(Ca , U) _{2-x} Ta ₂ O ₆ (O H)
01-089-6287	12	hydroxylpyromorphite, syn, pentalead tris(phosphate(V)) hydroxide	Pb ₅ (P O ₄) ₃ (O H)
01-083-1531	11	Ankerite	Ca Mg _{0.32} Fe _{0.68} (C O ₃) ₂
04-009-5863	11	zirconolite-4 M, syn	Ca _{1.5} Nd Zr _{1.5} Ti ₄ O ₁₄
00-051-1507	11	Ingersonite	Ca ₃ Mn Sb ₄ O ₁₄
01-075-1533	11	Zincite, syn	Zn O
01-084-2067	11	Ankerite	Ca Mg _{0.27} Fe _{0.73} (C O ₃) ₂
00-039-0382	11	Ertixiite	Na ₂ Si ₄ O ₉
01-079-1347	11	Ankerite	Ca _{9.97} (Mg _{2.73} Fe _{6.76} Mn _{0.54}) (C O ₃) ₂

Peak List: (Bookmark 5)

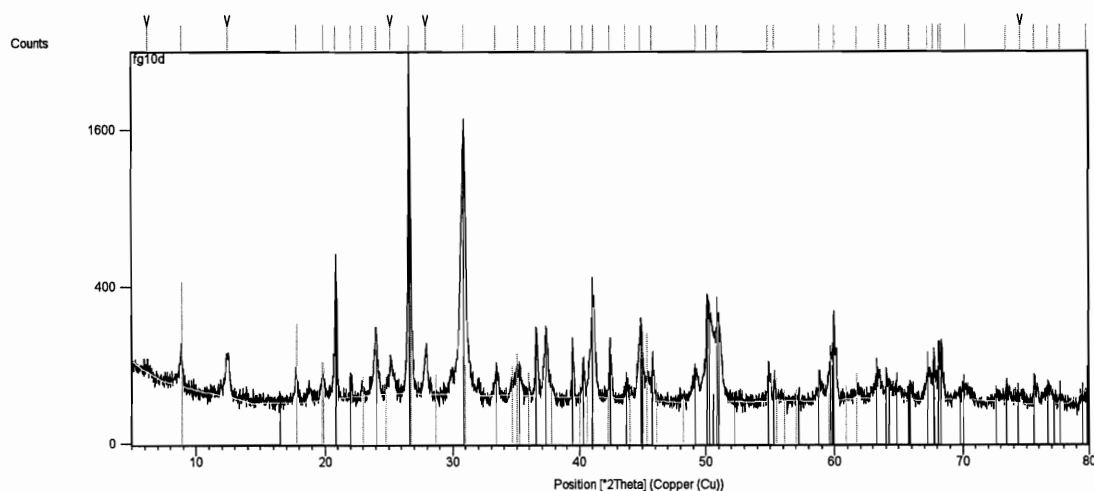
Pos. [°2Th.]	Height [cts]	d-spacing [Å]	Rel. Int. [%]
19.8759	15.12	4.46709	0.40
20.9226	19.58	4.24592	0.52
22.0738	55.32	4.02701	1.48
24.0791	224.36	3.69600	5.99
26.6830	77.84	3.34094	2.08
30.9897	3746.65	2.88576	100.00
33.5849	166.24	2.66847	4.44
35.3758	160.41	2.53738	4.28
37.4095	339.30	2.40398	9.06
41.1762	887.34	2.19055	23.68
41.2887	549.32	2.19026	14.66
43.8474	117.33	2.06309	3.13
44.9622	506.51	2.01449	13.52
49.3166	127.55	1.84633	3.40
50.5891	480.18	1.80283	12.82
51.0984	532.38	1.78605	14.21
58.9233	98.84	1.56615	2.64

59.8928	184.12	1.54310	4.91
61.9969	12.39	1.49568	0.33
63.4587	149.38	1.46470	3.99
64.5503	58.05	1.44255	1.55
65.2102	54.85	1.42954	1.46
66.1673	37.56	1.41116	1.00
67.4571	156.12	1.38728	4.17
70.5176	58.55	1.33438	1.56
72.9748	25.94	1.29539	0.69
74.7899	45.67	1.26839	1.22
77.0403	50.30	1.23685	1.34

Measurement Parameters: (Bookmark1)

Dataset Name fg10d
File name C:\Program Files\PANalytical\X'Pert
Quantify\RESULTS\KT\fg10d.XRDML
Measurement Date / Time 2/9/2010 2:21:34 PM
Start Position [$^{\circ}2\theta$.] 5.0000
End Position [$^{\circ}2\theta$.] 80.0000
Step Size [$^{\circ}2\theta$.] 0.0200
Scan Step Time [s] 1.0000
Scan Type Pre-set time
Divergence Slit Type Fixed
Divergence Slit Size [$^{\circ}$] 1.0329
Specimen Length [mm] 10.00
Receiving Slit Size [mm] 0.1000
Measurement Temperature [$^{\circ}C$] 25.00
Anode Material Cu
K-Alpha1 [\AA] 1.54060
K-Alpha2 [\AA] 1.54443
K-Beta [\AA] 1.39225

Graphics: (Bookmark2)



Peak List
01-070-7344
01-074-7804
00-007-0002

Identified Phases: (Bookmark 3)

Ref. Code	Score	Compound Name	Chemical Formula
01-070-7344	73	Quartz	Si O ₂
01-074-7804	58	Dolomite	Ca (Ca _{0.14} Mg _{0.86}) (C O ₃) ₂
00-007-0042	18	Muscovite-3T	(K , Na) (Al , Mg , Fe) ₂ (Si _{3.1} Al _{0.9}) O ₁₀ (O H) ₂

Candidate Patterns: (Bookmark4)

Ref. Code	Score	Compound Name	Chemical Formula
00-022-0712	35	Nimite-1MIIB	(Ni , Mg , Al) ₆ (Si , Al) ₄ O ₁₀ (O H) ₈
01-087-1497	34	birnessite (K), syn	K _{0.5} Mn ₂ O _{4.3} (H ₂ O) _{0.5}
01-074-7891	34	Birnessite	K _{0.312} Mn _{0.976} O ₂ (H ₂ O) _{0.37}
01-072-6745	30	Birnessite, syn	Na _{0.364} Mn O ₂ (H ₂ O) _{0.544}
01-073-9669	29	Sodium manganese(IV) manganese(III) oxide hydrate	Na _{0.58} Mn _{1.42} Mn _{0.58} O ₄ (H ₂ O) _{2.3}
01-072-7297	29	Birnessite, syn	Na _{0.58} Mn ₂ O ₄ (H ₂ O) _{1.5}
00-047-1821	29	Jianshuiite	(Mg , Mn +2) Mn ₃₊₄ O ₇₊₃ H ₂ O
01-080-2147	25	á-Si O ₂ , quartz, syn	Si O ₂
04-007-2812	24	lead diantimonate	Pb Sb ₂ O ₆
01-076-0927	24	sodium calcium tecto-alumosilicate	(Na _{0.84} Ca _{0.16}) Al _{1.16} Si _{2.84} O ₈
00-043-1456	23	Birnessite, syn	Na _{0.55} Mn ₂ O ₄ · 1.5 H ₂ O
01-073-7865	23	Potassium manganese(IV) manganese(III) oxide hydrate	K _{0.27} (Mn _{0.96} O ₂) (H ₂ O) _{0.69}
01-072-1335	22	lead catena-diantimonate	Pb Sb ₂ O ₆
00-038-0327	21	Linde B1	0.95 Na ₂ O · Al ₂ O ₃ · 3.35 Si O ₂ · 4.79 H ₂ O
01-074-9332	21	Langasite	La ₃ (Ga ₄ (Ga _{1.07} Si _{0.93}) O ₁₄)
01-074-9333	20	Langasite	La ₃ (Ga ₄ (Ga _{1.25} Si _{0.75}) O ₁₄)
03-065-3562	20	Klockmannite	Cu Se
00-041-1480	19	Albite, calcian, ordered	(Na , Ca) Al (Si , Al) ₃ O ₈
01-074-9339	19	Langasite	La ₃ (Ga ₄ (Ga _{0.978} Ge _{0.048} Si _{0.942}) O ₁₄)
04-001-4943	19	copper(I) indium sulfide	Cu In S ₂
01-074-9331	19	Langasite	La ₃ (Ga ₄ (Ga _{1.22} Si _{0.78}) O ₁₄)
00-030-0691	19	Geocronite	Pb ₁₄ (Sb , As) ₆ S ₂₃
01-074-9337	19	Langasite	La ₃ (Ga ₄ (Ga _{1.05} Si _{0.95}) O ₁₄)
01-074-9336	19	Langasite	La ₃ (Ga ₄ (Ga _{1.01} Ge _{0.02})

01-071-0441	18	beryllonite zincian, syn	Si _{0.97} O ₁₄) Na (Zn _{0.8} Fe _{0.2}) P O ₄
01-070-7027	18	trilanthanum pentagallosilicate	La ₃ (Ga ₅ Si O ₁₄)
01-074-9338	18	Langasite	La ₃ (Ga ₄ (Ga _{0.77} Ge _{0.252} Si _{0.876}) O ₁₄)
04-006-7955	18	Baddeleyite, cerian, syn	Ce _{0.02} Zr _{0.98} O ₂
01-074-9568	18	Stistaite	Sb Sn
01-084-0752	18	Albite, (low)	Na Al _{0.91} Si ₃ O ₈
00-033-1049	17	Compreignacite, syn	K ₂ (U O ₂) ₆ O ₄ (O H) ₆ · 8 H ₂ O
01-085-0721	17	Tetradymite	Bi ₂ Te ₂ S
04-010-6455	16	Baddeleyite, vanadian, syn	Zr _{0.95} V _{0.05} O ₂
01-072-6096	16	iron iron(III) silicon oxide hydroxide	Fe ₃ (Si _{1.32} Fe _{0.68}) O ₅ (O H) ₄
04-006-7958	16	Baddeleyite, cerian, syn	Ce _{0.1} Zr _{0.9} O ₂
00-037-1484	16	zirconia, zirconium dioxide, zirkite	Zr O ₂
00-045-1321	16	Clinochlore-1MIIb, mangoan	Mg ₃ Mn ₂ Al Si ₃ Al O ₁₀ (O H) ₈
01-070-2157	16	Polyhalite	K ₂ Ca ₂ Mg (S O ₄) ₄ (H ₂ O) ₂
01-089-2734	16	Klockmannite, syn	Cu _{0.87} Se
00-016-0145	16	Calcurmolite	Ca (U O ₂) ₃ (Mo O ₄) ₃ (O H) ₂ · 8 H ₂ O
04-006-9856	16	Baddeleyite, cerian, syn	Ce _{0.09} Zr _{0.91} O ₂
01-070-3752	16	Albite	(Na _{0.98} Ca _{0.02}) (Al _{1.02} Si _{2.98} O ₈)
01-072-6682	16	Baddeleyite, vanadian, syn	(V _{0.09} Zr _{0.91}) O ₂
01-072-6683	16	Baddeleyite, vanadian, syn	(V _{0.06} Zr _{0.94}) O ₂
01-072-6680	16	Baddeleyite, vanadian, syn	(V _{0.03} Zr _{0.97}) O ₂
03-065-3992	15	Geocronite	As _{5.50} Pb ₂₈ S ₄₆ Sb _{6.50}
01-085-1435	15	Manganpyrosomalite, ferroan	Fe ₇ Mn ₉ Si ₁₂ O ₃₀ (O H) ₁₇ Cl ₃
01-074-9335	15	Langasite	La ₃ (Ga ₄ (Ga _{1.07} Ge _{0.07} Si _{0.86}) O ₁₄)
00-043-1474	15	Geocronite	Pb ₁₄ Sb ₆ S ₂₃
00-044-0308	15	Silver Aluminum Nitrite Silicate	Ag ₈ (Al Si O ₄) ₆ (N O ₂) ₂

Peak List: (Bookmark 5)

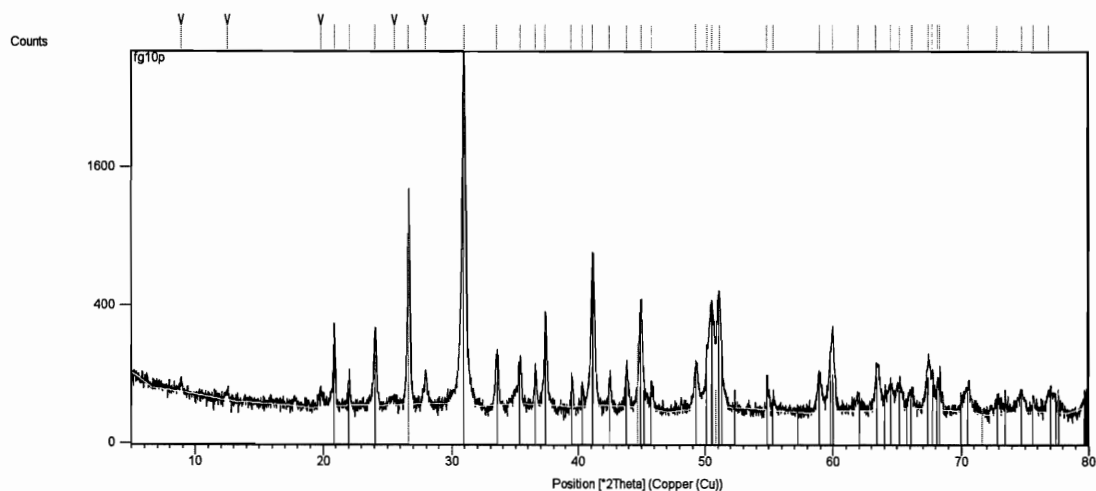
Pos. [°2Th.]	Height [cts]	d-spacing [Å]	Rel. Int. [%]
6.2565	14.51	14.12713	0.58
8.8671	113.00	9.97292	4.52
12.5313	88.20	7.06382	3.53
17.7863	50.62	4.98692	2.02
19.9019	39.94	4.46132	1.60
20.8818	507.96	4.25412	20.31
22.0784	41.20	4.02619	1.65
22.9653	12.31	3.87267	0.49
24.0356	177.35	3.70259	7.09
25.1982	78.04	3.53433	3.12
26.6492	2501.27	3.34510	100.00

27.9651	124.59	3.19061	4.98
30.8925	1687.30	2.89462	67.46
33.4125	50.88	2.68185	2.03
35.1684	45.40	2.55187	1.82
36.5288	157.20	2.45989	6.28
37.2986	188.03	2.41088	7.52
39.4648	129.35	2.28340	5.17
40.2750	79.61	2.23931	3.18
41.1399	323.10	2.19421	12.92
42.4480	152.34	2.12957	6.09
43.7434	22.44	2.06947	0.90
44.8798	227.93	2.01967	9.11
45.8041	86.42	1.98104	3.45
49.2697	53.53	1.84951	2.14
50.1288	317.24	1.81981	12.68
50.9679	232.69	1.79180	9.30
54.8772	79.33	1.67305	3.17
55.3323	34.98	1.66036	1.40
58.8956	30.13	1.56812	1.20
59.9565	254.87	1.54161	10.19
60.1240	117.20	1.54154	4.69
61.7978	15.41	1.50002	0.62
63.5152	44.40	1.46354	1.78
64.0507	43.35	1.45259	1.73
65.8989	20.30	1.41625	0.81
67.3102	48.82	1.38995	1.95
67.7548	109.60	1.38191	4.38
68.1420	138.82	1.37499	5.55
68.3188	144.47	1.37187	5.78
70.2593	17.60	1.33865	0.70
73.4420	26.59	1.28830	1.06
74.6195	11.89	1.27086	0.48
75.6775	44.84	1.25570	1.79
76.7965	21.37	1.24017	0.85
77.7052	13.41	1.22792	0.54
79.8639	29.95	1.20007	1.20

Measurement Parameters: (Bookmark1)

Dataset Name fg10p
File name C:\Program Files\PANalytical\X'Pert
Quantify\RESULTS\KT\fg10p.XRDML
Measurement Date / Time 2/8/2010 10:38:52 AM
Start Position [°2Th.] 5.0000
End Position [°2Th.] 80.0000
Step Size [°2Th.] 0.0200
Scan Step Time [s] 1.0000
Scan Type Pre-set time
Divergence Slit Type Fixed
Divergence Slit Size [°] 1.0329
Specimen Length [mm] 10.00
Receiving Slit Size [mm] 0.1000
Measurement Temperature [°C] 25.00
Anode Material Cu
K-Alpha1 [Å] 1.54060
K-Alpha2 [Å] 1.54443
K-Beta [Å] 1.39225

Graphics: (Bookmark2)



Peak List
00-036-0426
01-070-3755
01-071-3733

Identified Phases: (Bookmark 3)

Ref. Code	Score	Compound Name	Chemical Formula
00-036-0426	74	Dolomite	Ca Mg (C O ₃) ₂
01-070-3755	69	Quartz	Si O ₂
01-071-3739	34	Graphite-2H	C

Candidate Patterns: (Bookmark4)

Ref. Code	Score	Compound Name	Chemical Formula
04-008-9876	25	Grimaldiite, syn	H Cr O ₂
04-006-7957	20	Baddeleyite, cerian, syn	Ce _{0.08} Zr _{0.92} O ₂
00-041-1480	20	Albite, calcian, ordered	(Na , Ca) Al (Si , Al) ₃ O ₈
04-006-7956	19	Baddeleyite, cerian, syn	Ce _{0.05} Zr _{0.95} O ₂
04-006-7955	19	Baddeleyite, cerian, syn	Ce _{0.02} Zr _{0.98} O ₂
01-074-9335	18	Langasite	La ₃ (Ga ₄ (Ga _{1.07} Ge _{0.07} Si _{0.86}) O ₁₄)
01-074-9337	18	Langasite	La ₃ (Ga ₄ (Ga _{1.05} Si _{0.95}) O ₁₄)
01-076-0927	18	sodium calcium tecto-alumosilicate	(Na _{0.84} Ca _{0.16}) Al _{1.16} Si _{2.84} O ₈
01-070-0622	17	á-Cr O O D	Cr O O D
01-074-9094	17	Langanite	La ₃ ((Ga _{5.48} Nb _{0.52}) O ₁₄)
01-074-9332	17	Langasite	La ₃ (Ga ₄ (Ga _{1.07} Si _{0.93}) O ₁₄)
01-074-9336	17	Langasite	La ₃ (Ga ₄ (Ga _{1.01} Ge _{0.02} Si _{0.97}) O ₁₄)
04-004-4339	17	zirconium dioxide	Zr O ₂
01-084-0752	17	Albite, (low)	Na Al _{0.91} Si ₃ O ₈
01-074-9331	17	Langasite	La ₃ (Ga ₄ (Ga _{1.22} Si _{0.78}) O ₁₄)
01-085-1375	17	á-Cr O (O D), grimaldiite deuterated, syn	Cr O (O D)
01-089-5472	16	Baddeleyite, scandian, syn	Zr _{0.96} Sc _{0.04} O _{1.98}
01-084-1474	16	pyrochlore (Cd, Gd-exchanged), syn	(Cd Gd) (Ti Sb) O ₇
04-011-1097	16	Cadmium Gadolinium Titanium Antimony Oxide	Cd Gd Ti Sb O ₇
01-074-9333	16	Langasite	La ₃ (Ga ₄ (Ga _{1.25} Si _{0.75}) O ₁₄)
04-011-1101	16	Sodium Gadolinium Titanium Antimony Oxide	Na _{0.5} Gd _{1.5} Ti Sb O ₇
01-084-1478	16	pyrochlore (Gd-exchanged), syn	(Na _{0.5} Gd _{1.5}) (Ti Sb) O ₇
01-072-6680	16	Baddeleyite, vanadian, syn	(V _{0.03} Zr _{0.97}) O ₂
04-006-7958	16	Baddeleyite, cerian, syn	Ce _{0.1} Zr _{0.9} O ₂
01-089-5471	16	Baddeleyite, scandian, syn	Zr _{0.98} Sc _{0.02} O _{1.99}
01-070-3752	16	Albite	(Na _{0.98} Ca _{0.02}) (Al _{1.02}

01-074-9339	16	Langasite	Si _{2.98} O ₈) La ₃ (Ga ₄ (Ga _{0.978} Ge _{0.048} Si _{0.942}) O ₁₄)
01-089-6287	15	hydroxylpyromorphite, syn, pentalead tris(phosphate(V)) hydroxide	Pb ₅ (P O ₄) ₃ (O H)
04-010-6455	15	Baddeleyite, vanadian, syn	Zr _{0.95} V _{0.05} O ₂
01-070-7027	15	trilanthanum pentagallosilicate	La ₃ (Ga ₅ Si O ₁₄)
01-074-9093	15	Langanite	La ₃ ((Ga _{5.47} Nb _{0.53}) O ₁₄)
00-037-1484	15	zirconia, zirconium dioxide, zirkite	Zr O ₂
00-043-1478	14	binnite	(Cu , Fe) ₁₂ As ₄ S ₁₃
01-074-9338	14	Langasite	La ₃ (Ga ₄ (Ga _{0.77} Ge _{0.252} Si _{0.876}) O ₁₄)
04-010-1154	14	binnite	Cu ₁₀ Zn ₂ Sb _{0.6} As _{3.4} S ₁₃
00-006-0427	14	Klockmannite	Cu Se
04-006-7960	14	Baddeleyite, cerian, syn	Ce _{0.12} Zr _{0.88} O ₂
04-009-7705	14	spinel, submagnesian, manganian, syn	Mg _{0.449} Mn _{0.012} Al _{2.359} O ₄
01-071-5078	14	spinel, syn	(Mg _{0.41} Mn _{0.01} Al _{0.58}) (Al _{1.78} Mg _{0.04}) O ₄
01-074-1071	14	Tennantite	Cu ₁₂ As _{3.40} Sb _{0.60} S ₁₃
00-033-1348	14	Strontiumapatite, syn	Sr ₅ (P O ₄) ₃ (O H)
01-072-6683	13	Baddeleyite, vanadian, syn	(V _{0.06} Zr _{0.94}) O ₂
04-010-2078	13	tennantite	Cu _{6.48} Fe _{5.52} As ₄ S ₁₃
04-003-2101	13	cobalt antimonide	Co Sb ₃
01-076-0101	13	dodecacopper(I) tetraarsenic sulfide	Cu ₁₂ As ₄ S ₁₂
01-072-6684	13	Baddeleyite, vanadian, syn	(V _{0.12} Zr _{0.88}) O ₂
01-072-6682	13	Baddeleyite, vanadian, syn	(V _{0.09} Zr _{0.91}) O ₂
00-047-1769	13	Kieftite	Co Sb ₃
01-081-1314	12	Baddeleyite, syn	Zr _{0.944} O ₂
00-045-1436	12	Giniite, ferrian, syn	Fe ₅ (P O ₄) ₄ (O H) ₃ · 2 H ₂ O

Peak List: (Bookmark 5)

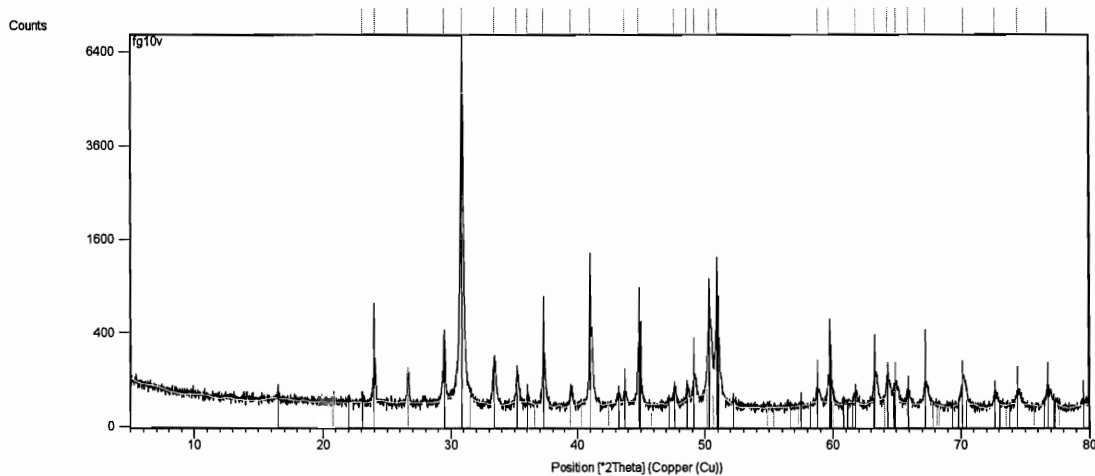
Pos. [°2Th.]	Height [cts]	d-spacing [Å]	Rel. Int. [%]
8.9019	22.11	9.93405	0.69
12.5290	20.59	7.06513	0.64
19.8356	25.40	4.47607	0.79
20.9004	270.25	4.25037	8.44
22.0900	83.89	4.02409	2.62
24.0806	249.84	3.69577	7.81
25.5900	9.41	3.48110	0.29
26.6660	1273.65	3.34303	39.79
27.9897	67.04	3.18787	2.09
30.9696	3200.71	2.88759	100.00
33.5261	122.60	2.67302	3.83
35.3905	99.86	2.53636	3.12
36.5954	75.19	2.45557	2.35
37.3439	306.63	2.40806	9.58

39.4785	64.23	2.28263	2.01
40.3293	37.93	2.23642	1.19
41.1428	736.14	2.19406	23.00
42.4849	57.53	2.12781	1.80
43.8313	93.31	2.06552	2.92
44.9825	406.81	2.01530	12.71
45.8157	47.12	1.98057	1.47
49.2469	101.20	1.85031	3.16
50.1462	177.13	1.81771	5.53
50.5518	361.92	1.80557	11.31
51.1239	452.52	1.78670	14.14
54.8805	71.92	1.67157	2.25
55.3270	24.65	1.66051	0.77
58.9406	75.46	1.56703	2.36
59.9754	261.97	1.54117	8.18
61.9435	17.19	1.49808	0.54
63.3721	106.26	1.46771	3.32
64.5010	42.46	1.44473	1.33
65.2047	46.72	1.43083	1.46
66.1557	29.06	1.41255	0.91
67.4707	112.94	1.38703	3.53
67.7689	85.47	1.38509	2.67
68.1600	68.18	1.37468	2.13
68.3398	101.27	1.37150	3.16
70.5411	47.59	1.33399	1.49
72.8807	23.09	1.29683	0.72
74.7549	31.27	1.26889	0.98
75.6778	24.14	1.25570	0.75
76.9050	33.41	1.23869	1.04

Measurement Parameters: (Bookmark1)

Dataset Name fg10v
File name C:\Program Files\PANalytical\X'Pert
Quantify\RESULTS\KT\fg10v.XRDML
Measurement Date / Time 2/10/2010 1:28:15 PM
Start Position [$^{\circ}2\text{Th.}$] 5.0000
End Position [$^{\circ}2\text{Th.}$] 80.0000
Step Size [$^{\circ}2\text{Th.}$] 0.0200
Scan Step Time [s] 1.0000
Scan Type Pre-set time
Divergence Slit Type Fixed
Divergence Slit Size [$^{\circ}$] 1.0329
Specimen Length [mm] 10.00
Receiving Slit Size [mm] 0.1000
Measurement Temperature [$^{\circ}\text{C}$] 25.00
Anode Material Cu
K-Alpha1 [\AA] 1.54060
K-Alpha2 [\AA] 1.54443
K-Beta [\AA] 1.39225

Graphics: (Bookmark2)



Peak List
01-074-7798
01-085-1108
01-085-0790

Identified Phases: (Bookmark 3)

Ref. Code	Score	Compound Name	Chemical Formula
01-074-7798	54	Ankerite	Ca (Mg _{0.67} Fe _{0.33}) (C O ₃) ₂
01-085-1108	40	Calcite, syn	Ca C O ₃
01-085-0796	20	Quartz, syn	Si O ₂

Candidate Patterns: (Bookmark4)

Ref. Code	Score	Compound Name	Chemical Formula
04-008-0796	23	ankerite	Ca Mg _{0.27} Fe _{0.73} (C O ₃) ₂
01-079-1349	23	ankerite HP	Ca. ₉₉₇ (Mg. ₂₇₃ Fe. ₆₇₆ Mn. ₀₅₄) (C O ₃) ₂
04-002-7701	17	Cerium Europium Selenium	Ce ₂ Eu Se ₄
00-048-1333	16	Americium Iridium	Am Ir ₂
04-004-5866	16	Lanthanum Selenium	La _{2.67} Se ₄
04-002-2281	16	Copper Lanthanum Selenium	Cu _{0.5} La _{2.5} Se ₄
04-006-5650	16	Copper Lanthanum Selenium	Cu _{0.5} La _{2.5} Se ₄
04-010-5328	14	Erbium Palladium Gallium	Er Pd Ga
01-071-5095	14	distrontium germanate	Sr ₂ (Ge O ₄)
01-072-8975	13	Gadolinium Ruthenium	Gd Ru ₂
04-003-6581	13	Gadolinium Ruthenium	Gd Ru ₂
04-003-7048	13	Cerium Ruthenium	Ce Ru ₂
04-004-3876	13	Curium Iridium	Cm Ir ₂
04-006-7067	13	Curium Iridium	Cm Ir ₂
04-002-2287	13	Silver Lanthanum Selenium	Ag _{0.5} La _{2.5} Se ₄
04-007-8340	13	Curium Iridium	Cm Ir ₂
04-010-1578	13	Neodymium Rhodium Silicide	Nd Rh ₃ Si ₂
04-003-1080	13	Neodymium Rhodium	Nd Rh ₂
04-007-8338	13	Americium Iridium	Am Ir ₂
04-001-3400	13	Cerium Ruthenium	Ce Ru ₂
04-002-3015	13	Erbium Selenium	Er _{2.67} Se ₄
04-002-5340	13	Lanthanum Selenium	La _{2.67} Se ₄
04-004-0926	13	Lanthanum Selenium	La _{2.67} Se ₄
04-004-1121	13	Lanthanum Selenium	La _{2.67} Se ₄
04-001-3399	12	Samarium Ruthenium	Sm Ru ₂
04-007-7252	12	Silver Cerium Antimony	Ag Ce Sb ₂
04-011-0299	12	Strontium Germanium Oxide	Sr ₂ (Ge O ₄)
01-075-3693	12	Dolomite	Ca Mg (C O ₃) ₂
01-075-3695	12	Dolomite	Ca Mg (C O ₃) ₂
01-071-8298	12	Iron Manganese Yttrium	(Fe _{0.25} Mn _{0.75}) ₂ Y
03-065-5100	12	Iron Manganese Yttrium	Fe Mn ₃ Y ₂
01-081-0429	12	Yttrium Nickel Hydride	Y _{0.937} Ni ₂ H _{2.835}
01-072-6471	12	zirconium iron deuteride	Zr Fe ₂ D _{2.66}
04-001-0031	12	Hafnium Molybdenum	Hf Mo ₂
01-087-1605	12	á`L-Sr ₂ (Ge O ₄), distrontium germanate	Sr ₂ (Ge O ₄)

03-065-4879	12	Cobalt Manganese Yttrium	Co Mn ₃ Y ₂
01-071-7322	12	Cobalt Manganese Yttrium	(Co _{0.5} Mn _{1.5}) Y
01-074-3928	11	Samarium ruthenium germanide	Sm Ru _{1.54} Ge _{0.46}
01-075-3694	11	Dolomite	Ca Mg (C O ₃) ₂
04-003-5964	11	Scandium Aluminum	Sc Al ₂
04-003-1317	11	Cerium Ruthenium	Ce Ru ₂
01-075-3692	11	Dolomite	Ca Mg (C O ₃) ₂
00-052-0546	11	Europium Manganese Tantalum Oxide	Eu ₂ Mn Ta _{1.175} O _{7.448}
01-071-5666	11	Aluminum Chromium Cobalt	(Al _{0.7} Cr _{0.3}) Co
00-005-0622	11	Dolomite	Ca Mg (C O ₃) ₂
04-001-1871	11	Gold Europium	Au ₂ Eu ₃
04-009-3411	11	Strontium Tin Oxide	Sr ₃ Sn ₂ O ₇
00-035-1377	11	Cesium Nickel Tin	Cs Ni ₂ Sn ₂
04-001-1817	11	Hafnium Molybdenum	Hf Mo ₂
04-002-9767	11	Hafnium Molybdenum	Hf Mo ₂

Peak List: (Bookmark 5)

Pos. [°2Th.]	Height [cts]	d-spacing [Å]	Rel. Int. [%]
23.0965	17.29	3.85096	0.25
24.0314	195.67	3.70323	2.80
26.6568	119.18	3.34417	1.70
29.4703	367.45	3.03099	5.25
30.8816	6995.67	2.89562	100.00
33.4393	211.03	2.67976	3.02
35.2157	105.30	2.54855	1.51
36.0511	23.50	2.49139	0.34
37.3107	255.24	2.41012	3.65
39.5249	49.47	2.28006	0.71
41.0339	551.88	2.19963	7.89
43.7374	34.18	2.06974	0.49
44.8447	306.99	2.02117	4.39
47.6654	41.50	1.90794	0.59
48.5935	44.54	1.87365	0.64
49.1931	79.95	1.85221	1.14
50.3404	568.78	1.81265	8.13
50.9355	609.37	1.79287	8.71
58.8401	26.13	1.56947	0.37
59.6886	97.36	1.54917	1.39
61.7998	29.49	1.50122	0.42
63.2830	119.83	1.46956	1.71
64.3148	95.44	1.44846	1.36
64.9805	57.80	1.43522	0.83
65.9208	25.65	1.41701	0.37
67.2628	78.09	1.39196	1.12
70.1985	96.04	1.34077	1.37
72.6674	42.41	1.30119	0.61
74.4105	34.59	1.27497	0.49
76.7349	53.83	1.24101	0.77